



# BRNO UNIVERSITY OF TECHNOLOGY

VYSOKÉ UČENÍ TECHNICKÉ V BRNĚ

## FACULTY OF ELECTRICAL ENGINEERING AND COMMUNICATION

FAKULTA ELEKTROTECHNIKY  
A KOMUNIKAČNÍCH TECHNOLOGIÍ

## DEPARTMENT OF RADIO ELECTRONICS

ÚSTAV RADIOELEKTRONIKY

# OPTIMAL INTENSITY DISTRIBUTION IN A LASER BEAM FOR FSO COMMUNICATIONS

OPTIMÁLNÍ ROZLOŽENÍ OPTICKÉ INTENZITY V LASEROVÉM SVAZKU PRO FSO KOMUNIKACE

## DOCTORAL THESIS

DIZERTAČNÍ PRÁCE

**AUTHOR**  
AUTOR PRÁCE

Ing. Peter Barcík

**SUPERVISOR**  
ŠKOLITEL

prof. Ing. Otakar Wilfert, CSc.

BRNO 2016

## **ABSTRACT**

The doctoral thesis is focused on analysing the distribution of optical intensity within a radiated laser beam at the plane of the transmitting (TXA) and receiving (RXA) aperture which is affected by propagation through free space as well as through the atmosphere. The aim of the thesis is to determine the optimal intensity distribution of the laser beam at the transmitter plane which is less affected by turbulence during propagation and transmitter aperture itself. In order to analyse the propagation of an optical wave through atmospheric turbulence, the simulation based on the Split-Step method is utilized. The propagation of the Flattened Gaussian beam was analysed for weak and moderate turbulence regimes. The thesis discusses usage of multimode fiber with large diameter as a shaping element and includes a design of the refraction beam shaper which is able to convert the Gaussian beam to a flattened Gaussian beam. Finally, a model of a fully photonic transmitter and receiver was built. The system is used for generating and receiving an optical coherent wave.

## **KEYWORDS**

Top-hat beam, Gaussian beam, scintillation index, atmospheric turbulence, refraction beam shaper, aspheric optical elements.

## **ABSTRAKT**

Dizertačná práca je zameraná na štúdium a analýzu rozloženia optickej intenzity v laserovom zväzku v rovine vysielacej (TXA) a prijímacej apertúry (RXA), ktorý podlieha zmenám ako pri šírení voľným priestorom, tak pri šírení atmosférou. Cieľom práce je nájsť optimálne rozloženie optickej intezity v rovine vysielacej apertúry, ktoré bude minimálne ovplyvnené apertúrou vysielача a atmosférickými turbulenciami. Za účelom analýzy šírenia optickej vlny atmosférou bola využitá simulácia založená na metóde Split-Step. Šírenie Flattened Gaussian zväzku bolo analyzované pre režim slabých a stredných turbulencií. Práca sa zaoberá použitím multimódového vlákna s veľkým priemerom jadra ako tvarujúceho elementu a obsahuje návrh refrakčného tvarovača, pomocou ktorého je možno konvertovať Gaussovský zväzok na zväzok s uniformným rozložením optickej intenzity. Nakoniec je pomocou získaných poznatkov zostavený plne fotonický vysieláč a prijímač, ktorých použitie spočíva v generovaní a prijímaní optickej koherentnej vlny prenášajúcej presnú fázu.

## **KLÍČOVÁ SLOVA**

Top-hat zväzok, Gaussovský zväzok, index scintilácie, atmosférické turbulencie, refrakčný tvarovač zväzku, asférické optické prvky.

BARCÍK, Peter *Optimal intensity distribution in a laser beam for FSO communications*: doctoral thesis. Brno: Brno University of Technology, Faculty of Electrical Engineering and Communication, Department of Radio Electronics, 2016. 96 p. Supervised by Prof. Ing. Otakar Wilfert, CSc.

## DECLARATION

I declare that I have written my doctoral thesis on the theme of “Optimal intensity distribution in a laser beam for FSO communications” independently, under the guidance of the doctoral thesis supervisor and using the technical literature and other sources of information which are all quoted in the thesis and detailed in the list of literature at the end of the thesis.

As the author of the doctoral thesis I furthermore declare that, as regards the creation of this doctoral thesis, I have not infringed any copyright. In particular, I have not unlawfully encroached on anyone’s personal and/or ownership rights and I am fully aware of the consequences in the case of breaking Regulation § 11 and the following of the Copyright Act No 121/2000 Sb., and of the rights related to intellectual property right and changes in some Acts (Intellectual Property Act) and formulated in later regulations, inclusive of the possible consequences resulting from the provisions of Criminal Act No 40/2009 Sb., Section 2, Head VI, Part 4.

Brno .....

.....

(author’s signature)

## ACKNOWLEDGEMENT

Firstly, I would like to express my sincere gratitude to my advisor Prof. Ing. Otakar Wilfert, CSc. for the continuous support of my Ph.D study and related research, for his patience, motivation, and immense knowledge. His guidance helped me in all the time of research and writing of this thesis.

I also would like to thank to my family for their continuous support during my studies and for always believing in me.

Brno .....

.....

(author's signature)



Faculty of Electrical Engineering  
and Communication  
Brno University of Technology  
Technická 12, CZ-61600 Brno  
Czech Republic  
<http://www.six.feec.vutbr.cz>

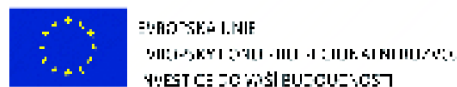
## ACKNOWLEDGEMENT

The research described in this doctoral thesis has been done in laboratories supported by Sensor, Information and Communication Systems Research Centre (SIX) project; registration number CZ.1.05/2.1.00/03.0072, Operational Program Research and Development for Innovation.

Brno .....

.....

(author's signature)



# Contents

<b>Introduction</b>	<b>12</b>
<b>1 State of the art</b>	<b>14</b>
1.1 Atmospheric turbulences . . . . .	14
1.2 Propagation of optical wave through turbulent medium . . . . .	16
1.2.1 Coherence . . . . .	16
1.2.2 Beam spreading . . . . .	18
1.2.3 Beam wandering . . . . .	19
1.2.4 Angle of arrival . . . . .	19
1.2.5 Optical scintillation . . . . .	20
1.3 Beam shapes . . . . .	22
<b>2 Objectives of the thesis</b>	<b>28</b>
<b>3 Numerical simulation of optical wave propagation</b>	<b>29</b>
3.1 Phase screen modeling . . . . .	29
3.2 Gaussian beam propagation simulation . . . . .	30
<b>4 Flattened-Gaussian beam</b>	<b>32</b>
4.1 Flattened Gaussian beam scintillation . . . . .	35
4.2 Simulation of Flattened Gaussian beam propagation . . . . .	36
4.3 Aperture averaging . . . . .	39
4.4 Probability of fade . . . . .	40
4.5 Summary . . . . .	42
<b>5 Beam shaper for free space optical communication transmitter</b>	<b>43</b>
5.1 Refraction beam shaper . . . . .	44
5.2 Optical fiber as a beam shaper . . . . .	49
5.3 Summary . . . . .	52
<b>6 Fully photonic link</b>	<b>53</b>
6.1 Transmitter with large core optical fiber . . . . .	53
6.2 Fully photonic receiver . . . . .	56

6.3	Estimation of received power by the Schmidt Cassegrain telescope . .	58
6.4	Diffraction of the optical wave caused by Schmidt Cassegrain telescope	60
6.5	Testing Transmitter . . . . .	66
6.6	Coupling efficiency . . . . .	67
6.7	Experimental measurement of the coupling loss . . . . .	71
6.8	Channel Characterization . . . . .	73
6.9	Summary . . . . .	76
<b>7</b>	<b>Conclusion</b>	<b>77</b>
	<b>Bibliography</b>	<b>79</b>
	<b>List of symbols, physical constants and abbreviations</b>	<b>86</b>
	<b>List of appendices</b>	<b>90</b>
<b>A</b>	<b>Curriculum Vitae</b>	<b>91</b>
<b>B</b>	<b>List of Publications</b>	<b>94</b>

# List of Figures

1.1	Beam wander . . . . .	19
1.2	Simulated field distribution of the Hermite–Gaussian beams for different $m$ and $n$ parameters . . . . .	23
1.3	Longitudinal intensity distribution of the Hermite – Gaussian beam ( $m, n=2$ ) beam for vacuum propagation . . . . .	23
1.4	Simulated field distribution of the Laguerre Gaussian beams for different $l$ and $p$ parameters . . . . .	24
1.5	Simulated field distribution of the Cos Gaussian beams for different $\beta$ parameters . . . . .	24
1.6	Simulated field distribution of the Cosh Gaussian beams for different $\Omega_0$ parameters . . . . .	25
1.7	Simulated field distribution of the dark hollow beam for $w_1 = 0.5\text{ mm}$ and $w_2 = 0.3\text{ mm}$ . . . . .	26
1.8	Longitudinal intensity distribution of the Dark hollow beam for vacuum propagation . . . . .	26
1.9	Simulated field distribution of the first kind Bessel – Gaussian beams	27
1.10	Longitudinal intensity distribution of the Bessel – Gaussian beam ( $n=1$ ) for vacuum propagation . . . . .	27
3.1	Split-step propagation method interpretation . . . . .	29
3.2	One realization of the phase screen created by sub-harmonics method	30
3.3	Initial Gaussian beam (a) and irradiance resulting from turbulence propagation (b) for $C_n^2 = 10^{-14}\text{ m}^{-2/3}$ . . . . .	31
3.4	Theoretical and simulated scintillation index of collimated Gaussian beam as a function of propagation length . . . . .	31
4.1	Mathematical functions for representation top-hat beams . . . . .	33
4.2	FG beam for various $N$ parameters as a function of radial distance normalized with beam half-width . . . . .	33
4.3	Propagation scheme . . . . .	34
4.4	Longitudinal intensity distribution of the FG beam for vacuum propagation . . . . .	34



4.5	Initial top-hat beam (a) and irradiance resulting from turbulence propagation (b) for $C_n^2 = 10^{-14} m^{-2/3}$ . . . . .	36
4.6	Simulated on-axis scintillation index as a function of propagation length for the FG beam with radius 10 mm at TXA plane . . . . .	37
4.7	Simulated on-axis scintillation index as a function of propagation length for the FG beam with radius 40 mm at TXA plane . . . . .	37
4.8	Simulated scintillation index for the FG beam as a function of beam radius at the TXA . . . . .	38
4.9	Simulated scintillation index for the FG beam as a function of flatness parameter $N$ . . . . .	38
4.10	Power scintillation index as a function of propagation length for different radius of receiving aperture . . . . .	39
4.11	Aperture averaging factor as a function of radius of the receiving aperture . . . . .	39
4.12	Probability of fade as a function of treshold level . . . . .	41
4.13	Expected number of fades as a function of threshold level . . . . .	41
5.1	Experimentally measured intensity profile of FG beam - lenslet array shaping technique . . . . .	43
5.2	Experimentally measured intensity profile of FG beam - diffractive diffuser shaping technique . . . . .	44
5.3	Scheme of refraction beam shaper based on Keplerian design . . . . .	45
5.4	Sag of the lenses . . . . .	46
5.5	Layout of the beam shaper . . . . .	47
5.6	Zemax simulation results . . . . .	48
5.7	The scintillation index at RXA for both beams as a function of beam radius at TXA (a) and the scintillation index for both beams with radius of 40 mm at RXA as a function of propagation length (b). . . . .	49
5.8	Optical intensity distribution of the single mode fiber . . . . .	50
5.9	Optical intensity distribution of the multimode fiber . . . . .	51
5.10	Optical intensity distribution of the plastic fiber . . . . .	51
6.1	Design of the transmitter . . . . .	53
6.2	Transmitter with plastic optical fiber. . . . .	55
6.3	Transmitter with plastic optical fiber. . . . .	55
6.4	Prototype of the FPR. . . . .	56
6.5	Measure of the received power as a function of half beam width at the receiver plane normalized by receiver aperture radius. . . . .	59
6.6	Schmidt Cassegrain telescope . . . . .	59
6.7	Scheme for circular aperture diffraction . . . . .	60
6.8	Circular aperture diffraction . . . . .	61

6.9	Telescope aperture with central obstruction . . . . .	62
6.10	Annular aperture diffraction . . . . .	63
6.11	Workplace for measuring the diffraction disk at the focal plane of the Schmidt Cassegrain telescope . . . . .	64
6.12	Experimentally measured diffraction disk at the focal plane of the Schmidt Cassegrain telescope . . . . .	65
6.13	Configuration of the testbed which consist of Testing Transmitter and Fully Photonic Receiver. SFL - Single Frequency Laser, Lens 1 - plano-concave lens with focal length $f_1 = -30\text{ mm}$ , Lens 2 - plano- convex lens with focal length $f_2 = 300\text{ mm}$ , $f_{TEL}$ - focal length of the Cassegrain telescope, $f_A$ - focal length of the aspheric collimating lens, $l_g$ - length of the GRIN lens, $d_w$ - working distance of the GRIN lens. . . . .	66
6.14	Receiving fiber alignment deviations . . . . .	69
6.15	The coupling loss of the FPR as a function of the lateral deviation. .	70
6.16	The coupling loss of the FPR as a function of the defocus deviation. .	71
6.17	The coupling loss of the FPR as a function of angular deviation. . . .	71
6.18	Testbed for testing of the fully photonic receiver . . . . .	72
6.19	Scheme for the measurement of coupling loss . . . . .	72
6.20	The coupling loss of the FPR as a function of the lateral deviation. .	73
6.21	The coupling loss of the FPR as a function of the defocus deviation. .	73
6.22	Concept of the fully photonic link. . . . .	74

# List of Tables

5.1	Parameters of the Lenses . . . . .	47
5.2	Parameters of the optical fibers . . . . .	50
6.1	Radius and relative power within the central diffraction disk . . . . .	63
6.2	Parameters of the testbed . . . . .	70
6.3	Link budget. . . . .	75

# INTRODUCTION

For about 30 years, Free-Space Optical (FSO) systems have been gaining a specific place in the wireless technology area. The FSO system is line of sight technology which is designed to transmit information with a modulated infrared laser beam from one point to another in free space. On the other side of the link the information is received and demodulated. The application of these systems is advantageous for high speed point to point communication links in an urban area where the last mile problem arises. Another application of FSO system is in space-to-ground links. FSO technology brings advantages, e.g. high bandwidth, a license free band, no electromagnetic interference, and quick deployment. High directivity of the laser beam ensures more security of conveyed information but also brings a more difficult alignment procedure in comparison with the Radio Frequency (RF) system. The most serious drawback of FSO systems is their dependence on the state of the atmosphere causing deterioration of the FSO system's availability. Hence, the FSO system can be regarded as an atmospheric sensor. The performance of the FSO terminals and transmission of the optical wave through the atmosphere are affected mainly by atmospheric turbulence, fog, snow, wind, rain, background radiation, etc.

Constituent particles of the atmosphere cause absorption and scattering. These phenomena have the most serious impact on the FSO link availability. A power margin of the link working in foggy conditions has to be set appropriately to overcome fog attenuation and thus reduce the probability of fade. Another atmospheric effect which has an essential impact on the performance of FSO systems is atmospheric turbulence. Atmospheric turbulence leads to fluctuation of the optical intensity in the plane of the receiving aperture. A more detailed description of the atmospheric turbulence phenomenon is mentioned in Chapter 1.

This unwanted effect caused by atmospheric turbulence can be mitigated by a number of techniques. Basic techniques for mitigating received power fluctuations include aperture averaging and spatial diversity [1, 2, 3, 4, 5] in transmission as well as in reception. Another widely discussed technique is the usage of random optical beams. It is already known that the application of different beam shapes (Flattened Gaussian (FG) beams, Bessel-Gaussian beams, etc.) increases the reliability and availability of FSO systems. The scintillation index of Bessel-Gaussian beams propagating in turbulent media was studied theoretically in [6, 7]. The application of nondiffracting beams with different degrees of coherence in FSO systems was experimentally tested in [8].

In this thesis we are focusing only on usage of FG beams in FSO systems. The propagation of the FG beam in a turbulent atmosphere has been extensively studied theoretically in [9, 10, 11]. The usage of FG beams is advantageous from a

practical point of view. The generation of Airy beams, Bessel-Gaussian beams, etc. requires special optical devices such as an axicon or spatial light modulator. On the other hand, generating an FG beam is relatively inexpensive with optical components such as a diffuser, refraction optics and lenslet array. This thesis will discuss the propagation of FG beams in a turbulent atmosphere. We simulated propagation of the Gaussian and FG beam in a weak and moderate atmospheric turbulent medium. The thesis also discusses the selection of appropriate FG beam width in FSO transmitters and aperture averaging effect in FSO receivers.

Photonic components usually used for optical fiber communication are nowadays utilized in fully optical FSO links. It means that the light is not converted from optical to electrical domain, but the received light is directly coupled into the optical fiber. The received light can be advantageously amplified by an EDFA and filtered by a fiber filter. In the sixth chapter the concept of the fully photonic receiver and transmitter is discussed.

# 1 STATE OF THE ART

This chapter gives an overall view on problem of propagation of optical wave in random atmospheric media. A laser beam propagating in the atmosphere experiences energy losses owing to absorption and scattering on gases and particulates of the atmosphere. Scattering of the optical wave is divided into two groups. When the particles are smaller than the wavelength of the light we are talking about Rayleigh scattering. Scattering by particles comparable in size with wavelength is called Mie scattering. Scattering by much larger particles is described by geometrical optics models. Attenuation caused by absorption ( $A_A$ ) and scattering ( $A_S$ ) is called extinction  $\alpha(\lambda)$  [12].

$$\alpha(\lambda) = A_A + A_S. \quad (1.1)$$

The attenuation due to absorption or scattering has the most serious impact on the FSO link availability and reliability. Because the atmospheric absorption and scattering are strongly dependent on wavelength, the attenuation can be minimized by correct wavelength selection. Another usually used method is to increase the power of the transmitter. If the attenuation is caused by fog, which has local character, route diversity scheme can be used. In that case, communication is rerouted through other link which is not affected by foggy condition [13].

A laser beam is not affected only by absorption and scattering, but also experiences amplitude and phase fluctuations due to random distribution of the refractive index of air. The distribution is random in time and in space too. The next section deals with the problem of atmospheric turbulences.

## 1.1 Atmospheric turbulences

Air movements in the atmosphere can be laminar or turbulent or both at the same time. The parameter which defines the transition from laminar to turbulent motion is Reynolds number [14]

$$Re = \frac{uL}{v_m}, \quad (1.2)$$

where  $u$  is an air velocity,  $L$  is a space scale of the flow process, and  $v_m$  is an air kinematic viscosity. When the flow of the atmosphere exceed the critical Reynolds number, the flow becomes chaotic and changes from laminar to turbulent [12].

Atmospheric turbulence is one of the most significant phenomena in atmospheric transmission medium. Temperature ( $T$ ) and index of refraction ( $n$ ) differences between the earth's surface and the atmosphere with wind variations create local unstable air masses which are broken up into turbulent whirls sometimes called eddies. The linear size of these eddies ( $l$ ) varies from millimetres (small scales  $l_0$ ) to

hundreds of meters (large scales  $L_0$ ). The continuous cascade of eddies is formed between this two scales ( $l_0 < l < L_0$ ) and is called inertial range. The eddies smaller than small scales ( $l < l_0$ ) belong to dissipation interval where they are changed to heat. The eddies bigger than large scales ( $l > L_0$ ) are broken and the turbulence disappear. The characteristics of the fluctuations may be expressed by a structure function of refractive index  $D_n(\mathbf{r})$

$$D_n(\mathbf{r}_1, \mathbf{r}_2) = \langle [n(\mathbf{r}_1) - n(\mathbf{r}_2)]^2 \rangle, \quad (1.3)$$

where  $n(\mathbf{r}_1)$  is refractive index at point  $\mathbf{r}_1$  and  $n(\mathbf{r}_2)$  is refractive index at point  $\mathbf{r}_2$ . Sharp brackets denote an ensemble average. For homogeneous and isotropic turbulences the dependency on distance  $r$  can be written as

$$D_n(\mathbf{r}) = C_n^2 r^{2/3}, \quad l_0 \ll r \ll L_0 \quad (1.4)$$

and

$$D_n(\mathbf{r}) = C_n^2 l_0^{-4/3} r^2, \quad r \ll l_0, \quad (1.5)$$

where  $l_0$  is inner scale and  $L_0$  is outer scale of turbulences [12].

The refractive index structure parameter  $C_n^2$  constitutes a measure of the turbulence. Typically, the values of  $C_n^2$  range from  $10^{-16} \text{ m}^{-2/3}$  for weak turbulence to  $10^{-12} \text{ m}^{-2/3}$  for strong turbulence. It has to be taken into account that the parameter  $C_n^2$  is dependent on height. The value of the parameter  $C_n^2$  is decreasing with increasing height. There are number of models which describes this dependency [15, 16]. This is very important especially for designing the space-to-ground (vertical) communication links. However for designing the horizontal free space optical link the parameter  $C_n^2$  is assumed to be constant over the entire propagation path.

Sometimes one has to estimate strength of turbulences from measured temperature gradient. For that case, the  $C_n^2$  parameter could be calculated from  $C_T^2$  which is structural characteristic of the temperature field. For dry air  $C_T^2$  to  $C_n^2$  can be recalculated according to following relation [14]

$$C_n = \frac{10^{-6}}{T} \left( \frac{77.6 P_{\text{atm}}}{T} + \frac{0.584 P_{\text{atm}}}{T \lambda^2} \right) C_T, \quad (1.6)$$

where  $P_{\text{atm}}$  [mbar] is atmospheric pressure,  $T$ [K] is temperature and  $\lambda$  is the wavelength.

Atmospheric turbulence leads to irradiance fluctuations, beam spreading, beam wandering and loss of spatial coherence of a laser beam [12].

Various frequency component in time varying electrical signal could be determined by Fourier transform method. Similar concept can be used in determining the different eddy sizes contributing to the refractive index of random medium [17].

In order to simulate refractive index fluctuations, different power spectrum models can be used. The turbulence spectrum links random fluctuations in the refractive index with optical turbulence effects on laser propagation [18]. The first and widely used model is Kolmogorov power spectrum which is valid only over the inertial range

$$\Phi_n(\kappa) = 0.003C_n^2\kappa^{-11/3}, \quad 1/L_0 \ll \kappa \ll 1/l_0, \quad (1.7)$$

where  $\kappa$  is wave number defined by  $\kappa_l = 2\pi/l_0$  or  $\kappa_0 = 2\pi/L_0$ . The spectrum wavenumber  $\kappa$  is not the same as wavenumber for electromagnetic propagation  $k = 2\pi/\lambda$ . If inner and outer scale effects must be taken into account, von Kármán spectrum [8]

$$\Phi_n(\kappa) = 0.003C_n^2 \frac{\exp(-\kappa^2/\kappa_m^2)}{(\kappa^2 + \kappa_0^2)^{11/6}}, \quad 0 \leq \kappa < \infty \quad (1.8)$$

or modified von Kármán spectrum can be applied where  $\kappa_m = 5.92/l_0$  and  $\kappa_0 = 1/L_0$ .

## 1.2 Propagation of optical wave through turbulent medium

As was stated before, the three phenomena that affect laser beam propagation through the atmosphere are scattering, absorption and atmospheric turbulence [12]. A laser beam can quickly lose a part of its energy and, moreover, this loss can lead to beam quality degradation. Signal amplitude is randomly modulated and phase front is distorted.

### 1.2.1 Coherence

As known, a laser is a source of light with high temporal and spatial coherence. Coherence of light is reduced by passing through the turbulent media, where the wavefront is randomly distorted. This random process has to be treated statistically by using theory of optical coherence. Spatial coherence is the correlation of the electric fields at two different positions ( $\mathbf{r}_1, \mathbf{r}_2$ ) on the same wave front. Temporal coherence is the correlation between the fields at two different times ( $t_1, t_2 = t_1 + \tau$ ) in the same wave train. We can simply say that spatial coherence is the ability of light interfere with spatial shifted version of itself and temporal coherence is the ability of light interfere with time delayed version of itself. The mutual coherence function  $\Gamma$  combines both spatial and temporal characteristics in one single term. It is defined as

$$\Gamma(\mathbf{r}_1, \mathbf{r}_2, \tau) = \langle U(\mathbf{r}_1, t + \tau)U^*(\mathbf{r}_2, t) \rangle \quad (1.9)$$



where  $U(\mathbf{r}_1, t)$  is the complex electric field at position  $\mathbf{r}_1$ ,  $U(\mathbf{r}_2, t)$  is the complex electric field at position  $\mathbf{r}_2$ ,  $t$  is time and  $\tau$  is time delay [12]. If the time delay is set to  $\tau = 0$ , the mutual coherence at the receiver plane is only function of position

$$\Gamma(\mathbf{r}_1, \mathbf{r}_2, L) = \langle U(\mathbf{r}_1, L)U^*(\mathbf{r}_2, L) \rangle \quad (1.10)$$

where  $L$  is the propagation distance. It is called mutual intensity.

The normalized mutual coherence function  $\gamma_{12}$  is given with relation (1.11) and is called the complex degree of coherence [12]

$$\gamma_{12}(\mathbf{r}_1, \mathbf{r}_2, L) = \frac{\Gamma(\mathbf{r}_1, \mathbf{r}_2, L)}{\sqrt{\Gamma(\mathbf{r}_1, \mathbf{r}_1, L)\Gamma(\mathbf{r}_2, \mathbf{r}_2, L)}}, \quad (1.11)$$

where  $\Gamma(\mathbf{r}_1, \mathbf{r}_1, L)$  is intensity at the point  $r_1$  and  $\Gamma(\mathbf{r}_2, \mathbf{r}_2, L)$  is intensity at point  $r_2$ . The spatial coherence radius of the wave is defined where the modulus of the complex degree of coherence falls to  $1/e$  [19].

Loss of spatial coherence limits the effective aperture size of heterodyne detection optical receivers [12]. The coherence radius is useful for determining the size of the receiver aperture through a process called aperture averaging and also for determining the separation distance of detectors in a multiple receiver system [20]. In Ref. [12] spatial coherence radius for the infinity plane wave  $\rho_{pl}$  and spherical wave  $\rho_{sp}$  is given by

$$\rho_{pl} = (1.46 C_n^2 k^2 L)^{-3/5}, \quad l_0 \ll \rho_{pl} \ll L_0, \quad (1.12)$$

$$\rho_{sp} = (0.55 C_n^2 k^2 L)^{-3/5}, \quad l_0 \ll \rho_{sp} \ll L_0 \quad (1.13)$$

where  $k$  is the wave number and  $L$  is the distance between the optical transmitter and receiver. For a collimated Gaussian-beam wave, the spatial coherence radius  $\rho_g$  is approximated by [12]

$$\rho_g = (0.55 C_n^2 k^2 L (a + 0.62 \Lambda^{11/6}))^{-3/5}, \quad l_0 \ll \rho_g \ll L_0 \quad (1.14)$$

where the Fresnel ratio  $\Lambda$  is for a beam half width at the receiver plane  $w$  defined by

$$\Lambda = \frac{2L}{kw^2}. \quad (1.15)$$

Parameter  $a$  is defined by

$$a = \frac{1 - \Theta^{8/3}}{1 - \Theta}, \quad \Theta \geq 0 \quad (1.16)$$

where  $\Theta$  is the refractive beam parameter and can be calculated by

$$\Theta = \frac{1}{\left[1 + \left(\frac{2L}{kw_0^2}\right)^2\right]} \quad (1.17)$$

where  $w_0$  is beam half width at the waist.

Usually the statistical measure of coherence is determined by atmospheric coherence width  $r_0$ . This parameter is known as Fried parameter. The Fried parameter could be interpreted as the aperture over which there is approximately one radian of root-mean-square phase aberration. The second interpretation is that, it is aperture which has the same resolution as a diffraction limited aperture in the absence of the turbulence [21]. In astronomical seeing this parameter is called "seeing parameter". Large value of the  $r_0$  means good seeing and small value of the  $r_0$  bad seeing. This parameter is related to the plane wave spatial coherence by [22]

$$r_0 = 2.1 \rho_{pl} = (0.423 C_n^2 k^2 L)^{-3/5}. \quad (1.18)$$

The Fried parameter is described as a function of wavelength, refractive index structure parameter and propagation distance. If an undisturbed plane wave incident on receiver lens with diameter  $D_{RXA}$  and focal length  $f$ , the spot size at the focal plane is given by relation [21]

$$d_{spot, ideal} = \frac{\lambda}{D_{RXA}} f. \quad (1.19)$$

Due to atmospheric turbulence the incident plane wave is distorted and spot at the focal plane of the receiver became blurry. The spot size at the focal plane of the receiver is larger and has diameter

$$d_{spot, turb} = \frac{\lambda}{r_0} f. \quad (1.20)$$

According to [23], when the diameter  $D_{RXA}$  is smaller than Fried parameter  $r_0$  the resolution of the receiver is limited by the optics. The resolution is limited by the atmosphere when diameter of the receiver  $D_{RXA}$  is larger than  $r_0$ . A typical value of the Fried parameter for wavelengths from visible spectrum is between 10 to 20 cm. However thanks to dependency of  $r_0$  on wavelength, the Fried parameter is bigger for infra-red spectrum. The Fried parameter for wavelength 1550 nm lies between 30 to 70 cm.

### 1.2.2 Beam spreading

Small scale turbulence eddies cause distortion of the propagated optical wave (loss of spatial coherence) which leads to beam divergence beyond the pure diffraction predicted by theory. Then the beam diameter could be bigger than aperture of the receiver which decrease received power.

### 1.2.3 Beam wandering

The effect of beam wandering is caused by the turbulent cells with size larger than the laser beam diameter [12]. Laser beam passing through the turbulent cell is diverted from the original direction because of different refractive index of the turbulent cell. The redirection depends on the distance between transmitter and receiver plane, position of the turbulent cell in laser beam path, refractive index and the size of turbulent cell. Beam wandering can be evaluated by the root-mean square centroid displacement [24] which describes how laser beam moves at receiver plane. The rms displacement is given by the relationship

$$\langle r_c^2 \rangle = 2.87L^3 C_n^2 w_0^{-1/3}, \quad (1.21)$$

where  $L$  is the propagation distance and  $w_0$  is radius of the collimated Gaussian beam [12].

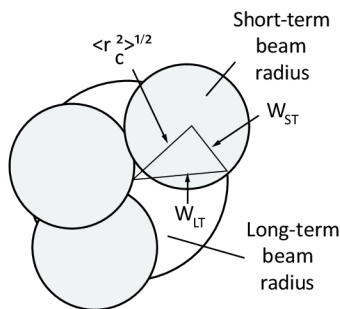


Fig. 1.1: Beam wander [12]

### 1.2.4 Angle of arrival

One of the effects caused by atmospheric turbulences, which have an essential impact on availability of the free space optical link, is fluctuations of the angle of arrival. The incident angle is defined as the angle between the direction of propagation of an optical wave which is incident to the plane of the receiving aperture and optical axis of the receiver [12]. As a consequence of angle of arrival fluctuation, the focused optical wave is shifted from the optical axis (image jitter) in the focal plane of the receiving system. Variance of the angle of arrival  $\beta_a$  for a plane wave is defined as

$$\beta_{a,pl} = \sqrt{2.91 C_n^2 L D_{RxA}^{-\frac{1}{3}}} \quad (1.22)$$

where  $L$  is distance between the transmitter and the receiver and  $D_{RxA}$  is diameter of the receiving aperture. According to Churnside it is possible to estimate variance

of the angle of arrival for a spherical wave [25]

$$\beta_{a,sp} = \sqrt{\frac{3}{8} 2.91 C_n^2 L D_{RXA}^{-\frac{1}{3}}}. \quad (1.23)$$

The equation 1.23 will be considered in the last chapter. The variance of the angle of arrival will be very important parameter during the assessment of the fully photonic receiver.

## 1.2.5 Optical scintillation

Atmospheric turbulences have also an effect on the distribution of the optical intensity in the propagated laser beam. Laser radiation is affected by turbulence and develops temporal and spatial fluctuations of irradiance observable at the receiver side. The degree of the fluctuation of the received signal is usually measured by scintillation index [18]

$$\sigma_I^2 = \frac{var(I)}{mean(I)^2} = \frac{\langle I^2 \rangle}{\langle I \rangle^2} - 1, \quad (1.24)$$

where *var* means variance and *I* is optical intensity. From equation 1.24 is apparent that scintillation index means normalized variance of optical intensity.

When an undisturbed plane wave or a spherical wave model is used, it is possible to describe optical scintillation by means of the Rytov variance [8]

$$\sigma_1^2 = K C_n^2 k^{7/6} L^{11/6}, \quad (1.25)$$

where *K* is the constant for plane wave 1.23 or for spherical wave 0.5, *k* is the wave number. Rytov variance  $\sigma_1^2$  represents the index of scintillation  $\sigma_I^2$  associated with plane wave or spherical wave during the weak fluctuation regime. Weak fluctuations of the optical intensity are characterized by  $\sigma_1^2 < 1$ , whereas strong fluctuations are associated with  $\sigma_1^2 > 1$ . For horizontal communication link the strength of the turbulence defined by  $C_n^2$  is taken to be constant whereas in case of vertical or slant path link the  $C_n^2(h)$  is function of altitude *h*. The previous scintillation equations (1.24, 1.25) are valid for point receiver. If aperture of the receiver has diameter *D* the aperture averaging effect has to be taken into account. The scintillation index for point receiver is then multiplied with parameter *A* also called Aperture Averaging Factor

$$A = \frac{\sigma_I^2(D)}{\sigma_I^2(0)}. \quad (1.26)$$

For weak fluctuation theory this factor can be estimated from following equation [26]

$$A = \left( 1 + 1.062 \frac{k D^2}{4L} \right)^{-7/8}. \quad (1.27)$$

Aperture averaging is one of the basic techniques that is used for mitigation of turbulence induced scintillation.

The equation 1.25 defines scintillation index of plane wave or spherical wave respectively for weak fluctuations condition. In FSO communications as a light source the lasers and laser diodes are usually used. The irradiation emanated from the laser can be defined as a circularly symmetrical Gaussian beam wave. The Gaussian beam wave at the transmitter plane is characterized by beam radius  $W_0$ , on axis intensity  $I_0$ , radius of curvature  $F_0$  and wave number  $k$ . The wave is represented by following equation [12]

$$U(r, 0) = I_0 \exp\left(-\frac{r^2}{W_0^2} - \frac{ikr^2}{2F_0}\right). \quad (1.28)$$

If the wave is propagated through the free space, Gaussian beam wave at the receiver side is given by

$$U(r, L) = \frac{I_0}{\Theta_0 + i\Lambda_0} \exp\left(ikL - \frac{r^2}{W_2} - i\frac{kr^2}{2F}\right), \quad (1.29)$$

where  $\Theta_0 = 1 - L/F_0$  is refraction parameter,  $\Lambda_0 = 2L/kW_0^2$  is diffraction parameter in the plane of the transmitter,  $W$  is beam width and  $F$  is radius of curvature at the receiver side.

Thereafter the refraction and diffraction parameters are  $\Theta = 1 - L/F$ ,  $\Lambda = 2L/kW^2$ , beam width and radius of curvature are defined by  $W = W_0\sqrt{\Theta_0^2 + \Lambda_0^2}$  or  $F = F_0(\Theta_0^2 + \Lambda_0^2)(\Theta_0 - 1)/(\Theta_0^2 + \Lambda_0^2 - \Theta_0)$ . In presence of turbulence within the propagation path the effective parameters have to be defined: effective diffraction parameter  $\Lambda_e = \Lambda/(1 + 1.63\sigma_1^{12/5}\Lambda)$  and effective beam width  $W_e = W\sqrt{(1 + 1.63\sigma_1^{12/5}\Lambda)}$ .

The radial and longitudinal component of Gaussian beam wave scintillation index for weak and strong turbulence regime is represented by [12, 27]

$$\sigma_I^2(r, L) = 4.42\sigma_1^2\Lambda_e^{5/6}\frac{r^2}{W_e^2} + \exp\left[\frac{0.49\sigma_B^2}{(1 + 0.56\sigma_B^{12/5})^{7/6}} + \frac{0.51\sigma_B^2}{(1 + 0.69\sigma_B^{12/5})^{5/6}}\right] - 1, \quad (1.30)$$

where  $\sigma_B^2$  is Rytov variance for a beam wave defined by

$$\sigma_B^2 \cong 3.86\sigma_1^2 \left\{ 0.4 \left[ (1 + 2\Theta)^2 + 4\Lambda^2 \right]^{5/12} \cos \left[ \frac{5}{6} \arctan \left( \frac{1 + 2\Theta}{2\Lambda} \right) \right] - \frac{11}{6} \Lambda^{5/6} \right\}. \quad (1.31)$$

The formation of irradiance fluctuation is involved by inner scale and outer scale components of the turbulences as well. For that case, scintillation index which consider both scales are proposed by [12]. In weak fluctuation regime outer and inner scales have negligible effect on scintillation index.

### 1.3 Beam shapes

The intensity distribution at the plane of the transmitter in FSO link can be defined by number of beam shapes. During the propagation in free space or in atmosphere each of the beam shapes exhibit different properties. For instance, different scintillation index, spreading, beam wandering and others. The various types of beam shapes have been extensively studied, e.g., Hermite – Gaussian beams, Cos Gaussian beams, Cosh Gaussian beams, Laguerre Gaussian beams, Dark Hollow beams,  $J_0$  – Bessel beams,  $I_0$  – Bessel beams, Flattened – Gaussian beams, etc.

#### Hermite – Gaussian beams

The field of the higher order of the Hermite – Gaussian modes (Fig. 1.7) of a laser is given by

$$U(x, y, z = 0) = H_m \left( \sqrt{2} \frac{x}{w_0} \right) H_n \left( \sqrt{2} \frac{y}{w_0} \right) \exp \left( -\frac{x^2 + y^2}{w_0^2} \right), \quad (1.32)$$

where  $m, n = 0, 1, 2, \dots$ ,  $w_0$  is the radius of the beam and  $H_m(x)$  is the  $m$ -th Hermite polynomial [23]. It was showed in literature [23], that the Hermite Gaussian beams and Laguerre Gaussians beam suffer less on beam spreading caused by turbulence than Gaussian beams. From the longitudinal intensity distribution is obvious that the shape of the beam is not changing during propagation without atmospheric turbulence (Fig. 1.3).

#### Laguerre Gaussian beams

Laguerre Gaussian beam (Fig. 1.4) at the transmitter plane is defined as follows [28]

$$U(\mathbf{s}, \phi, z = 0) = \left( \frac{\sqrt{2}s}{w_0} \right)^l L_p^l \left( \frac{2s^2}{w_0^2} \right) \exp \left[ -\frac{s^2}{w_0^2} + il\phi \right] \quad (1.33)$$

where  $L_p^l$  is the associate Laguerre polynomial,  $w_0$  is the radius of the beam, and  $(\mathbf{s}, \phi)$  is cylindrical coordinate system. When the angular mode number  $l$  and radial mode number  $p$  are set to zero, the field is reduced to the fundamental Gaussian mode. Scintillation analysis carried out by [29] proved that scintillation index of this beam is lower than scintillation index of the Gaussian beam. The lowest scintillation index was achieved when parameter  $l$  is equal to zero and parameter  $p$  is as high as possible.

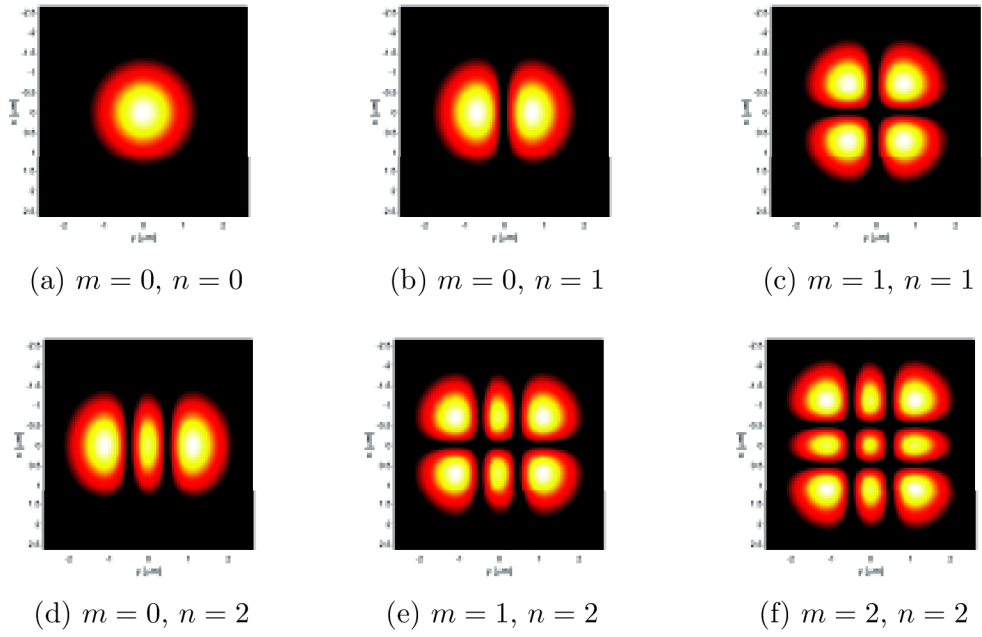


Fig. 1.2: Simulated field distribution of the Hermite–Gaussian beams for different  $m$  and  $n$  parameters

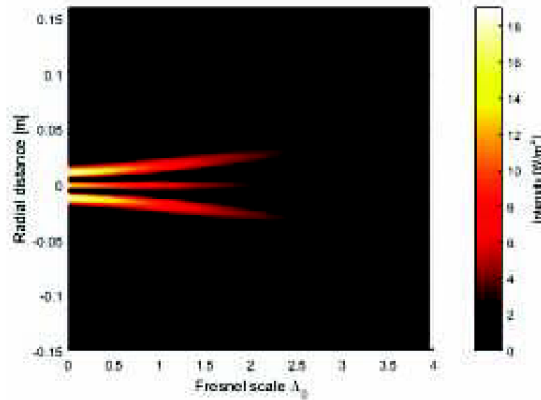


Fig. 1.3: Longitudinal intensity distribution of the Hermite – Gaussian beam ( $m, n=2$ ) beam for vacuum propagation

### Cos and Cosh Gaussian beams

Rectangular Cos Gaussian beam (Fig. 1.5) and Cosh Gaussian beam (Fig. 1.6) at the transmitter plane is defined by

$$U(x, y, z = 0) = \exp\left(-\frac{x^2 + y^2}{w_0^2}\right) \cos(\beta_x x) \cos(\beta_y y) \quad (1.34)$$

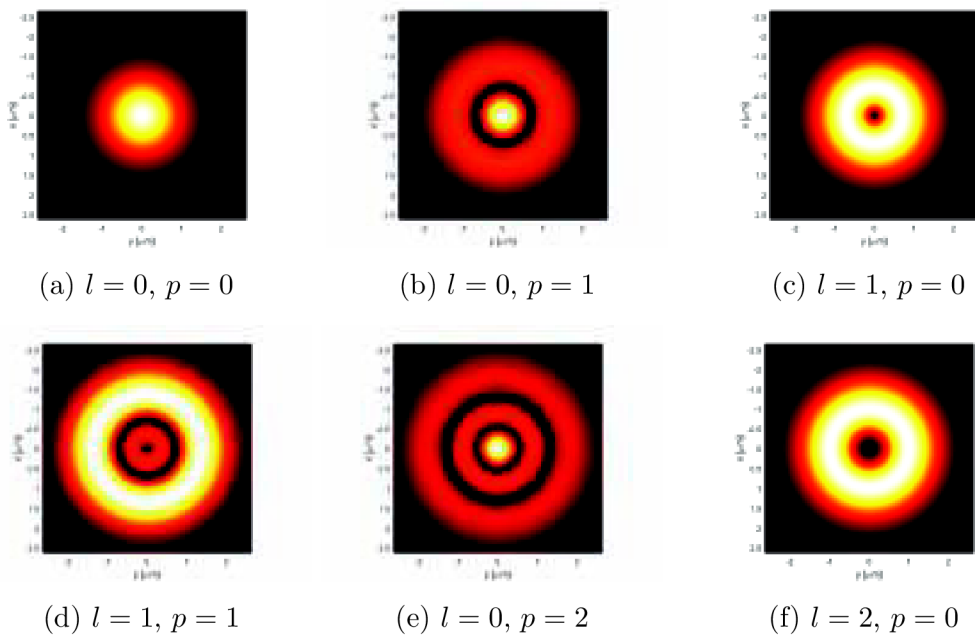


Fig. 1.4: Simulated field distribution of the Laguerre Gaussian beams for different  $l$  and  $p$  parameters

and

$$U(x, y, z = 0) = \exp\left(-\frac{x^2 + y^2}{w_0^2}\right) \cosh(\Omega_0 x) \cosh(\Omega_0 y) \quad (1.35)$$

where  $w_0$  is radius of the beam,  $\beta$  is the parameter associated with cos part and  $\Omega_0$  is the parameter associated with the cosh part. The interesting thing about cos and cosh Gaussian beams is that they are reciprocal during propagation in free space. It means that the Cos Gaussian beam is transformed during propagation to Cosh Gaussian beam and vice versa [30].

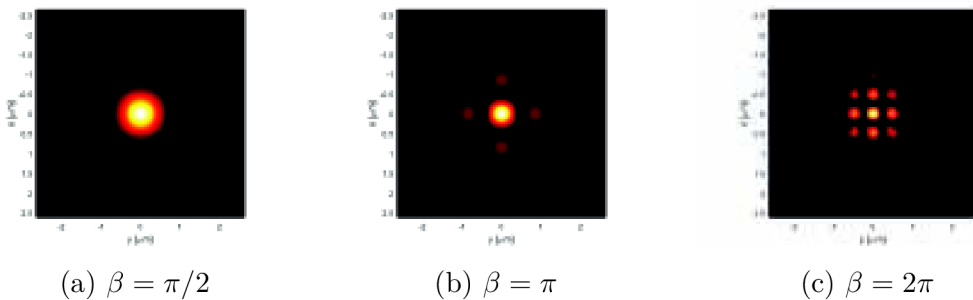


Fig. 1.5: Simulated field distribution of the Cos Gaussian beams for different  $\beta$  parameters



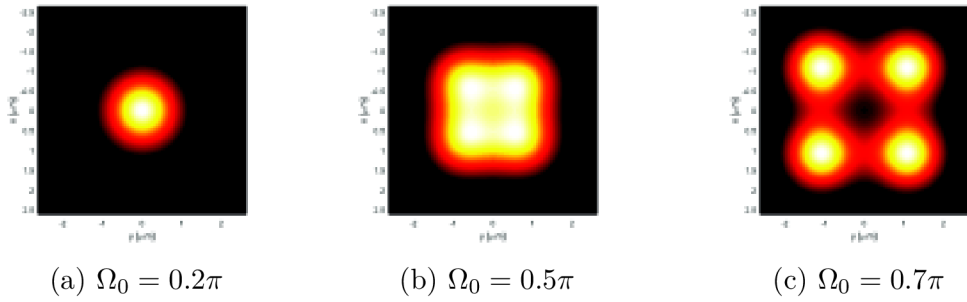


Fig. 1.6: Simulated field distribution of the Cosh Gaussian beams for different  $\Omega_0$  parameters

Scintillation index of the Cosh Gaussian beam is lower for longer propagation distance and lower source size; on the contrary, scintillation index of the Cos Gaussian beam is lower for lower propagation distance and large source size [31].

### Dark hollow beams

Dark hollow beams (Fig. 1.7 ) are significant for zero central intensity. They are usually used in applications like optical tweezers, optical trapping of particles, etc. The computer generated hologram and spatial filtering is normally used to generate these beams [32]. The field of the dark hollow beam is given by subtraction of primary and secondary Gaussian beam.

$$E(\mathbf{s}, z = 0) = \left[ \exp\left(-\frac{2s^2}{w_1^2}\right) - \exp\left(-\frac{2s^2}{w_2^2}\right) \right] \quad (1.36)$$

where  $w_1$  and  $w_2$  is half – width of the primary and secondary Gaussian beam and  $\mathbf{s}$  is transverse vector. The intensity distribution within the beam is changed during propagation in vacuum. The doughnut shape is transformed to Gaussian Fig. 1.8. According to [33], dark hollow beam shows lower scintillation level in comparison with Gaussian beam in weak turbulence regime for longer propagation distance.

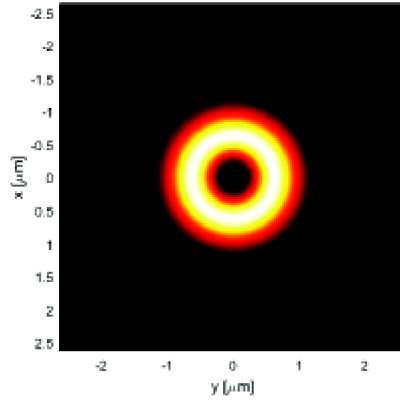


Fig. 1.7: Simulated field distribution of the dark hollow beam for  $w_1 = 0.5 \text{ mm}$  and  $w_2 = 0.3 \text{ mm}$

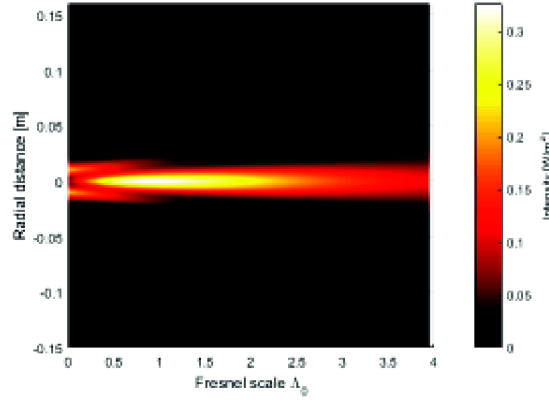


Fig. 1.8: Longitudinal intensity distribution of the Dark hollow beam for vacuum propagation

### Bessel – Gaussian beams

Bessel beams (Fig. 1.9, Fig.1.10) are important for their non – diffractive properties. Field of the Bessel – Gaussian beam is given by

$$E(\mathbf{s}, z = 0, \omega) = J_n(\alpha s) \exp(in\theta) \exp\left(-\frac{s^2}{w_0^2}\right) \quad (1.37)$$

where  $n$  denotes the topological charge,  $J_n$  is the Bessel function,  $\alpha$  and  $w_0$  are the width parameters and  $\omega$  is the angular frequency and  $\mathbf{s}$  is transverse vector. From the scintillation analysis [7] of the lowest order Bessel – Gaussian beams is clear that scintillation index in weakly turbulent atmosphere is lower than scintillation of the Gaussian beam. However, at long propagation distances and large beam widths the scintillation index become higher in comparison with Gaussian beam.

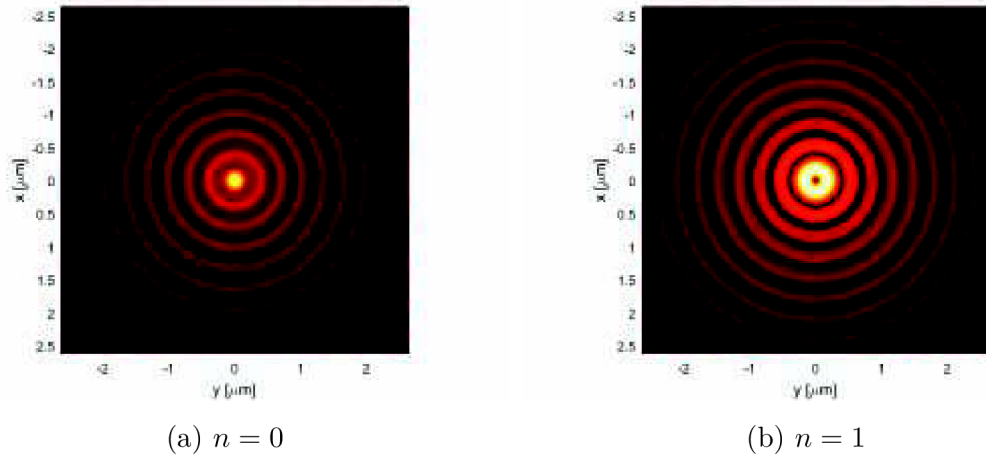


Fig. 1.9: Simulated field distribution of the first kind Bessel – Gaussian beams

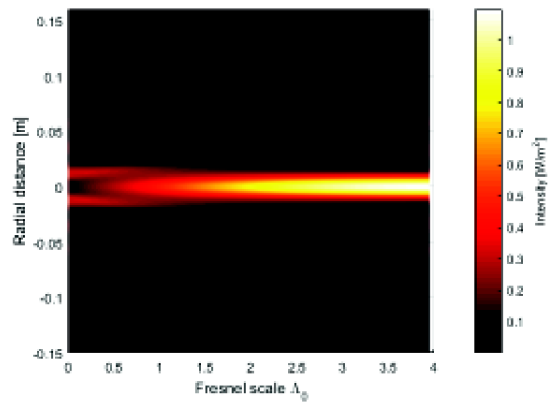


Fig. 1.10: Longitudinal intensity distribution of the Bessel – Gaussian beam ( $n=1$ ) for vacuum propagation

## 2 OBJECTIVES OF THE THESIS

The dissertation thesis is focused on analysing the distribution of optical intensity within a radiated laser beam at the transmitter and receiver plane which is affected by propagation through free space as well as through the atmosphere. The aim of the thesis is to determine the optimal intensity distribution of a laser beam at the transmitter plane which is minimally affected by turbulence during the propagation process. As a consequence, the scintillation index should be reduced. There are a number of theoretical studies aimed at propagation of the Flattened Gaussian beam (top-hat beam), despite the lack of experimental work in this area. The novelty of this dissertation thesis consists in the utilization of a top-hat beam shaper of the FSO link. The most important objectives of the thesis are as follows:

- The first aim is to create a simulation program for studying the propagation of an arbitrary optical wave through the atmosphere. The program will be able to simulate different strengths of turbulences with a specified turbulence power spectrum.
- Based on the findings of the theoretical analysis and simulations, the second aim is to design a laser beam transmitter with the ability to shape a Gaussian beam to a top-hat beam.
- The third aim is to design and practically validate properties of a fully photonic link which will be able to transmit an optical signal without the need to convert it into the electrical domain. Data gathered during experimental testing will be compared with theoretical assumptions.

### 3 NUMERICAL SIMULATION OF OPTICAL WAVE PROPAGATION

In order to study propagation properties of the arbitrary optical wave, the simulation program in MATLAB was utilized. The program was based on Split-step method [34]. This method is widely used for simulation of optical waves in inhomogeneous media like atmosphere. Algorithm for single step  $\Delta z$  can be written as [35]

$$U(x, y, z + \Delta z) = \exp(-i\Delta n k \Delta z) \mathcal{F}^{-1} \left\{ \exp \left[ \frac{i(k_x^2 + k_y^2) \Delta z}{2k} \right] \mathcal{F} \{U(x, y, z)\} \right\}. \quad (3.1)$$

An initial wave is located at a source plane ( $z = 0$ ) and propagates along the  $z$  axis (Fig.3.1). Path length  $L$  is then divided into a series of  $M_{step}$  step. Width of each step can be calculated as  $\Delta z = L/M_{step}$ . In the centre of this interval ( $\Delta z/2$ ) the phase screen was placed. From (3.1) it is clear that propagation between every step takes place in transformed domain (frequency domain). After each step the optical wavefront is transformed back to spatial domain, where a phase screen is used to simulate the atmospheric effect.

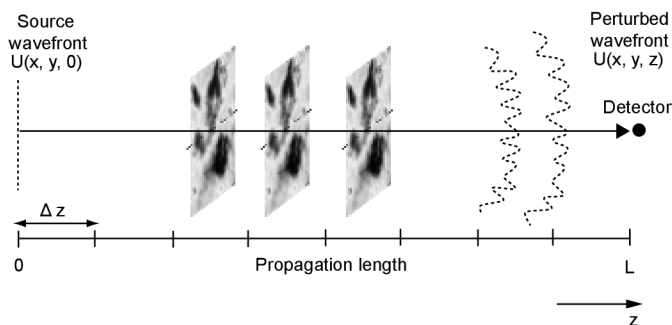


Fig. 3.1: Split-step propagation method interpretation [36]

#### 3.1 Phase screen modeling

For the simulation of propagation of the optical beam through turbulent media, spatial statistic of refractive turbulences is needed, because of randomly varying index of refraction. The initial wavefront is propagated through regions of turbulences which cause variations in phase across the reference wavefront. As a result a variation in irradiance across the wavefront is observed. The problem of creating phase screens is one of generation individual realizations of a random process [34]. There are many available options how to generate phase screens. In [37] algorithm based

on Zernike expansion of randomly weighted Karhunen-Loeve functions is presented. The advantage of this method is faster execution time in comparing with FFT based method however restriction to a circular aperture can be problematic. The simplest way is to generate phase screen with FFT-based method, where the screen is generated in spectral domain with the selected spectral turbulence model. Shortcoming of this method is that do not reflect low frequency phase variations such as tilt because the spatial frequency grid is not sampling low enough. This problem can be overcome with sub-harmonics method, where limited number of sub-harmonics is used at low frequencies [34]. Phase screen created by this method is depicted in Fig. 3.2.

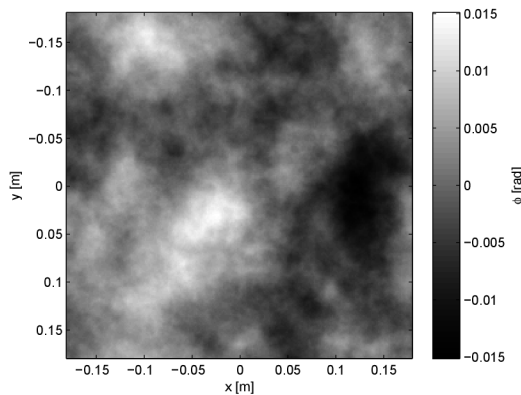


Fig. 3.2: One realization of the phase screen created by sub-harmonics method

## 3.2 Gaussian beam propagation simulation

The numerical simulation was used to simulate propagation of collimated Gaussian beam with wavelength 1550 nm in turbulent atmosphere with  $C_n^2 = 10^{-14} \text{ m}^{-2/3}$ . The on-axis scintillation index was calculated according equation (1.24) from 100 random runs. I performed simulation with 30 random phase screens each one has 256x256 grid points. The simulated results were compared with theoretical predictions specified by (1.30). One of the random realizations is depicted in Fig. 3.3.

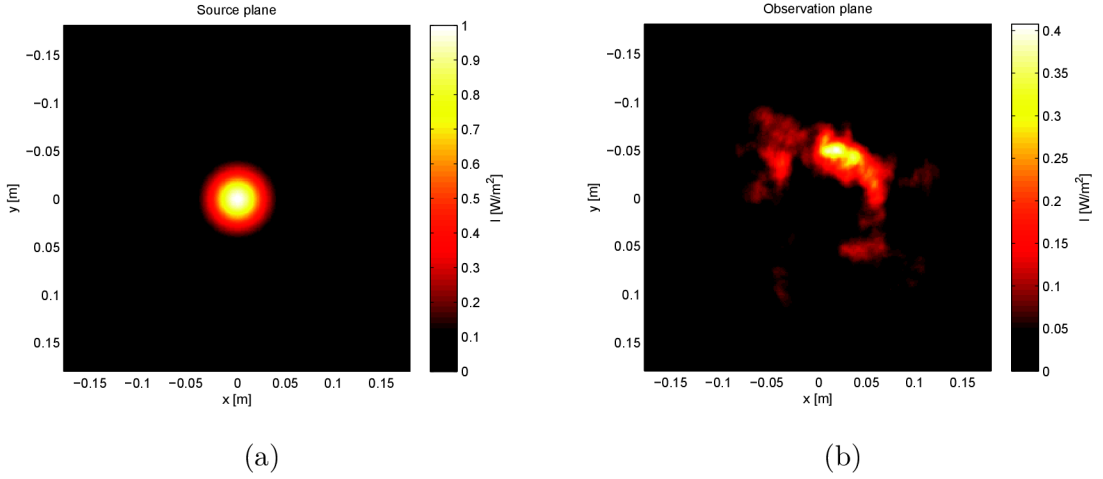


Fig. 3.3: Initial Gaussian beam (a) and irradiance resulting from turbulence propagation (b) for  $C_n^2 = 10^{-14} \text{ m}^{-2/3}$ .

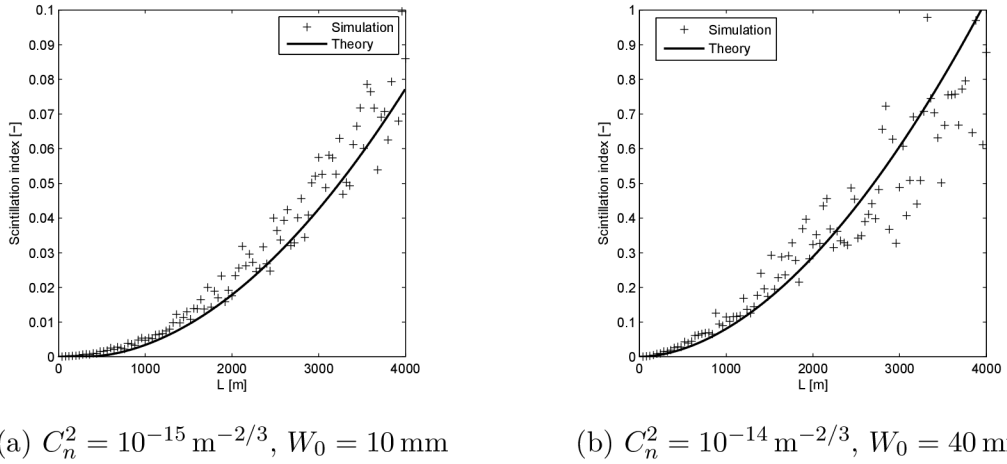


Fig. 3.4: Theoretical and simulated scintillation index of collimated Gaussian beam as a function of propagation length

From Fig. 3.4 it is evident that the simulated scintillation values are overspread as a consequence of low number of random runs. However good agreement between the simulation and theoretical expectation was achieved. This method of beam propagation simulation is relevant but the parameters of the simulation have to be set appropriately.

## 4 FLATTENED-GAUSSIAN BEAM

I need to define a beam with a uniform distribution of optical intensity in the profile. Fermi-Dirac, Super-Gaussian or flattened Lorentzian approximations can be used for mathematical expressions of a top-hat beam. The following expression describes a field of the Fermi-Dirac beam  $U_{FD}(\mathbf{s})$  [38]

$$U_{FD}(\mathbf{s}, z = 0) = \frac{1}{1 + \exp[\gamma(\frac{s}{R_0} - 1)]}, \quad (4.1)$$

where  $\mathbf{s}$  is transverse vector,  $R_0$  is the radius at which the intensity has fallen to half of its value on the axis,  $\gamma$  is a dimensionless parameter which determines the degree of beam flatness and  $g_0$  is the maximal value of optical intensity on the beam axis.

The next possible approximation of the top-hat beam can be provided by the Super-Gaussian function  $U_{SG}$  [38]

$$U_{SG}(\mathbf{s}, z = 0) = \exp \left[ -2 \left( \frac{s}{R_0} \right)^p \right], \quad (4.2)$$

where  $p$  is a dimensionless parameter which determines the degree of beam flatness. Fig.4.1a shows Super-Gaussian functions with different parameters  $p$ . The flatness of the beam profiles increases with increasing values of the parameters  $\gamma$  and  $p$ . The output beam distribution can be characterized by the flattened Lorentzian function as well

$$U_{FL}(\mathbf{s}, z = 0) = \left( \frac{1}{\pi R_{FL}^2} \right) \left[ \frac{1}{\left[ 1 + \left( \frac{s}{R_{FL}} \right)^q \right]^{\frac{2}{q}}} \right], \quad (4.3)$$

where  $R_{FL}$  is width of the flattened beam profile. Steepness of the beam is determined by shape parameter  $q$ . The distribution of optical field  $U_{FL}$  for different parameters  $q$  is shown in Fig. 4.1b. The top-hat beam can be also represented as a superposition of  $N$  Gaussian beams [39]

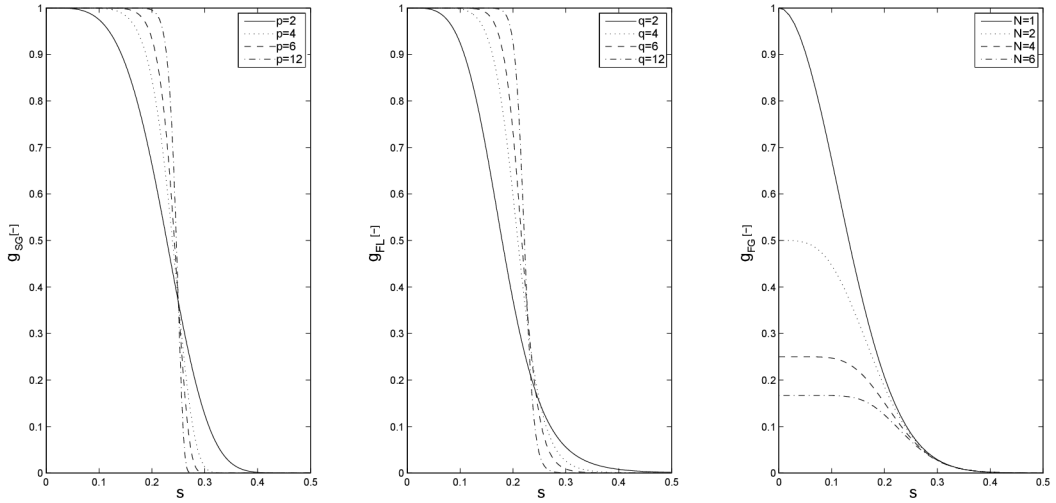
$$U_{FG}(\mathbf{s}, z = 0) = \sum_{n=1}^N \frac{(-1)^{n-1}}{N} \binom{N}{n} \exp \left( -\frac{ns^2}{2a_s^2} \right), \quad (4.4)$$

where  $a_s$  is beam radius.

For a mathematical expression of the circularly symmetrical FG beam at the transmitter plane (TXA) located in  $z = 0$ , approximation proposed by Bagini et al. [40] can be used

$$U_{TXA}(\mathbf{s}, z = 0) = A \exp \left( -\frac{(N+1)s^2}{w_0^2} \right) \sum_{m=0}^N \frac{1}{m!} \left( \frac{\sqrt{N+1}s}{w_0} \right)^{2m}. \quad (4.5)$$





(a) Super-Gaussian approximation (b) Flattened Lorentzian approximation (c) Flattened Gaussian approximation

Fig. 4.1: Mathematical functions for representation top-hat beams

The parameter  $A$  is amplitude of the field distribution,  $\mathbf{s}$  is transverse vector at TXA plane,  $s$  is radial distance from the optical axis,  $w_0$  is beam half-width at TXA and  $N \geq 0$  is flatness order [41]. With increasing  $N$ , the FG profile becomes flatter (Fig. 4.2). If the parameter  $N$  is equal to zero, the FG beam turns into a Gaussian beam. I used this expression in order to determine intensity distribution  $U_{TXA}$  at the transmitter plane.

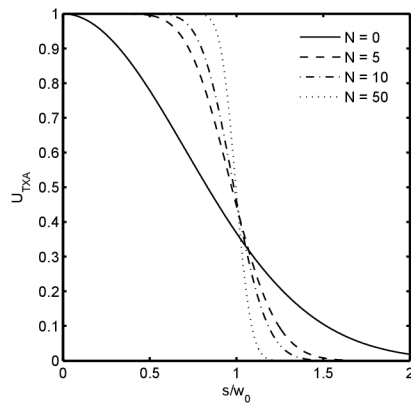


Fig. 4.2: FG beam for various  $N$  parameters as a function of radial distance normalized with beam half-width

The intensity distribution at the receiver plane  $U_{RXA}$  can be determined by using

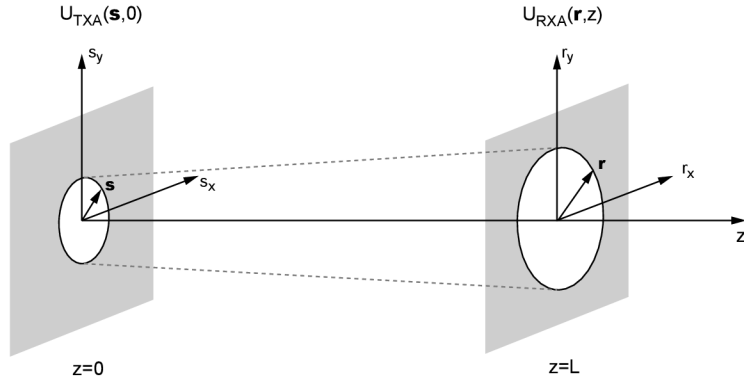


Fig. 4.3: Propagation scheme

the Huygens-Fresnel diffraction integral as follows

$$U_{RXA}(\mathbf{r}, z) = \frac{-ik}{2\pi z} \exp(ikz) \int_{-\infty}^{\infty} \int_{-\infty}^{\infty} U_{TXA}(\mathbf{s}, 0) \exp\left(\frac{ik}{2z} |\mathbf{s} - \mathbf{r}|^2\right) ds^2, \quad (4.6)$$

where  $z$  is the distance between the TXA and RXA plane,  $\mathbf{r}$  is transverse vector at the RXA plane,  $k$  is wave number,  $U_{TXA}(\mathbf{s}, 0)$  is the intensity distribution and  $\mathbf{s}$  is transverse vector at the TXA plane. The scheme of propagation is depicted in Fig. 4.3. In order to simulate the propagation of the FG beam in a vacuum, it is convenient to rewrite Eq. 4.6 as a convolution of the field at the TXA plane with the free-space amplitude spread function [34]

$$U_{RXA}(\mathbf{r}, z) = U_{TXA}(\mathbf{s}, 0) * \left( \frac{-ik}{2\pi z} \exp\left(ikz + \frac{ik}{2z} |\mathbf{s} - \mathbf{r}|^2\right) \right). \quad (4.7)$$

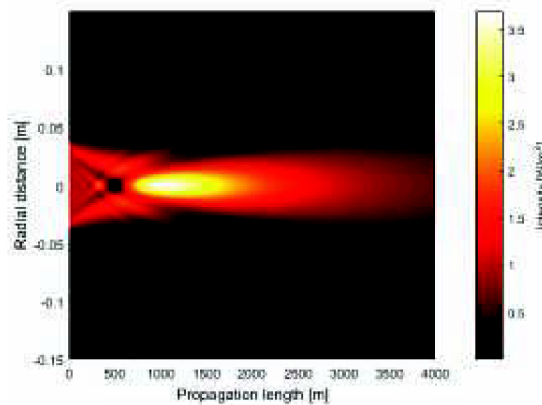


Fig. 4.4: Longitudinal intensity distribution of the FG beam for vacuum propagation

I performed the simulation of Eq. 4.7 to evaluate the intensity distribution across the propagation length. The FG beam half-width was set to  $w_0=40$  mm, flatness

parameter  $N=10$  and wavelength 1550 nm. In Fig. 4.4, it can be seen that the FG beam with high flatness parameter  $N$  acts like a plane wave diffracted on a circular aperture with a radius equal to the FG beam half-width. As the beam is propagated, the transverse optical intensity distribution changes and the middle part of the beam reaches its minimum. From this minimum point, two Fresnel zones are observed exactly at the TXA plane. The Fresnel zone, in our case, can be defined as follows

$$N_{Fresnel} = \frac{w_0^2}{L\lambda}, \quad (4.8)$$

where  $N_{Fresnel}$  is the number of Fresnel zone and  $L$  is the distance between the plane with minimum and the TXA plane. If the FG beam is further propagated, its shape turns into a Gaussian or Airy function.

## 4.1 Flattened Gaussian beam scintillation

The propagation of the FG beam in a turbulent atmosphere has been extensively studied theoretically [9, 10, 11]. Baykal and Eyyuboglu [39] derive equation 4.9 for scintillation index of flattened Gaussian beam defined by equation 4.4 propagated in weak turbulence regime. I used this equation in order to study the optimal size of the beam at TXA.

$$\begin{aligned} \sigma_I^2(0, L) = & 4.884C_n^2 k^{7/6} L \Re \left( \frac{1}{\sum_{n=1}^N \sum_{p=1}^N \frac{(-1)^{n+p-2}}{[1-npa^2L^2+iaL(n+p)]} \binom{N}{n} \binom{N}{p}} \right. \\ & \times \sum_{n=1}^N \sum_{p=1}^N \frac{(-1)^{n+p-2}}{[1-npa^2L^2+iaL(n+p)]} \binom{N}{n} \binom{N}{p} \\ & \times \frac{L^{5/6}}{[1+n^2p^2a^4L^4+a^2L^2(n^2+p^2)]^{5/6}} \\ & \times \int_0^1 \left\{ aL(n+p)(1+npa^2L^2)(1-t)^2 + \right. \\ & \left. + i \left[ 2(1+n^2p^2a^4L^4)(1-t) + a^2L^2(n^2+p^2)(1-t^2) \right] \right\}^{5/6} dt \\ & \left. - \frac{1}{\sum_{n=1}^N \sum_{p=1}^N \frac{(-1)^{n+p-2}}{[1-npa^2L^2+iaL(n+p)]} \binom{N}{n} \binom{N}{p}} \right. \\ & \left. \times a^{5/6} L^{5/6} \frac{3}{8} \sum_{n=1}^N \sum_{p=1}^N \frac{(-1)^{n+p-2} (n+p)^{5/6}}{[1-npa^2L^2+iaL(n+p)]^{11/6}} \binom{N}{n} \binom{N}{p} \right), \quad (4.9) \end{aligned}$$

where  $a = 1/(ka_s^2)$ . If the parameter  $N$  is set to 1 the scintillation index is reduced to the well-known equation 1.25.

## 4.2 Simulation of Flattened Gaussian beam propagation

The numerical simulation was also used to simulate propagation of the FG beam through weak and moderate atmospheric turbulences (Fig. 4.5).

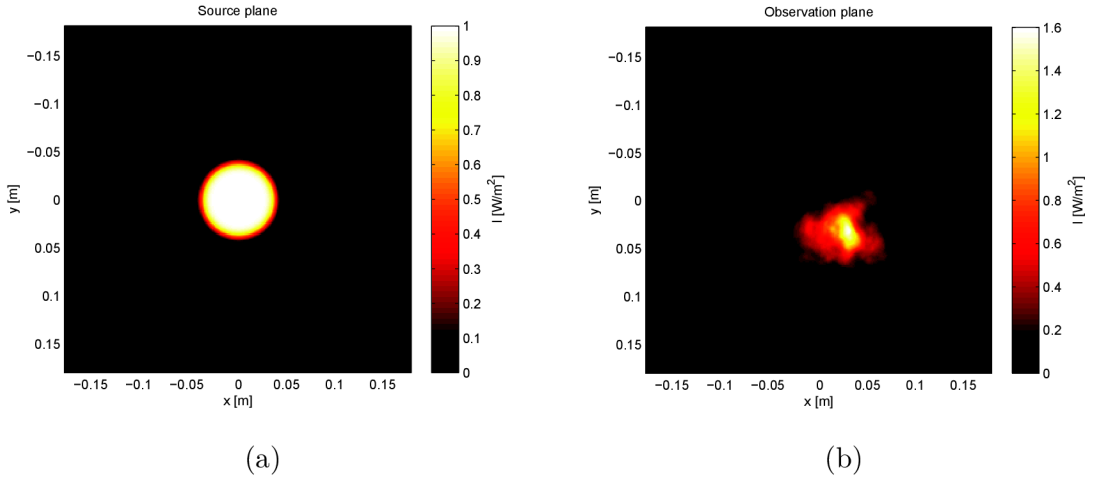


Fig. 4.5: Initial top-hat beam (a) and irradiance resulting from turbulence propagation (b) for  $C_n^2 = 10^{-14} m^{-2/3}$

The initial wavefront is propagated through regions of turbulences which are represented by random phase screens [34]. As a result, a variation in irradiance across the wavefront is observed. The on-axis scintillation index was calculated according to Eq. (1.24) from 500 random runs.

The simulation was carried out for an FG beam with beam radius 10 mm and 40 mm at TXA plane and for flatness parameter  $N = 0$  (Gaussian beam) and  $N = 10$  (FG beam).

From Fig. 4.6, a very interesting fact is notable. The FG beam with radius 10 mm at TXA plane has almost the same on-axis scintillation index as the Gaussian beam. However, this fact is not valid for beam radius 40 mm at TXA plane (Fig. 4.7), where the on-axis scintillation index is lower in comparison with a Gaussian beam for reasonable link lengths. Another interesting fact is that there is a peak of the on-axis scintillation index around 600 m. The peak is located at the place in which two Fresnel zones on TXA plane are observed. The height of the peak is

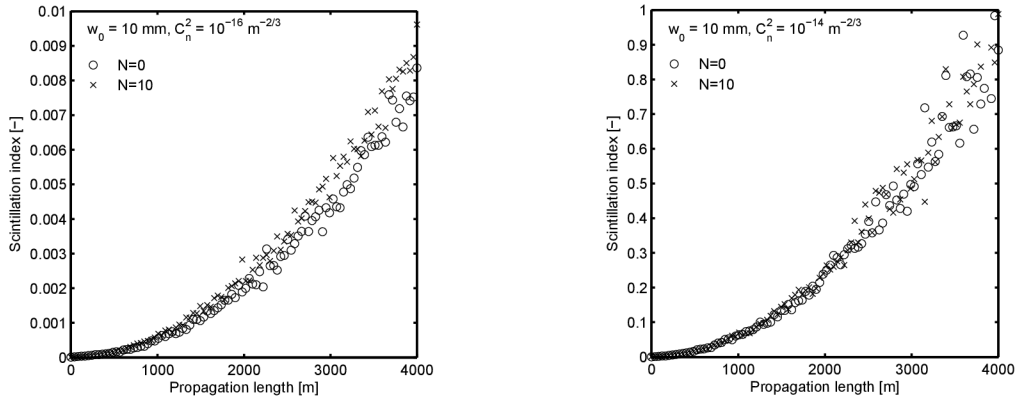


Fig. 4.6: Simulated on-axis scintillation index as a function of propagation length for the FG beam with radius 10 mm at TXA plane

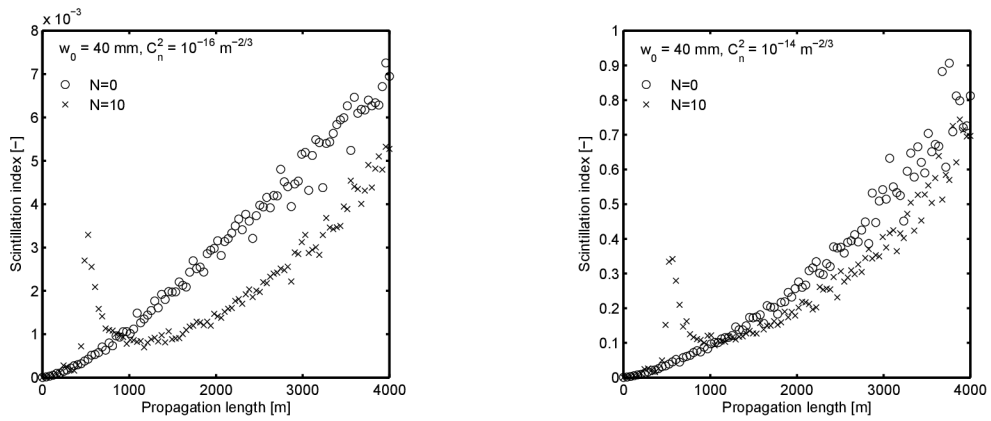


Fig. 4.7: Simulated on-axis scintillation index as a function of propagation length for the FG beam with radius 40 mm at TXA plane

dependent on the order of the flatness parameter of the FG beam. The higher the value of the flatness parameter  $N$  is, the higher the scintillation peak is observed.

Simulation data for FG beam on-axis scintillation as a function of beam radius at TXA plane for two  $N$  parameters are depicted in Fig. 4.8. One can see that the size of the FG beam at the TXA plane plays an important role in the scintillation analysis. Note, that the on-axis scintillation for  $N=0$  is firstly almost constant and then increasing slightly for beam radius above 0.05 m. On the other hand, on-axis scintillation for  $N=10$  is slightly decreasing and then reaches minimum around the radius 0.05 m. If the radius of the beam is further increased the scintillation starts to increase rapidly and then falls to the same value as for  $N=0$ . Therefore, one can estimate the optimal radius of the FG beam, where scintillation for the propagation length 4 km is minimal. The optimal radius for weak and moderate turbulence

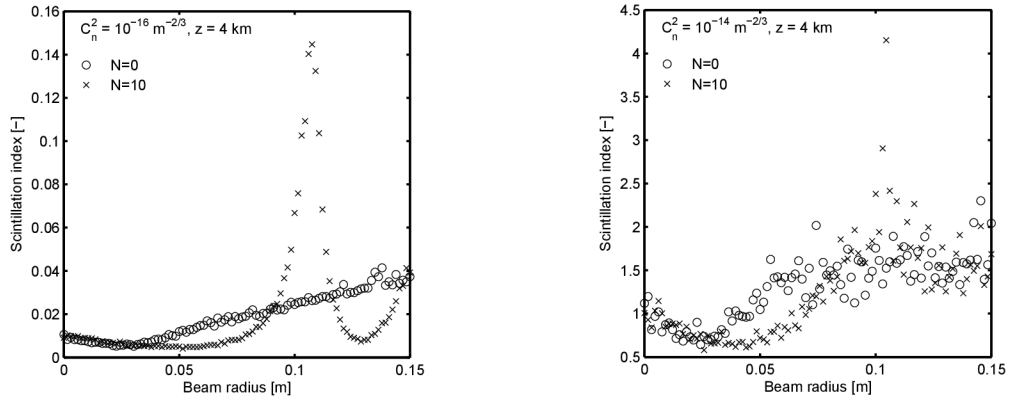


Fig. 4.8: Simulated scintillation index for the FG beam as a function of beam radius at the TXA

regime should be slightly bigger than the radius of the first Fresnel zone, which is also defined by  $\sqrt{L/k}$ .

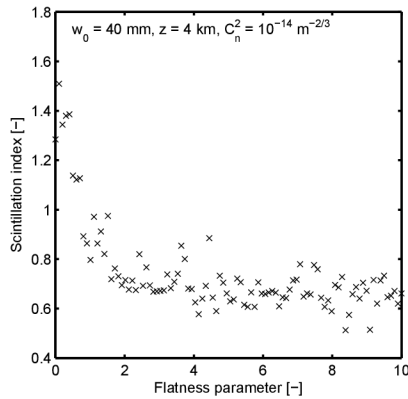


Fig. 4.9: Simulated scintillation index for the FG beam as a function of flatness parameter  $N$

For the sake of maximal reduction of scintillation, I plot the scintillation index as a function of flatness parameter  $N$  (Fig. 4.9). It is obvious that the scintillation index is decreasing with increasing parameter  $N$ . Thus the  $N$  parameter should be high enough.

### 4.3 Aperture averaging

In this section I analysed effect of the aperture averaging on the scintillation for the FG beam with flatness parameter  $N=10$ . The simulation was carried out for circular receiving aperture with radius up to 150 mm. The increasing radius of a receiving aperture, for given beam divergence, wavelength and propagation distance, has noticeable impact on power scintillation reduction, as shown in Fig. 4.10. For the receiving aperture with radius bigger than 50 mm the scintillation peak is diminished completely. As was stated above, the scintillation reduction is quantified by parameter called the aperture averaging factor. The aperture averaging factor as a function of radius of the receiving aperture for three different beam half-widths at the TXA plane is depicted in Fig. 4.11. With increasing radius of the receiving

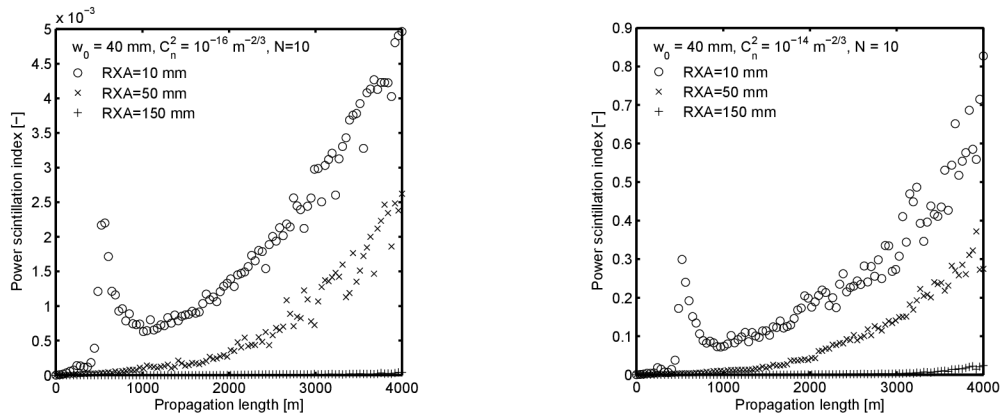


Fig. 4.10: Power scintillation index as a function of propagation length for different radius of receiving aperture

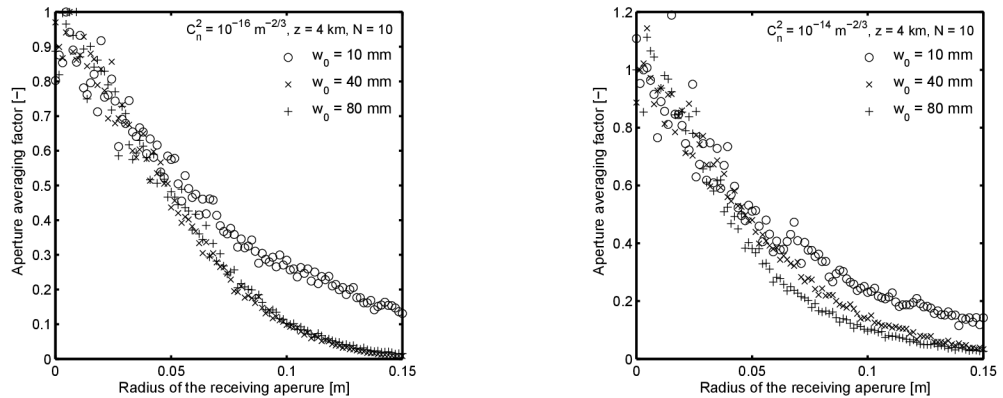


Fig. 4.11: Aperture averaging factor as a function of radius of the receiving aperture

aperture the aperture averaging factor decreases and thus the scintillation of the

received power decreases. It can be seen that value of aperture averaging factor depends on beam half-width at the TXA and beam divergence. The scintillation of the power is averaged out more for the FG beam with half-width 40 mm in comparison with half-width 10 mm. In case of using receiving aperture with radius above 0.15 m, aperture averaging factor is almost the same for FG beam with half-width 40 mm and 80 mm. The previous statements are valid for weak and moderate turbulence regime.

## 4.4 Probability of fade

Reliability of the optical communication link could be assessed by probability of fades models [12, 24]. Fade probability is calculated only for intensity fluctuations caused by atmospheric turbulence. The presented results are valid for point receiver. Because the scintillation was simulated only for weak atmospheric turbulence, the lognormal model was used.

The lognormal model is given by [12]

$$P_I(I) = \frac{1}{I \sigma_I(\mathbf{r}, L) \sqrt{2}} \exp \left\{ -\frac{\ln \left( \frac{I}{\langle I(\mathbf{r}, L) \rangle} \right) + 0.5 \sigma_I^2(\mathbf{r}, L)}{2 \sigma_I^2(\mathbf{r}, L)} \right\} \quad (4.10)$$

where  $\sigma_I^2(\mathbf{r}, L)$  is the scintillation index and  $\langle I(\mathbf{r}, L) \rangle$  is the mean irradiance. Probability of fade is then determined as follows [24]

$$Pr(I \leq I_T) = 0.5 \left\{ 1 + \operatorname{erf} \left[ \frac{0.5 \sigma_I^2(\mathbf{r}, L) - 0.23 F_T}{\sqrt{2} \sigma_I(\mathbf{r}, L)} \right] \right\}, \quad (4.11)$$

where  $\operatorname{erf}(x)$  is the error function.  $F_T$  is the fade threshold parameter defined as

$$F_T = 10 \log \left( \frac{\langle I(0, L) \rangle}{I_T} \right), \quad (4.12)$$

where  $I_T$  is the threshold level of irradiance and  $\langle I(0, L) \rangle$  is on-axis mean irradiance at distance L. Expected number of fades per second is defined as [12]

$$\langle n(I_T) \rangle = \nu_0 \exp \left[ -\frac{(0.5 \sigma_I^2 - 0.23 F_T)^2}{2 \sigma_I^2} \right], \quad (4.13)$$

where  $\nu_0$  is quasi-frequency. According to [22] the quasi-frequency is taken as 550 Hz.



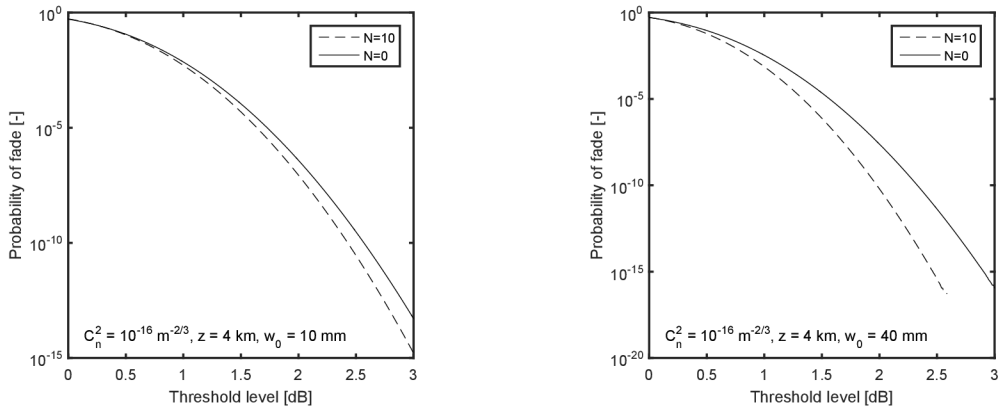


Fig. 4.12: Probability of fade as a function of threshold level

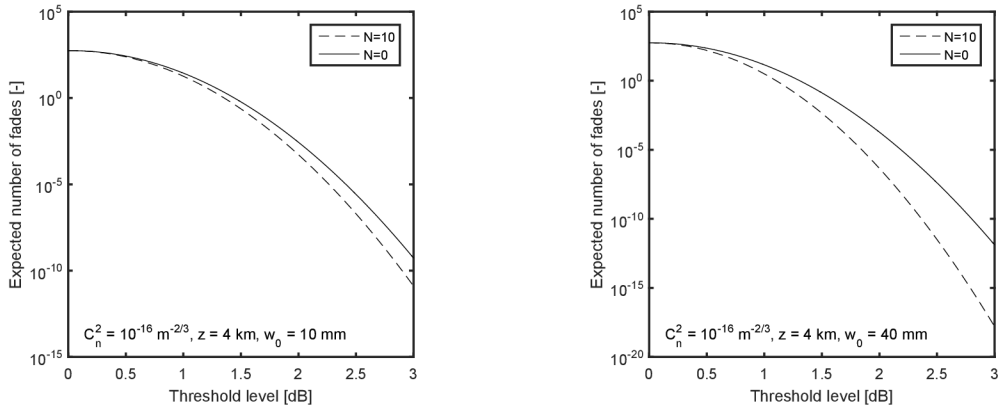


Fig. 4.13: Expected number of fades as a function of threshold level

In this section the probability of fade and expected number of fades per second for Flattened Gaussian beam with radius 10 mm and 40 mm was estimated. The level of scintillation was determined from the simulated results which were presented in Section 4.2 (Fig. 4.6 , Fig. 4.7).

The probability of fades for FG beam half-width  $w_0 = 10$  mm is depicted in Fig. 4.12. There is no significant advantage in probability of fades between FG beam with parameter  $N = 0$  and  $N = 10$ . On the other hand when the beam radius is set to  $w_0 = 40$  mm, one can see more significant difference in probability of fades. The similar results are obtained for expected number of fades (Fig. 4.13). As a conclusion it is possible to say, that FG beam brings advantage over the Gaussian beam, however the parameters of the FG beam has to be set carefully.

## 4.5 Summary

In this chapter, propagation of the FG beam through weak and moderate turbulent atmosphere was simulated. The simulation was based on the split-step beam propagation method. It was shown that propagation of the FG beam with a high flatness parameter can be analysed as a diffraction of an incident plane wave on a circular aperture with a radius equal to the radius of the FG beam at the TXA plane. Using this approach, I was able to determine optimal parameters in terms of reducing on-axis scintillation index. For reducing on-axis scintillation, the optimal radius of the FG beam at the TXA plane for a particular propagation length has to be set. As a result of the simulation, I also found that the receiver has to be placed in the far field ( $N_{\text{Fresnel}} \ll 1$ ) and the flatness parameter has to be high enough. The simulations also showed that the aperture averaging effect has essential impact on scintillation reduction. Therefore, the signal-to-noise ratio at the receiver increases and bit error rate decreases. It was found that the scintillations were averaged out maximally for bigger half-width of the beam at TXA as well as for bigger radius of the receiving aperture. However, the optimal radius of the receiving aperture depends on particular system demands. From the probability of fades analysis, it is clear that there is an advantage over the Gaussian beam for FG beams with half-width  $w_0 = 40$  mm.

## 5 BEAM SHAPER FOR FREE SPACE OPTICAL COMMUNICATION TRANSMITTER

After the results presented in the previous chapter, it can be stated that the optimal distribution of optical intensity within a laser beam at the TXA is uniform. However, coherent optical sources like lasers and laser diodes emit a light whose intensity profile can be approximated by a Gaussian function. So the intensity distribution has to be transformed into a uniform function. There exist several transformation methods to obtain the uniform optical intensity distribution at the output plane of beam shaping optics. Some of the methods are appropriate for laser beams with a high degree of coherence, and other methods are applicable to non coherent optical sources. The transformation techniques can also be divided according to the measure of conversion losses. One group of shaping techniques is known as field mapping. It is suitable for coherent optical sources [42]. The other methods, which are cost effective and also applicable for non coherent sources, are beam integrators [42].

One of the basic techniques for laser beam shaping is a method which uses a lenslet array as a shaping element. The method belongs to the group of beam integrators. The basic concept of the usage of the lenslet array is in dividing the input Gaussian beam into sub-beams. The diameter of particular sub-beams depends on the lenslet structure. Afterwards, I fold particular sub-beams by an optical lens, which is called a Fourier lens [42]. The sub-beams are visible from the experimentally measured intensity profile in Fig. 5.1.

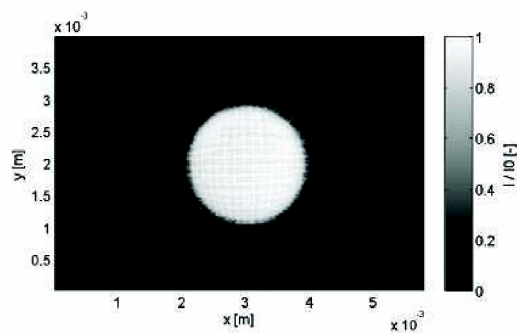


Fig. 5.1: Experimentally measured intensity profile of FG beam - lenslet array shaping technique [43]

Diffractive diffusers, also so-called homogenizers, are the next option how to get a desired distribution of the optical intensity at a chosen plane [44]. These diffusers belong to the group of field mappers [42]. This type of diffractive optics is typically

used when the monochromatic laser beam is applied. Among other advantages, we take into account the fact that they are not sensitive to alignment and do not affect the polarization of the input beam. The most common shapes of diffusers are square, round, rectangular and elliptical. The edges of the diffuser beam are generally steep. The disadvantage of this method is that the intensity profile of the output beam is speckled due to the pseudo-random energy diffusion (Fig. 5.2).

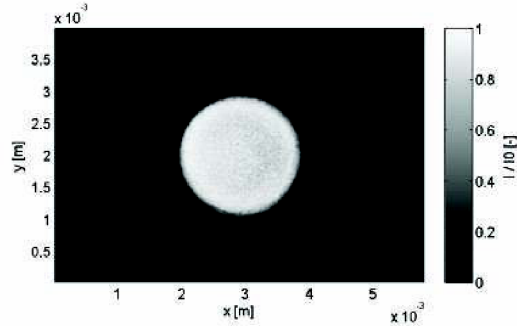


Fig. 5.2: Experimentally measured intensity profile of FG beam - diffractive diffuser shaping technique [43]

## 5.1 Refraction beam shaper

A couple of plano-aspheric lenses seem to be promising beam shaping method [38, 45, 46, 47, 48] for FSO communications. The advantage of this beam shaper is low loss in optical power in comparison with previously mentioned techniques. The Keplerian configuration [38] consists of two plano-convex lenses, the first aspheric surface reshapes the intensity profile and the second one corrects the beam phase [49]. The design can be performed by a geometric design method which is based on the numerical calculation of two plano-aspheric lenses. However, other techniques might be used as well e.g. the functional differential equation based design approach where the rotational symmetric lens profiles are described by two-point Taylor polynomials [50]. I have performed the design of such a beam shaper. The design was verified in optical design system ZEMAX [51].

As an input beam I supposed collimated Gaussian beam with irradiance distribution given with relation

$$I_{in}(x) = \frac{2}{\pi w_0^2} \cdot e^{-2\left(\frac{x}{w_0}\right)^2}. \quad (5.1)$$

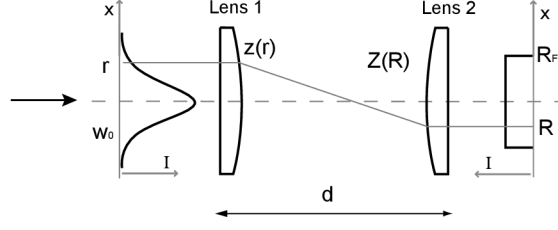


Fig. 5.3: Scheme of refraction beam shaper based on Keplerian design [52].  $z(r)$  - sagita of the first aspherical surface,  $Z(R)$  - sagita of the second aspherical surface,  $r$  - distance from the optical axis of the input ray,  $R$  - distance from the optical axis of the ray in the output plane,  $w_0$  - input beam radius,  $R_{FL}$  - output beam half radius,  $d$  - distance between two aspherical lenses

The function of the output beam shape is optional and depends on the usage of the shaper. I used flattened Lorentzian function [53]

$$I_{out}(x) = \left( \frac{1}{\pi R_{FL}^2} \right) \left[ \frac{1}{\left[ 1 + \left( \frac{x}{R_{FL}} \right)^q \right]^{\frac{2}{q}}} \right], \quad (5.2)$$

where  $R_{FL}$  is the beam half width.

According to Kreuzer patent [54] the first condition which has to be fulfilled is conservation of the energy (5.3), where energy of the incident beam is equal to energy of the output beam.

$$\int_0^r I_{in}(x) x dx = \int_0^R I_{out}(x) x dx, \quad (5.3)$$

where  $I_{in}$  is intensity of input beam and  $I_{out}$  is intensity of output beam. I assume the ideal lens elements without the reflection and absorption losses. After symbolical integration of left and right side of the equation (5.3) the mapping functions for the first and the second aspheric lens may be obtained.

$$R(r) = \frac{R_{FL}}{\sqrt[q]{-1 + \left[ 1 - e^{-2\left(\frac{r}{w_0}\right)^2} \right]^{\frac{q}{-2}}}} \quad (5.4)$$

$$r(R) = w_0 \sqrt{-0.5 \left[ 1 - \left[ 1 + \left( \frac{R_{FL}}{R} \right)^q \right]^{\frac{-2}{q}} \right]} \quad (5.5)$$

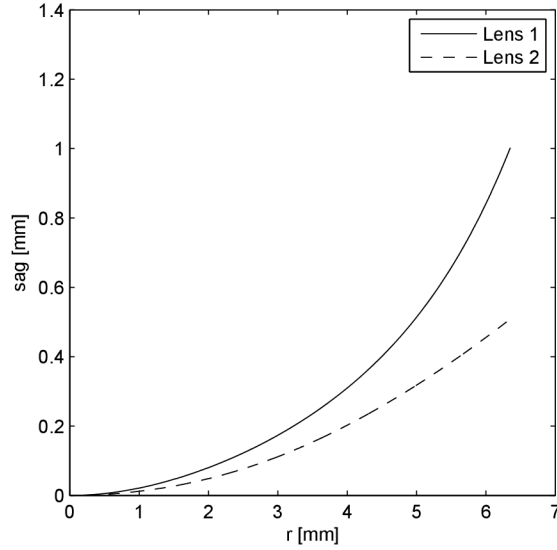


Fig. 5.4: Sag of the lenses

The profile of the aspheric lenses  $z(r)$ ,  $Z(R)$  are determined in terms of  $n$ ,  $d$ ,  $r$  and  $R$  as follows [54]

$$z(r) = \int_0^r \left[ (n^2 - 1) + \left[ \frac{(n-1)d}{(R-r)} \right]^2 \right]^{\frac{-1}{2}} dr, \quad (5.6)$$

$$Z(R) = \int_0^R \left[ (n^2 - 1) + \left[ \frac{(n-1)d}{(R-r)} \right]^2 \right]^{\frac{-1}{2}} dR, \quad (5.7)$$

where  $n$  is refractive index of lens material,  $d$  is separation of the two lenses,  $r$  and  $R$  is the radius of the first and the second element from optical axis.

The parameters of our design are as follows: wavelength 1550 nm, material of the lenses CAF2 with refractive index  $n = 1.433489$ , separation distance between lenses  $d$  was set to 150 mm, Gaussian beam waist  $w_0 = 2.6$  mm, beam width of flattened output beam  $R_{FL} = 3$  mm for  $q$  parameter 6. After the numerical integration of the equations (5.6) and (5.7) I got profile of the both aspheric surfaces which are depicted in Fig. 5.4.

Because optical design software like ZEMAX needs parameters of the lens in terms of polynomial equation (5.8), I had to fit the equation to the obtained curves from Fig. 5.4.

$$z(r) = \frac{\frac{r^2}{R}}{1 + \sqrt{1 - (1+k)\frac{r^2}{R^2}}} + A_1 r^4 + A_2 r^6 + A_3 r^8 + A_4 r^{10} + A_5 r^{12}. \quad (5.8)$$

The fitting was performed by Weighted Least Squares method. The resulting parameters are listed in Tab. 6.2.

Tab. 5.1: Parameters of the Lenses

	Lens 1 [mm]	Lens 2 [mm]
Vertex radius $R$	23.2365	42.4596
Conic constant $k$	-1.0679	-1.0407
$A_1$	$-4.9277x10^{-4}$	$9.0003x10^{-5}$
$A_2$	$3.5893x10^{-5}$	$-1.8609x10^{-6}$
$A_3$	$-1.1531x10^{-6}$	$-5.4168x10^{-8}$
$A_4$	$2.1961x10^{-8}$	$2.4074x10^{-9}$
$A_5$	$-1.65038x10^{-10}$	$2.4234x10^{-11}$

Designed beam shaper was verified in ZEMAX software. The resulting optical layout is depicted in Fig. 5.5. The refractive beam shaper is not achromatic. If we want to change the wavelength of the incident light, we have to change the separation distance between two lenses [46].

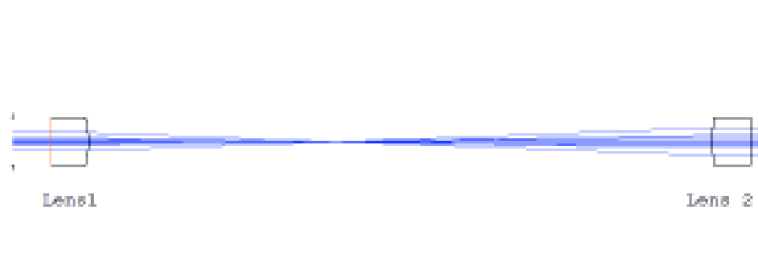
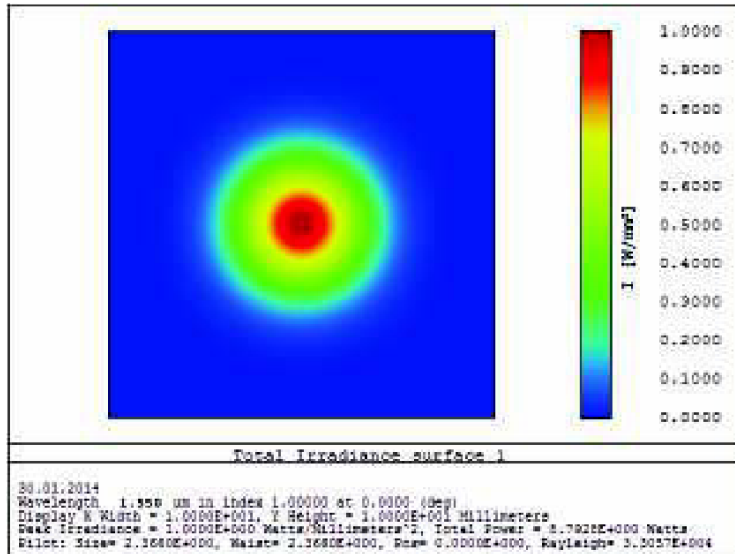
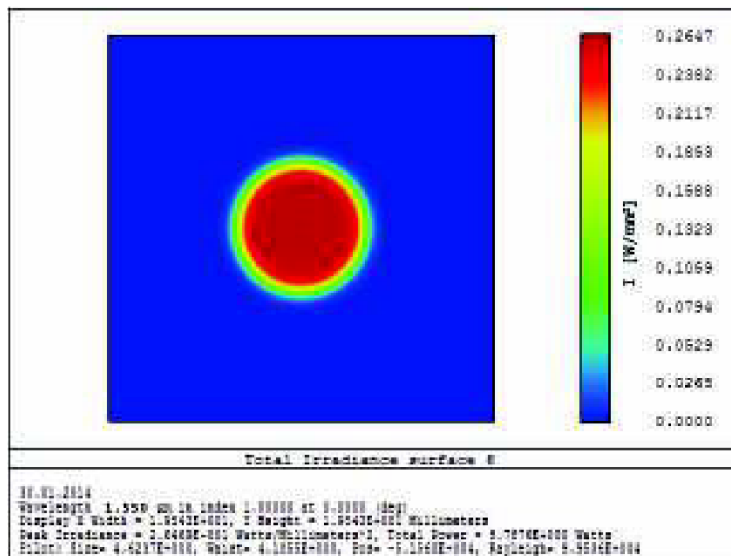


Fig. 5.5: Layout of the beam shaper



(a) Input Gaussian beam



(b) Output top-hat beam

Fig. 5.6: Zemax simulation results

The output FG beam (at the TXA plane) in Fig.5.6b has diameter 3 mm, however beam radius at TXA plays very important role in scintillation analysis. Assume that FSO link has length 4000 m, wavelength 1550 nm and refraction structure parameter is set to  $10^{-14} \text{ m}^{-2/3}$ . The optimal size of the beam at the TXA plane to achieve minimal scintillation can be estimated from Fig. 5.7a, where a function of top-hat beam scintillation index (from equation 4.9) on beam radius at TXA is depicted. From enlarged figure section the optimal radius of the beam is around 40 mm, where the scintillation index reaches minimum. The beam at the output of the refraction



beam shaper has radius 3 mm which means that using of beam expander behind the shaper to achieve optimal beam size is needed. In Fig. 5.7b the scintillation indexes for a Gaussian beam and FG beam is compared. For this particular FG beam radius the obtained result reveals that the scintillation index become larger for link distance lower than 2000 m. Situation changes for greater distances, where the scintillation index is approximately 30 % lower than the Gaussian beam scintillation index. I obtained very similar results by simulating the system in Chapter 4.

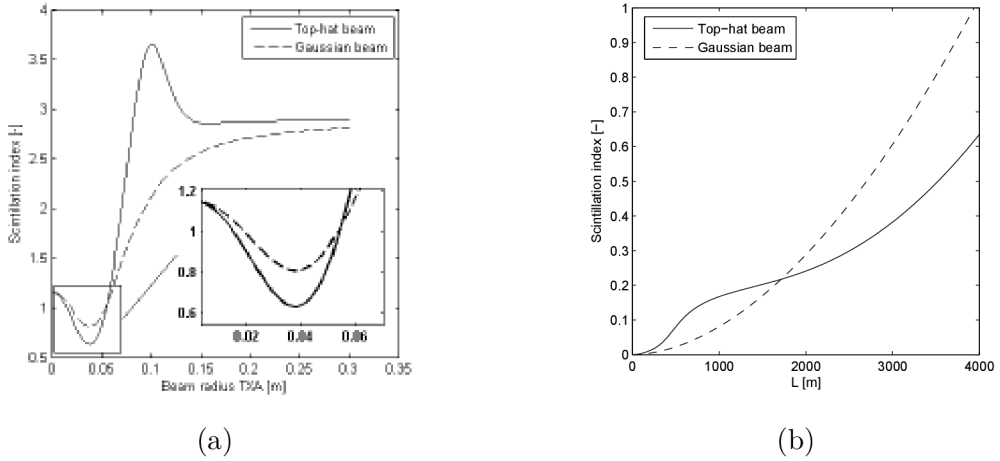


Fig. 5.7: The scintillation index at RXA for both beams as a function of beam radius at TXA (a) and the scintillation index for both beams with radius of 40 mm at RXA as a function of propagation length (b).

As was stated in [24] this slight decrease of scintillation index leads to significant improvement of a fade statistic.

## 5.2 Optical fiber as a beam shaper

In previous sections I deal with the case where the optical intensity has uniform distribution at the TXA plane. If the coherent beam with uniform intensity distribution is propagated then the intensity distribution at the RXA plane becomes Gaussian due to diffraction. The intensity distribution depends on FG beam halfwidth at the TXA plane, wavelength of the light source and propagation length.

In this section I am dealing with problem how to achieve uniform distribution of the optical intensity at the receiver plane. One of the possibility is using of optical fiber as a transmitting fiber. The intensity of light emanating from three different fibers was studied. For the comparison the single mode fiber is also included. Thereafter I analysed multi-mode gradient index fiber and multimode step index fiber with

Tab. 5.2: Parameters of the optical fibers

	Fiber 1	Fiber 2	Fiber 3
Type	Single - mode	Multi - mode gradient index	Multi - mode step index
Core diameter [ $\mu\text{m}$ ]	10	62.5	1000
Core material	Fused silica	Fused silica	Fused silica
Numerical aperture (NA)	0.130	0.275	0.220
Attenuation @ 1550 nm [dB/km]	0.18	0.6	400
Wavelength range [nm]	980 – 1550	800 – 1600	350 – 2500

large core diameter. The technical parameters of the fibers are summarized in Tab. 5.2.

In Fig. 5.8 is depicted intensity distribution emanating from the single mode fiber. Only one fundamental mode is propagated and intensity distribution has Gaussian character with peak at the center. The optical intensity distribution of multi-mode gradient index fiber is depicted in Fig. 5.9. It is clear that there are dozens of modes propagated inside the fiber. In order to excite as many modes as possible the fiber was scrambled with mode scrambler. The mode scrambler has to be used because fiber was only 2 meters long and single mode laser was used as a light source.

The third fiber is multi mode step index fiber with large core diameter. The diameter of the core is 1000  $\mu\text{m}$ . A large core fibers are usually used as a spectrometer probes. Due to high attenuation of the fibers, they are used for short distance

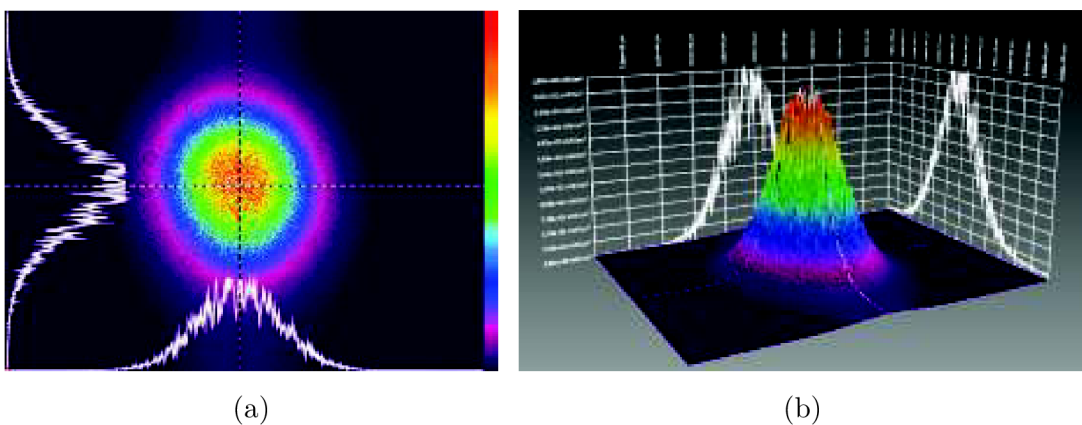


Fig. 5.8: Optical intensity distribution of the single mode fiber

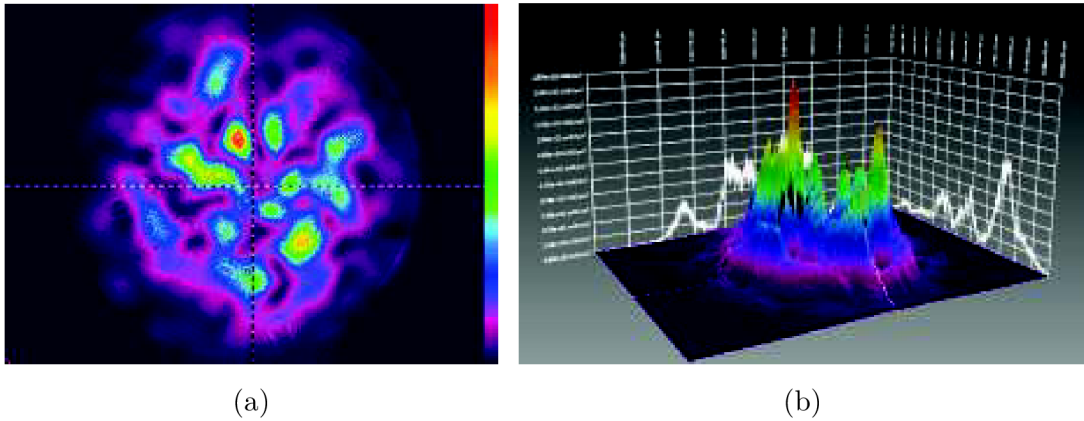


Fig. 5.9: Optical intensity distribution of the multimode fiber

communication and car communication inside a car. Even the length of the fiber was only 2 meters all modes were excited without any mode scrambler. When the intensity distribution was depicted, very interesting fact was observed. The intensity distribution is created with million of modes and the envelope of this modes looks like top-hat beam (see Fig. 5.10). The short fiber can be used in the transmitter as a shaping element. As a result one get more uniform distribution of the optical intensity at the RXA plane.

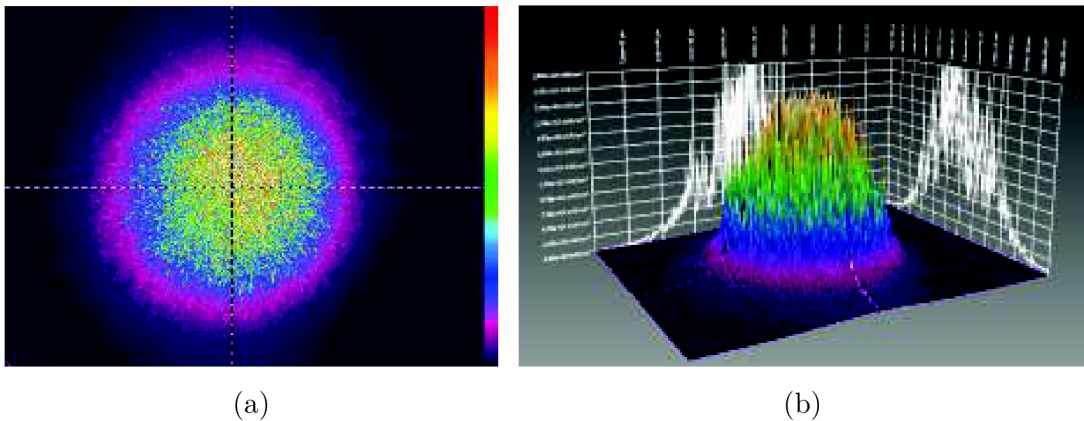


Fig. 5.10: Optical intensity distribution of the plastic fiber

Another feature of the large core fiber is that it acts like a phase diffuser and emanating light became partially coherent. It was shown in many publications that partially coherent beam is less affected by atmospheric turbulences [55, 56].

## 5.3 Summary

This chapter introduced the beam shaping techniques, which is suitable for converting Gaussian beam optical intensity distribution to Flattened Gaussian beam optical intensity distribution. Within this chapter the pros and cons of the shaping techniques were mentioned. I designed the refractive beam shaper which consists of two plano convex aspheric lenses. Thereafter, the design was verified with the optical and illumination design software ZEMAX. The output FG beam has good quality. However, the price of the beam shaper would be very high because the aspheric lenses have to be custom made. Because the beam shaper should be implemented inside a free space optics terminal, the price should be very low. The next possible option is using a plastic optical fiber with large core diameter as a beam shaping element. For that case I have examined the output optical intensity distribution of three different optical fibers, among which single mode fiber, multimode fiber and plastic optical fiber. The plastic optical fiber exhibits an appropriate output optical intensity distribution. The distribution is created by thousand of modes whose envelope is similar to the FG beam. Because the light emanating from the plastic optical fiber is partially coherent, the scintillation level could be even more reduced.

## 6 FULLY PHOTONIC LINK

The perspective technology, which can increase resistance of the FSO link to atmospheric effects, is concept of the fully photonic FSO terminals [57, 58]. The outdoor unit of the fully photonic FSO terminal consists of only passive optical components. Active components like lasers, photodiodes, fiber amplifiers, fiber couplers and supply parts are placed in the indoor unit, which does not suffer on weather changes.

### 6.1 Transmitter with large core optical fiber

The fully photonic concept of the transmitter offers many possibilities in improving optical wireless communication. The transmitted beam may include multiple optical channels obtained by using the WDM technique.

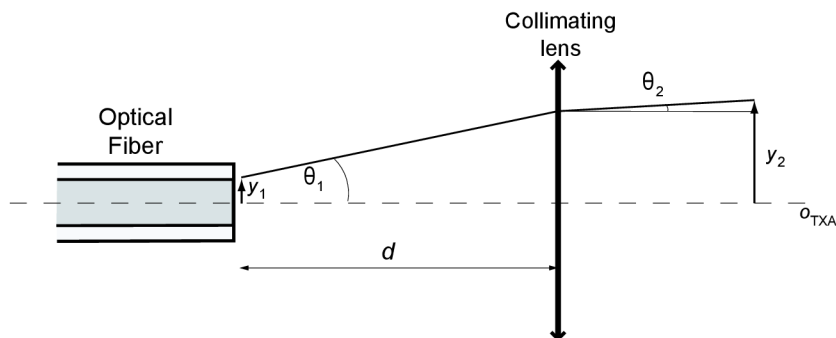


Fig. 6.1: Design of the transmitter

The purpose of the Fully Photonic Transmitter (FPT) is to create a transmitted optical beam by an optical fiber irradiating the transmitting lens (achromatic doublet lens). If the multimode fiber (plastic or glass) is used as a final fiber, the optical intensity distribution in the transmitted beam will generate a so-called "top-hat" beam [58], which is more resistant to the negative effects of atmospheric turbulence in comparison with the standard Gaussian beam.

An optical fiber AVANTES FC-IR1000-2-FC/PC with core diameter 1 mm and numerical aperture  $NA = 0.22$  was used as the transmitting fiber in our model. The attenuation of the fiber 2 meters long is approximately 0.8 dB. For modeling the FPT function, it is sufficient to apply the matrix optics methods.

The translation matrix describing the free space propagation of the optical ray through the distance  $d$  between the output aperture of the optical fiber and principal plane of the transmitting optical system (achromatic doublet lens) is expressed as

follows [59]

$$\mathbf{M}_T = \begin{bmatrix} 1 & d \\ 0 & 1 \end{bmatrix}. \quad (6.1)$$

The transmitting optical system (Fig. 6.1) is modeled as a thin ideal lens with focal length  $f_{\text{TXA}}$ . Propagation of the optical ray through this lens is described by the refraction matrix  $\mathbf{M}_R$

$$\mathbf{M}_R = \begin{bmatrix} 1 & 0 \\ -\frac{1}{f_{\text{TXA}}} & 1 \end{bmatrix}. \quad (6.2)$$

The resulting transfer matrix, between the output aperture of the optical fiber and output plane of the achromatic doublet lens, could be expressed by transfer matrix (6.1) and refraction matrix (6.2). The output ray parameters at the output of the collimating lens (transmitting aperture) are given by (Fig. 6.1)

$$\begin{bmatrix} y_2 \\ \theta_2 \end{bmatrix} = \mathbf{M}_R \mathbf{M}_T \begin{bmatrix} y_1 \\ \theta_1 \end{bmatrix}. \quad (6.3)$$

Therefore, parameters of the transmitted ray ( $y_j$  and  $\theta_j$ ,  $j = 1, 2$ ) can characterize the parameters of the transmitted beam: distance of the ray from the optical axis  $y_j$  corresponds to beam radius, and angle between the ray and optical axis  $\theta_j$  agree with beam divergence. After substituting matrices (6.1) and (6.2) into equation (6.3) we get the relations for beam radius  $y_2$  and beam divergence  $\theta_2$

$$y_2 = y_1 + d\theta_1, \quad (6.4)$$

$$\theta_2 = -\frac{y_1}{f_{\text{TXA}}} + \theta_1 \left( \frac{d}{f_{\text{TXA}}} - 1 \right). \quad (6.5)$$

An achromatic doublet lens THORLABS AC508-075-C with focal length  $f_{\text{TXA}} = 75$  mm and diameter  $D_{\text{TXA}} = 50$  mm, which is suitable for the transmitting optical system, was chosen as the collimating lens from commercially available lenses. The lens is coated for C-band 1050 - 1700 nm. After substituting the angle  $\theta_1$ , which is given by the numerical aperture of the transmitting fiber and core radius of the transmitting fiber  $y_1$ , into (6.4) and (6.5) we get the divergence of the transmitted optical beam 1 mrad.

From the energetic point of view it is need to check whether the NA of the fiber is lower than NA of the transmitting lens. Numerical aperture of the transmitting lens can be calculated as follows

$$NA_{\text{lens}} \approx \frac{1}{2f\#}, \quad (6.6)$$



## 6.2 Fully photonic receiver

The most challenging part of the fully photonic terminal is to design the fully photonic receiver (FPR). The purpose of the FPR is to focus the received optical power to the core of a receiving optical fiber with diameter of only few micrometers. In order to estimate the coupling efficiency in laboratory condition it is needed to design the testbed (Fig. 6.13). In the section, I numerically design the testbed for measuring the coupling efficiency of the FPR. The testbed consists of the Testing Transmitter (TT) and FPR under test. The numerical model is based on transformation of the Gaussian beam through optical system described by ray transfer matrix. The step by step design process is added and finally the coupling efficiency of the FPR is theoretically estimated for single-mode fiber.

The FPR concept is shown in Fig. 6.13. The optical wave captured by the Cassegrain telescope is collimated using an aspheric collimating lens and guided to the GRIN lens, which is connected to an receiving optical fiber at its output. The outgoing collimated optical wave from the aspherical lens is ensured by tuning the focal length  $f_{tel}$  of the Cassegrain telescope (Fig. 6.4).

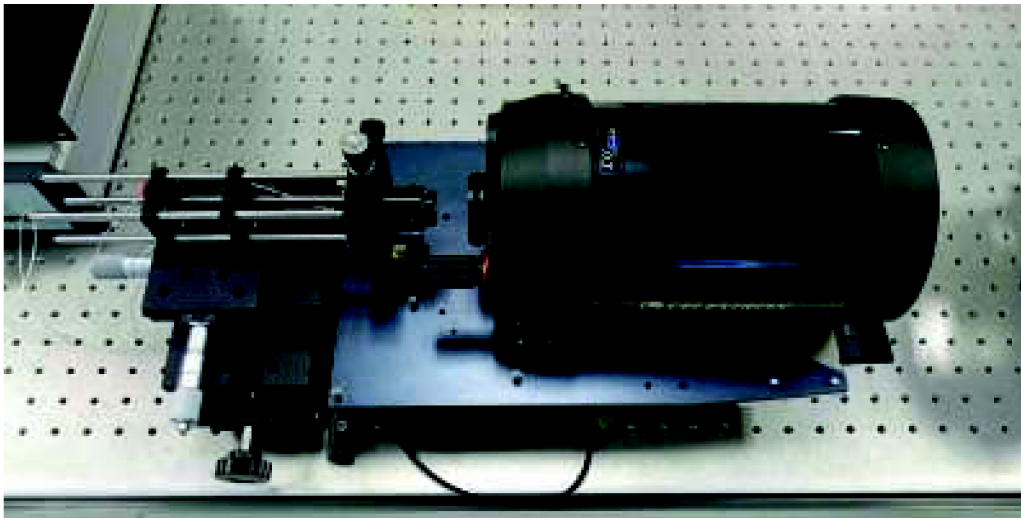


Fig. 6.4: Prototype of the FPR.

The critical optical system requirements include diameter of the receiver aperture, field of view of the receiver, operating wavelength, f-number of the aspheric collimating lens, core diameter and acceptance angle of the receiving fibre [17, 60, 58]. This section presents considerations and requirements on the FPR design used for optical beam coupling from free-space to an optical fiber at  $\lambda = 1550$  nm.

The FPR model was created using matrix optics methods, which assumes beam propagation in Gaussian paraxial space (rays are propagated near the optical axis with a small deviation from the direction of the axis).



In order to get the whole ray transfer matrix of the system, the Cassegrain telescope is modelled as a thin positive lens, whose refraction matrix

$$\mathbf{M}_{1'} = \begin{bmatrix} 1 & 0 \\ -1/f_{tel} & 1 \end{bmatrix} \quad (6.7)$$

is situated at the principal plane of the receiving lens. The ray transfer between the principal plane of the receiving lens and the principal plane of the aspherical lens is expressed by the translation matrix

$$\mathbf{M}_{1'2'} = \begin{bmatrix} 1 & f_{tel} + f_A \\ 0 & 1 \end{bmatrix}. \quad (6.8)$$

For the refraction matrix of the aspherical lens situated at the principal plane of the lens, it is possible to write

$$\mathbf{M}_{2'3'} = \begin{bmatrix} 1 & 0 \\ -1/f_A & 1 \end{bmatrix}. \quad (6.9)$$

The distance between the principal plane of the aspherical lens and input aperture of the GRIN element is given by the translation matrix

$$\mathbf{M}_{3'4'} = \begin{bmatrix} 1 & d_3 \\ 0 & 1 \end{bmatrix}. \quad (6.10)$$

The GRIN lens refraction matrix can be expressed as follows [61]

$$\mathbf{M}_{5'6'} = \begin{bmatrix} \cos(g l_g) & \frac{1}{g n_g} \sin(g l_g) \\ g n_g \sin(g l_g) & \cos(g l_g) \end{bmatrix}, \quad (6.11)$$

where  $g$  is gradient constant,  $l_g$  is length and  $n_g$  is refraction index at the center of the GRIN lens. For the maximum coupling efficiency the fiber is placed at the working distance of the GRIN lens. Working distance  $d_w$  is represented by the following translation matrix

$$\mathbf{M}_{7'8'} = \begin{bmatrix} 1 & d_w \\ 0 & 1 \end{bmatrix}. \quad (6.12)$$

The ray transfer matrix of the complete receiving optical system  $\mathbf{M}_{\mathbf{R}}$  is given by multiplying all the elementary matrices in the correct order

$$\mathbf{M}_{\mathbf{R}} = \mathbf{M}_{7'8'} \cdot \mathbf{M}_{5'6'} \cdot \mathbf{M}_{3'4'} \cdot \mathbf{M}_{2'3'} \cdot \mathbf{M}_{1'2'} \cdot \mathbf{M}_{1'}. \quad (6.13)$$

After rearrangement we obtain

$$\mathbf{M}_{\mathbf{R}} = \begin{bmatrix} A_R & B_R \\ C_R & D_R \end{bmatrix}, \quad (6.14)$$

where elements of the matrix are

$$A_R = -\frac{f_A (\cos(gl_g)) - d_w g n_g \sin(gl_g)}{f_{tel}}, \quad (6.15)$$

$$B_R = (\cos(gl_g) - d_w g n_g \sin(gl_g)) \\ \times \left[ f_A - \frac{f_{tel}(d_3 - f_A)}{f_A} \right] \frac{f_{tel} \left( \frac{\sin(gl_g)}{g} + n_g d_w \cos(gl_g) \right)}{f_A n_g}, \quad (6.16)$$

$$C_R = \frac{f_A g n_g \sin(gl_g)}{f_{tel}}, \quad (6.17)$$

$$D_R = -\frac{f_{tel} \cos(gl_g)}{f_A} - g n_g \sin(gl_g) \left[ f_A - \frac{f_{tel}(d_3 - f_A)}{f_A} \right]. \quad (6.18)$$

From the obtained relations, it is possible to calculate crucial parameters and make a design of the FPR.

### 6.3 Estimation of received power by the Schmidt Cassegrain telescope

After propagation through the free space channel, the beam is received by the Schmidt-Cassegrain telescope 6.5 (primary mirror diameter  $D_{1,RXA} = 125$  mm, secondary mirror diameter  $D_{2,RXA} = 50$  mm). Due to construction of the Schmidt-Cassegrain telescope, 16 % of the area of the receiving aperture is obscured by secondary mirror. The amount of the received power by telescope can be calculated as follows

$$P_{RXA} = \left[ \int_0^{\frac{D_{1,RXA}}{2}} I_0 \exp \left[ -2 \left( \frac{r}{w_{RXA}} \right)^2 \right] 2\pi r dr \right] - I_0 \pi \frac{D_{2,RXA}^2}{4}, \quad (6.19)$$

where  $w_{RXA}$  is half beam width at the plane of the receiving aperture;  $r$  is perpendicular distance from the optical axis of the receiver and  $I_0$  is optical intensity on the optical axis at the plane of the receiving aperture. After evaluation of the integral 6.19 we get the relation for received power

$$P_{RXA} = \frac{1}{2} I_0 \pi \left\{ w_{RXA}^2 \left[ 1 - \exp \left( -2 \left( \frac{D_{1,RXA}}{2 w_{RXA}} \right)^2 \right) \right] - \frac{D_{RXA}^2}{2} \right\}. \quad (6.20)$$

In Fig. 6.5 is depicted the dependency of measure of the received power on the half beam width  $w_{RXA}$  at the receiver plane normalized by receiver aperture radius

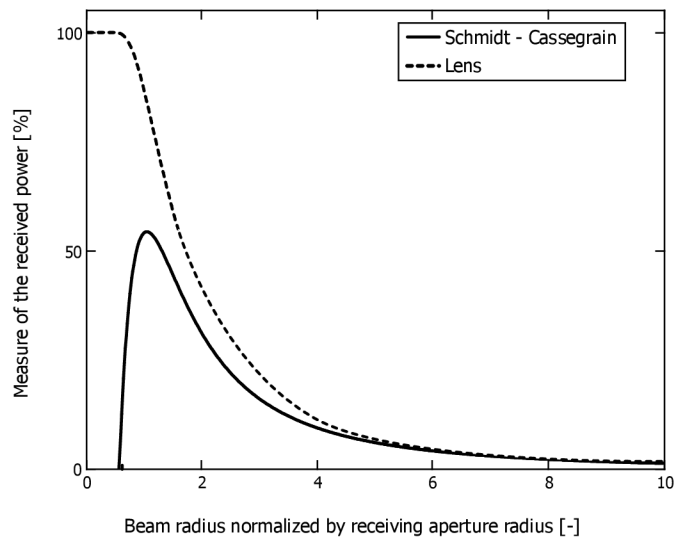


Fig. 6.5: Measure of the received power as a function of half beam width at the receiver plane normalized by receiver aperture radius.

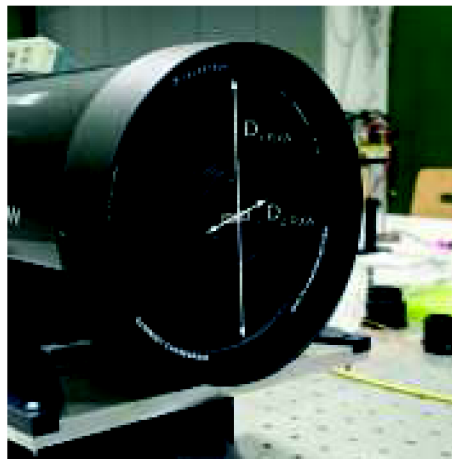


Fig. 6.6: Schmidt Cassegrain telescope

$D_{1,RXA}/2$ . The power received by hypothetical receiving lens with the same radius as Cassegrain telescope is also depicted for comparison.

From the Fig. 6.5 the effect of obscuration is clearly visible. The received power is maximal when the radius of the beam is the same as the radius of the receiving aperture. However, the radius of the beam in real scenario has to be larger than receiver aperture because of pointing losses or beam wandering due to atmospheric turbulence. If the beam will be 4 times larger than receiver aperture then the received power by Cassegrain telescope will be almost the same as power received by hypothetical lens and the obscuration by secondary mirror is negligible.

## 6.4 Diffraction of the optical wave caused by Schmidt Cassegrain telescope

In FSO link, the receiver is irradiated by plane monochromatic wave with constant distribution of optical intensity. In our case the Schmidt Cassegrain telescope is used as a optical receiver system. This section deals with annular aperture diffraction caused by the circular aperture and secondary mirror obstruction of the Schmidt Cassegrain telescope. The central obstruction of the telescope affects the optical intensity distribution at the focal plane of the telescope. Because the light in fully photonic receiver is coupled to the optical fiber, one has to know to what extent the effect of diffraction on annular aperture influence the coupling efficiency of the Fully Photonic Link.

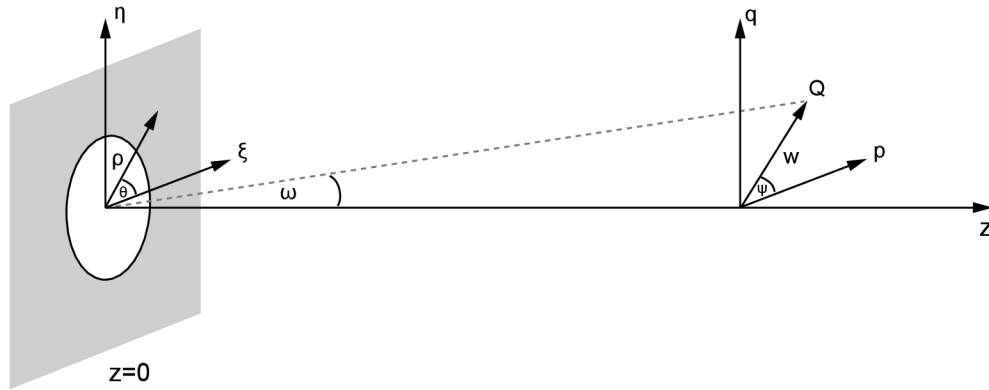


Fig. 6.7: Scheme for circular aperture diffraction

If the circular aperture is irradiated by a plane wave (Fig. 6.7), the Fraunhofer diffraction pattern formed at the focal plane of the telescope is called an Airy disk. The diffraction integral is written as [62]

$$U(Q) = C \int_0^a \int_0^{2\pi} \exp[-i k \rho \cos(\theta - \psi)] \rho d\rho d\theta, \quad (6.21)$$

where  $(\rho, \theta)$  are polar coordinates of the point at the plane of the aperture and  $(w, \psi)$  are coordinates of the point  $Q$  at the plane of the diffraction pattern. After integration it follows that for small angle  $\omega$  the function is [62]

$$U(Q) = C \pi a^2 \left[ \frac{2 J_1(k a \omega)}{(k a \omega)} \right]. \quad (6.22)$$

The constant  $C$  is defined by the power within the circular aperture  $P$ , diameter of the circular aperture  $D$  and distance of the diffraction pattern from the aperture

plane  $R$  [62]

$$C = \frac{1}{\lambda R} \sqrt{\frac{P}{D}}. \quad (6.23)$$

The intensity distribution within the diffraction pattern in the case of a clear circular aperture is characterized by the following relation [63]

$$I(Q) = |U(Q)|^2 = I_0 \left[ \frac{2 J_1(k a \omega)}{k a \omega} \right]^2, \quad (6.24)$$

where  $I_0$  is optical intensity at the maximum of the diffraction pattern,  $k$  is wave number of the incident optical wave,  $a$  is radius of the aperture and  $\omega$  angular radius. The angular radius of the Airy disk  $\omega_A$  is determined by the first minimum of the function (6.24). The first minimum of the function (6.24) occurs at  $k a \omega_A = 3.832$  (see Fig. 6.8).

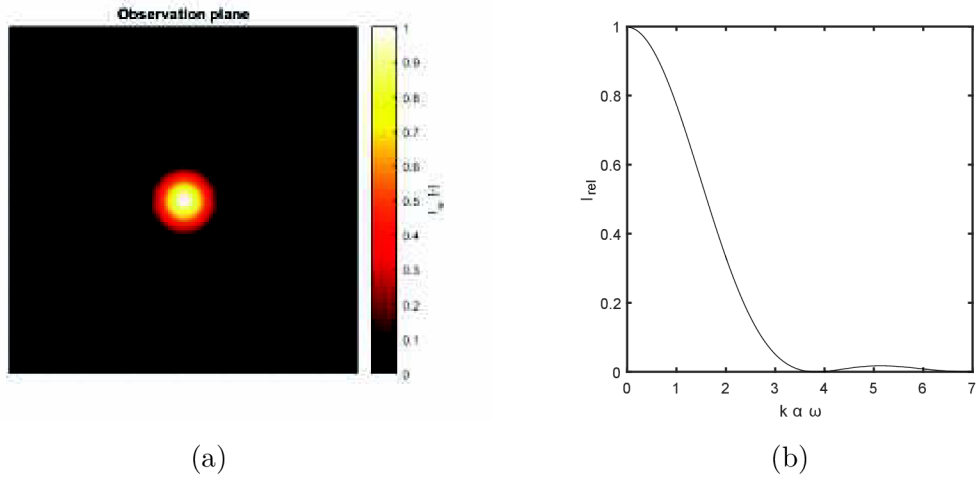


Fig. 6.8: Circular aperture diffraction

Angular radius of the Airy disk  $\omega_A$  is then given by

$$\omega_A = \frac{1.22 \lambda}{D} \quad (6.25)$$

where  $D$  is receiving aperture diameter. Radius of the Airy disk at the focal plane of the telescope can be calculated from the focal length of the telescope  $f$

$$r_A = f \omega_A = \frac{1.22 \lambda f}{D}. \quad (6.26)$$

When the obstruction of the telescope aperture by the secondary mirror is taken into account (Fig. 6.9), the aperture is not circular but annular. The diffraction on the mirrors of the Schmidt Cassegrain telescope was in our case approximated by

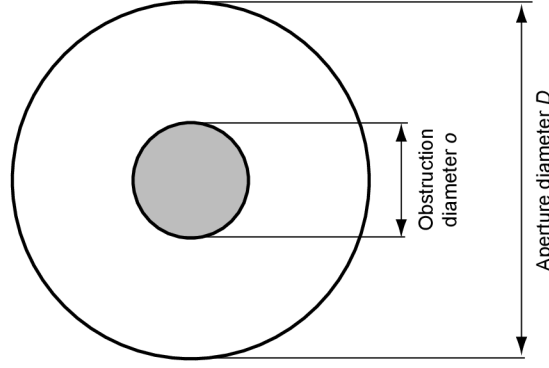


Fig. 6.9: Telescope aperture with central obstruction

diffraction on the annular aperture. If the annular aperture is irradiated by a plane wave, the diffraction pattern at the focal plane has the following character [62]

$$U(Q) = C \int_{\epsilon a}^a \int_0^{2\pi} \exp[-i k \rho \cos(\theta - \psi)] \rho d\rho d\theta, \quad (6.27)$$

where  $\epsilon$  is the ratio between the radius of the central obstruction  $o$  and aperture of the telescope  $D$

$$\epsilon = \frac{o}{D}. \quad (6.28)$$

After integration, [62] is obtained

$$U(Q) = C \pi a^2 \left\{ \left[ \frac{2 J_1(k a \omega)}{(k a \omega)} \right] - \epsilon^2 \left[ \frac{2 J_1(k \epsilon a \omega)}{(k \epsilon a \omega)} \right] \right\}. \quad (6.29)$$

The intensity at the diffraction pattern is represented as [62]

$$I(Q) = \frac{I_0}{(1 - \epsilon^2)^2} \left[ \frac{J_1(k a \omega) - \epsilon J_1(k \epsilon a \omega)}{k a \omega} \right]^2, \quad (6.30)$$

where  $I_0$  is optical intensity at the maximum of the diffraction pattern.

In Fig. 6.10, the function (6.30) is depicted for three different ratios between the radius of the central obstruction and aperture of the telescope. It is clear that the size of the secondary mirror plays an important role in optical distribution at the focal plane. By increasing the  $\epsilon$  parameter, the optical intensity within the diffraction pattern is distributed from the central disk to the diffraction rings. The resolving power of the system is increase because by increasing the parameter  $\epsilon$  the radius of the central disk decreases. From Fig. 6.10, it can be seen that by increasing the  $\epsilon$  parameter the power within the central disk decreases respectively. According to [64], the ratio of the power within the central diffraction disk to the total power is defined as

$$P_{rel} = \frac{\int_0^{\omega_{CD}} I \omega d\omega}{\int_0^{\infty} I \omega d\omega}, \quad (6.31)$$

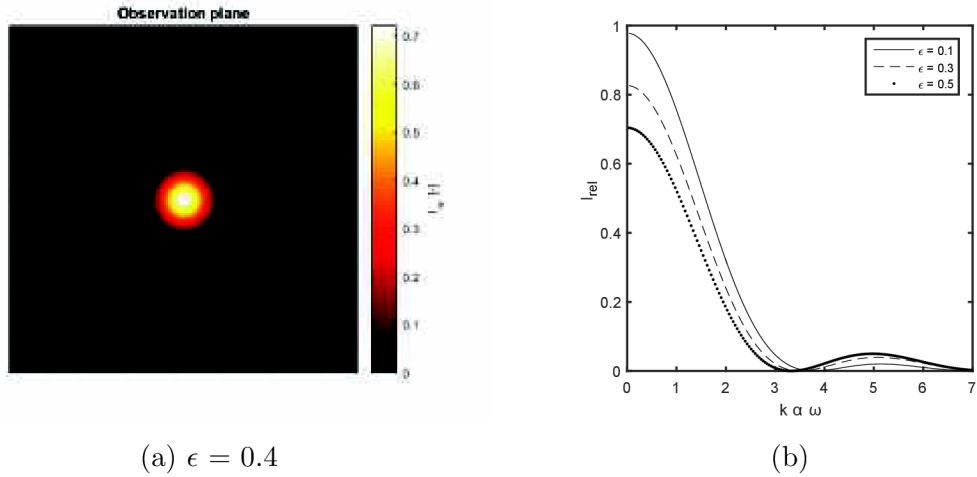


Fig. 6.10: Annular aperture diffraction

Tab. 6.1: Radius and relative power within the central diffraction disk [64]

$\epsilon$	$k a \omega$	$P_{rel} [-]$
0	3.832	0.838
0.10	3.786	0.818
0.15	3.733	0.795
0.20	3.665	0.764
0.25	3.586	0.732
0.30	3.501	0.682
0.40	3.323	0.584
0.50	3.144	0.479

where  $\omega_{CD}$  is the angular radius of the central diffraction disk.

In Tab. 6.1 from [64], the positions of the first minimum for different  $\epsilon$  and relative power within the central diffraction disk are listed.

It is possible to say, that obscuration by the second mirror affect the diffraction pattern at the focal plane of the telescope. The practical effect of having a central obstruction in a telescope is that the central disc becomes slightly smaller, and the first bright ring becomes brighter at the expense of the central disc. This becomes more problematic with short focal length telescopes which require larger secondary mirrors.[65]

The diameters of the primary and secondary mirrors of the Schmidt Cassegrain

telescope, Fig. 6.6, used in the FPR are  $D_{1, \text{RXA}} = 125 \text{ mm}$ ,  $D_{2, \text{RXA}} = 50 \text{ mm}$  respectively. The position of the first minima of the function (6.30) for parameter  $\epsilon = 0.4$  is theoretically 3.323. Therefore, the angular radius of the central diffraction disk  $\omega_{CD}$  at the focal plane of the telescope can be calculated as

$$k D_{1, \text{RXA}} \omega_{CD} = 3.232, \quad (6.32)$$

then

$$\omega_{CD} = \frac{1.05 \lambda}{D_{1, \text{RXA}}}. \quad (6.33)$$

When the focal length of the telescope is taken into account, the radius of the central diffraction disk  $r_{CD}$  is obtained as

$$r_{CD} = \frac{1.05 \lambda f}{D_{1, \text{RXA}}}. \quad (6.34)$$

The theoretical radius of the central disk at the focal plane of the Schmidt Cassegrain telescope is approximately  $15 \mu\text{m}$ . When the light is coupled to the SM optical fiber with radius  $5 \mu\text{m}$ , which is placed to the center of diffraction disk, one can estimate that the theoretical coupling loss for a perfectly aligned system is around 5 dB.

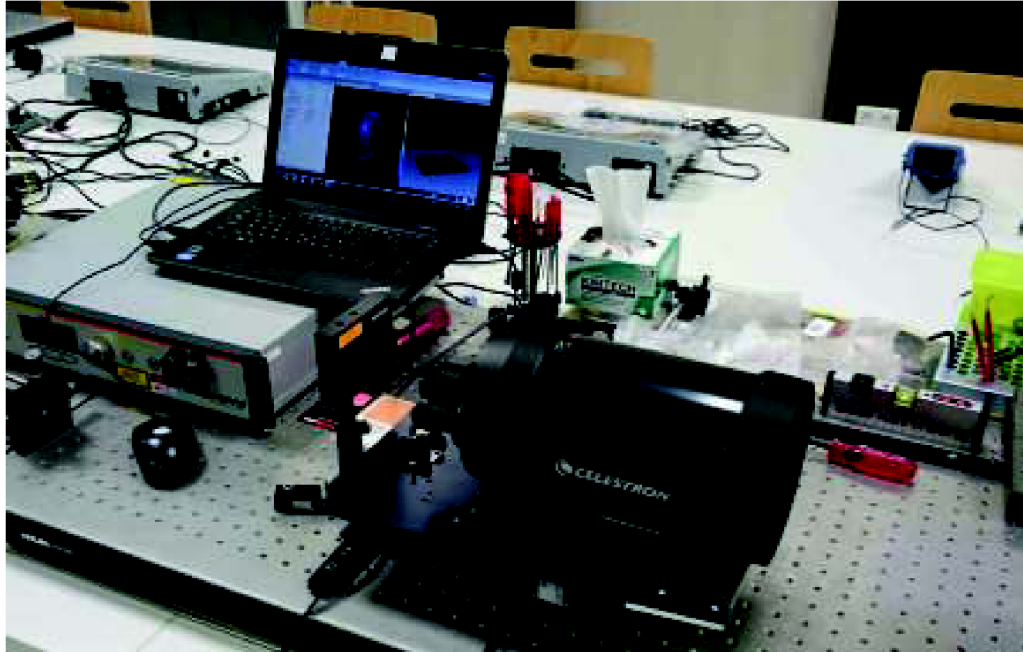


Fig. 6.11: Workplace for measuring the diffraction disk at the focal plane of the Schmidt Cassegrain telescope

In order to find out the real diameter of the central diffraction disk, an experimental measurement was carried out (Fig. 6.11). The Schmidt Cassegrain telescope



was irradiated by a coherent optical plane wave. Using the interference on the plane-parallel plate the collimation of light incident on the Schmidt Cassegrain telescope was checked. The optical intensity at the focal plane of the telescope was recorded with a CCD beam profiler.

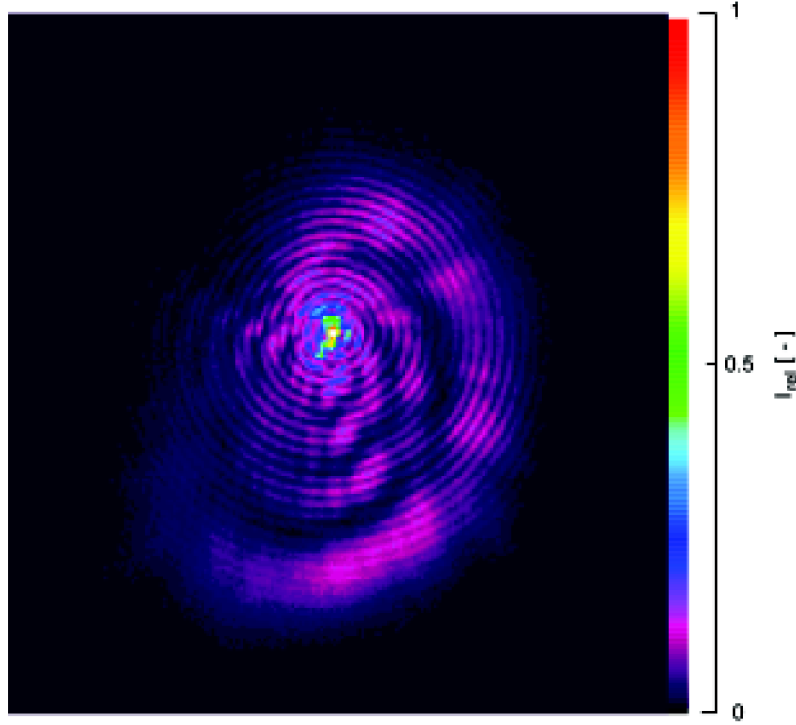


Fig. 6.12: Experimentally measured diffraction disk at the focal plane of the Schmidt Cassegrain telescope

The diffraction pattern at the focal plane of the telescope is depicted in Fig. 6.12. The real radius of the central diffraction disc (white area in the center of the diffraction pattern) is around  $20 \mu\text{m}$  which is very close to the theoretical expectations. The power contained in this area is much bigger than the power in the rest of the diffraction pattern.

In the case of FPR, the single mode optical fiber with collimating optics is placed to the center of the diffraction pattern when the maximum power is achieved. From a simple calculation, the coupling loss in the real scenario when the light from the telescope is coupled into the SM fiber is around 6 dB. From Fig. 6.12, it is visible that some parasitic diffraction effects are present. The bigger diffraction rings are caused by diffraction of the optical wave on the central obstruction while the smaller diffraction rings are caused by the finite aperture of the telescope.

## 6.5 Testing Transmitter

For the estimation of the coupling efficiency of the FPR (free space to SM fiber), it was necessary to design the Testing Transmitter (TT). The TT should irradiate whole receiving aperture of the FPR under test.

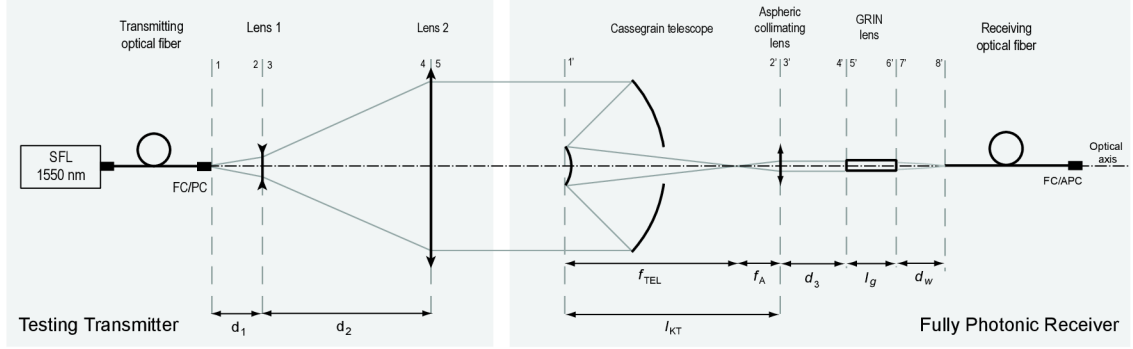


Fig. 6.13: Configuration of the testbed which consist of Testing Transmitter and Fully Photonic Receiver. SFL - Single Frequency Laser, Lens 1 - plano-concave lens with focal length  $f_1 = -30 \text{ mm}$ , Lens 2 - plano-convex lens with focal length  $f_2 = 300 \text{ mm}$ ,  $f_{TEL}$  - focal length of the Cassegrain telescope,  $f_A$  - focal length of the aspheric collimating lens,  $l_g$  - length of the GRIN lens,  $d_w$  - working distance of the GRIN lens.

The Single Frequency laser in TT with wavelength of 1550 nm was used as a source and then it was coupled to the single-mode fiber with radius  $5 \mu\text{m}$ . The sufficient irradiation of the receiver (FPR) aperture is ensured with beam expander which consist of two lenses Lens 1 and Lens 2 (Fig. 6.13). The design of the beam expander was carried out with geometrical optics. The transmitting optical fiber irradiates the Lens 1 from the distance  $d_1$ . This distance is represented by translation matrix

$$\mathbf{M}_{12} = \begin{bmatrix} 1 & d_1 \\ 0 & 1 \end{bmatrix}. \quad (6.35)$$

The Lens 1 was assumed as a thin lens with focal length  $f_1$  with refraction matrix

$$\mathbf{M}_{23} = \begin{bmatrix} 1 & 0 \\ -1/f_1 & 1 \end{bmatrix}. \quad (6.36)$$

In order to collimate the wave emanating from the transmitting fiber the distance between the Lens 1 and Lens 2 is given by difference of the absolute value of their focal lengths

$$\mathbf{M}_{34} = \begin{bmatrix} 1 & d_2 \\ 0 & 1 \end{bmatrix}. \quad (6.37)$$

Then the Lens 2 was modelled as a refraction matrix of the thin lens with focal length  $f_2$

$$\mathbf{M}_{45} = \begin{bmatrix} 1 & 0 \\ -1/f_2 & 1 \end{bmatrix}. \quad (6.38)$$

The ray transfer matrix of the TT can be calculated as follows

$$\mathbf{M}_T = \mathbf{M}_{45} \cdot \mathbf{M}_{34} \cdot \mathbf{M}_{23} \cdot \mathbf{M}_{12}. \quad (6.39)$$

And finally the elements of the  $M_T$

$$\mathbf{M}_T = \begin{bmatrix} A_T & B_T \\ C_T & D_T \end{bmatrix}, \quad (6.40)$$

are derived

$$A_T = 1 - \frac{d_2}{f_1}, \quad (6.41)$$

$$B_T = d_2 - \frac{d_1((d_2 - f_1))}{f_1}, \quad (6.42)$$

$$C_T = \frac{d_2 - f_1}{f_1 f_2} - \frac{1}{f_1}, \quad (6.43)$$

$$D_T = \frac{d_1(d_2 - f_2)}{f_1 f_2} - \frac{d_1 + d_2 - f_2}{f_2}. \quad (6.44)$$

From the ray transfer matrix the TT was set up in order to get collimated beam at the output.

## 6.6 Coupling efficiency

The complex envelope of a Gaussian beam is defined by the complex  $q$  parameter

$$\frac{1}{q(z)} = \frac{1}{R(z)} - j \frac{\lambda}{\pi w^2(z)}, \quad (6.45)$$

where  $R(z)$  is the radius of the curvature and  $w(z)$  is the radius of the beam waist. The properties of the optical system centered about the propagation axis can be described by the ray transfer matrix. Therefore the  $q_2$  parameter of the Gaussian beam after the passage through an optical system can be deduced from an ABCD law as follows

$$q_2 = \frac{Aq_1 + B}{Cq_1 + D}, \quad (6.46)$$

where  $q_1$  is the parameter of the input Gaussian beam and A, B, C, D are elements of the ray transfer matrix. After substitution of the Eq. (6.45) into the previous equation the radius of curvature and the beam waist radius can be derived as

$$R_2 = \frac{w_1^4 \pi^2 \left(A + \frac{B}{R_1}\right)^2 + B^2 \lambda^2}{w_1^4 \pi^2 \left(A + \frac{B}{R_1}\right) \left(C + \frac{D}{R_1}\right) + BD \lambda^2}, \quad (6.47)$$

$$w_2 = \sqrt{\frac{w_1^4 \pi^2 \left(A + \frac{B}{R_1}\right)^2 + B^2 \lambda^2}{w_1^2 \pi^2 (AD - BC)}}. \quad (6.48)$$

From these equations the  $q_2$  parameter of the output Gaussian beam can be obtained.

In order to estimate the coupling efficiency of the optical receiver I used analytical Near-Field Method proposed by Kataoka [66]. The overlap integral characterizes the coupling efficiency between incident light and SM optical fiber [66]

$$\eta = \frac{\left| \int \psi_L \psi_F dr \right|^2}{\int |\psi_L|^2 dr \int |\psi_F|^2 dr}, \quad (6.49)$$

where  $\psi_L$  is relative field amplitude of the incident light and  $\psi_F$  is relative field amplitude of the optical fiber mode. It should be noted that the coupling efficiency expressed by equation (6.49) does not take into account any optical aberration. Equation (6.49) is only shown to be valid under assumption that the system is stationary and polarization independent and nonlinear effects does not occur. Optical fiber field amplitude is [66]

$$\psi_F = \sqrt{\frac{2}{\pi}} \frac{1}{w_F} \exp\left(-\frac{r^2}{w_F^2}\right), \quad (6.50)$$

where  $w_F$  is mode field radius of the fiber. I assume that the incident beam is a circularly symmetrical in terms of the radial coordinate  $r$ . Then the field amplitude of the incident light focused on the optical fiber is characterised as [66]

$$\psi_L = \sqrt{\frac{2}{\pi w_L^2}} \exp\left(-\frac{r^2}{w_L^2}\right), \quad (6.51)$$

where  $w_L$  is radius of the incident Gaussian beam. The coupling efficiency  $\eta$  is then defined as [66]

$$\eta(\Delta_x, \Delta_z) = \frac{4}{\left(\frac{w_F}{w_L} + \frac{w_L}{w_F}\right)^2 + \frac{\lambda^2 \Delta_z^2}{\pi^2 w_F^2 w_L^2}} \exp\left(-\frac{4\Delta_x^2}{w_F^2 + w_L^2}\right), \quad (6.52)$$

$$\eta(\alpha) = \exp\left(-\frac{2\pi^2}{\lambda^2} \frac{\alpha^2 w_F^2 w_L^2}{(w_F^2 + w_L^2)}\right), \quad (6.53)$$

where  $\Delta_x$  is lateral deviation,  $\Delta_z$  is defocus deviation and  $\alpha$  is angular deviation of the receiving fiber (Fig. 6.14). Relation between FPR coupling efficiency and FPR coupling loss can be defined by expression

$$\alpha_{CL} = 10 \log \frac{1}{\eta}, \quad (6.54)$$

where  $\alpha_{CL}$  is coupling loss in dB.

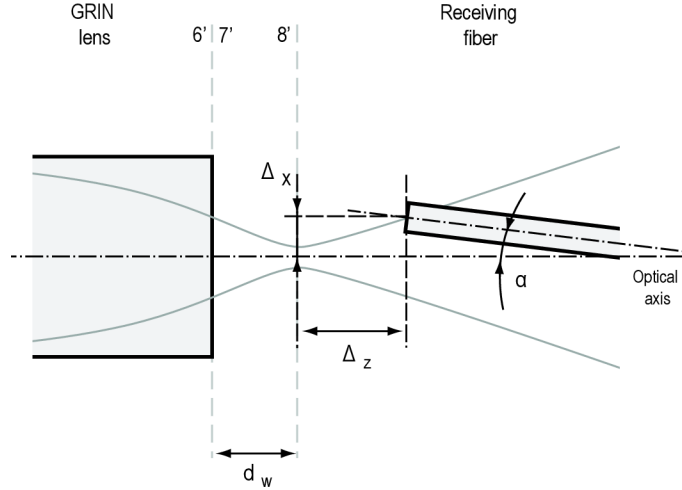


Fig. 6.14: Receiving fiber alignment deviations

Testbed parameters are listed in Table 6.2. The parameters of the Gaussian beam emanating from the transmitting fiber (at the plane 1) are  $w_1$  and  $R_1$ . The beam waist of the Gaussian beam was placed exactly to back focal point of the Lens 1. From these parameters it is possible to obtain parameter  $q_1$  from Eq. 6.45. I used the ray transfer matrices  $M_T$  and  $M_R$  in order to transform the  $q_1$  into the  $q_2$  parameter according to ABCD law (Eq. 6.46). Therefore I can calculate the parameters of the Gaussian beam behind the receiver at the plane 8'. The radius of curvature  $R_2$  and beam radius  $w_2$  of the transformed Gaussian beam was calculated from Eq. 6.47 and Eq. 6.48. The beam radius at the focus point of the GRIN lens is  $w_2 = 17.4 \mu m$  and the radius of curvature  $R_2$  is infinite.

The FPR coupling efficiency was investigated for single-mode fiber with field radius  $w_F = 4.5 \mu m$ . Once we know the field amplitude distribution of the optical fiber and incident light at the plane 8', we can estimate coupling efficiency from Eq. 6.52 and Eq. 6.53. The coupling loss in dB was determined according to Eq. 6.54. We obtained the coupling loss 5.2 dB for perfectly aligned system. To find out how the system will be sensitive to the alignment procedure, the coupling loss as a function of lateral deviation (Fig. 6.20), angular deviation (Fig. 6.21) and defocus deviation (Fig. 6.17) are depicted.

Tab. 6.2: Parameters of the testbed

<b>TT parameters</b>	
Wavelength $\lambda$	1550 nm
Beam waist radius $w_1$	$4.5 \mu\text{m}$
Radius of curvature $R_1$	$\infty$
Focal length of the Lens 1 $f_1$	-30 mm
Focal length of the Lens 2 $f_2$	300 mm
Distance $d_1$	30 mm
<b>FPR parameters</b>	
Focal length of the Cassegrain telescope $f_{tel}$	1250 mm
Aperture radius of the Cass. telescope $D_{RXA}/2$	62.5 mm
Focal length of the aspheric lens $f_A$	4.51 mm
Distance $d_3$	1 mm
GRIN lens length $l_g$	4.43 mm
Gradient constant of the GRIN lens $g$	$326 \text{ m}^{-1}$
Index of refraction at center of the GRIN lens $n_g$	1.5901
Working distance of the GRIN lens $d_w$	0.39 mm

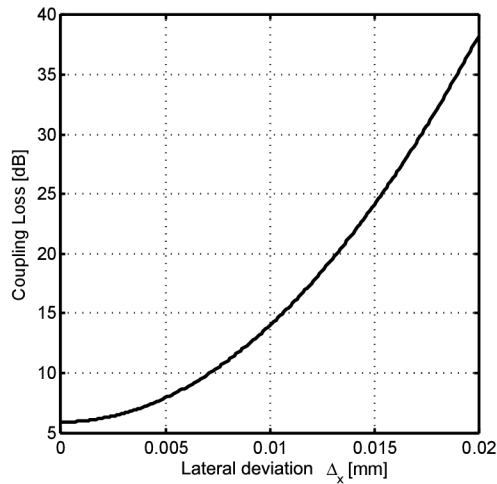


Fig. 6.15: The coupling loss of the FPR as a function of the lateral deviation.

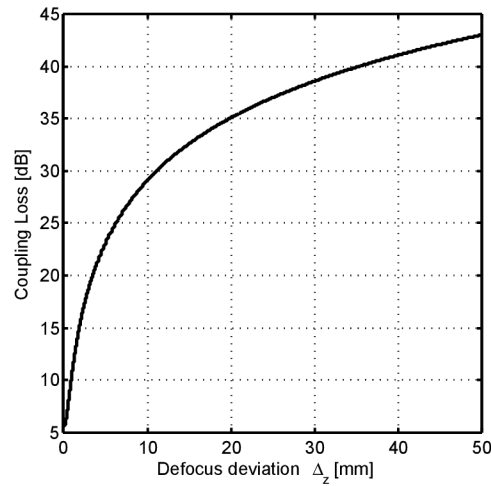


Fig. 6.16: The coupling loss of the FPR as a function of the defocus deviation.

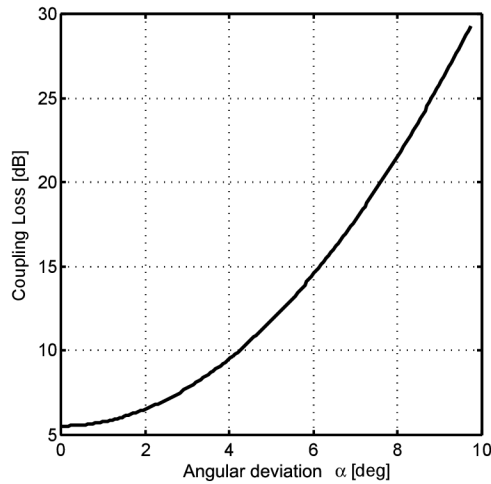


Fig. 6.17: The coupling loss of the FPR as a function of angular deviation.

According to these figures it is clear that alignment of the system is quite challenging, which indicates that some kind of adaptive technique should be used. For achievement of the sufficient power level the Erbium-doped Fiber Amplifier can be used conveniently.

## 6.7 Experimental measurement of the coupling loss

The system theoretically described in previous subsection was build up and tested. The testbed is depicted in Fig. 6.18. Construction elements from Thorlabs were

used to build the system.

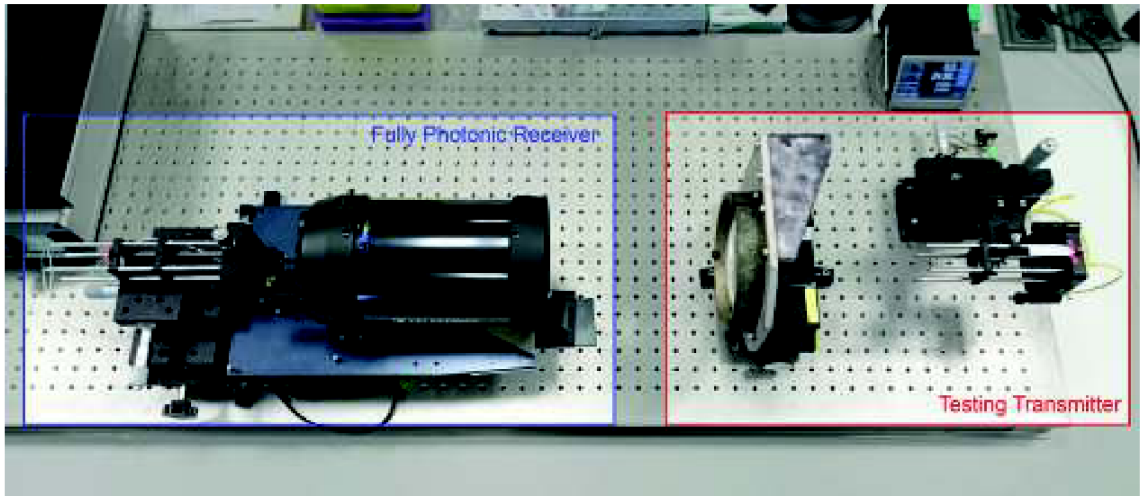


Fig. 6.18: Testbed for testing of the fully photonic receiver

The coupling loss of the fully photonic receiver was measured for lateral and defocus deviation (see Fig. 6.19). Mechanical arrangement of the receiver does not allow movement of the fiber tip. The GRIN element which is attached to the fiber and aspheric collimating lens are placed in one housing. Thus, we could move only with whole element instead of fiber. For this reason the measured values of the coupling loss are not the same. However, for the perfect alignment of the system the coupling loss is about 6 dB, which is close to the theoretical estimation.

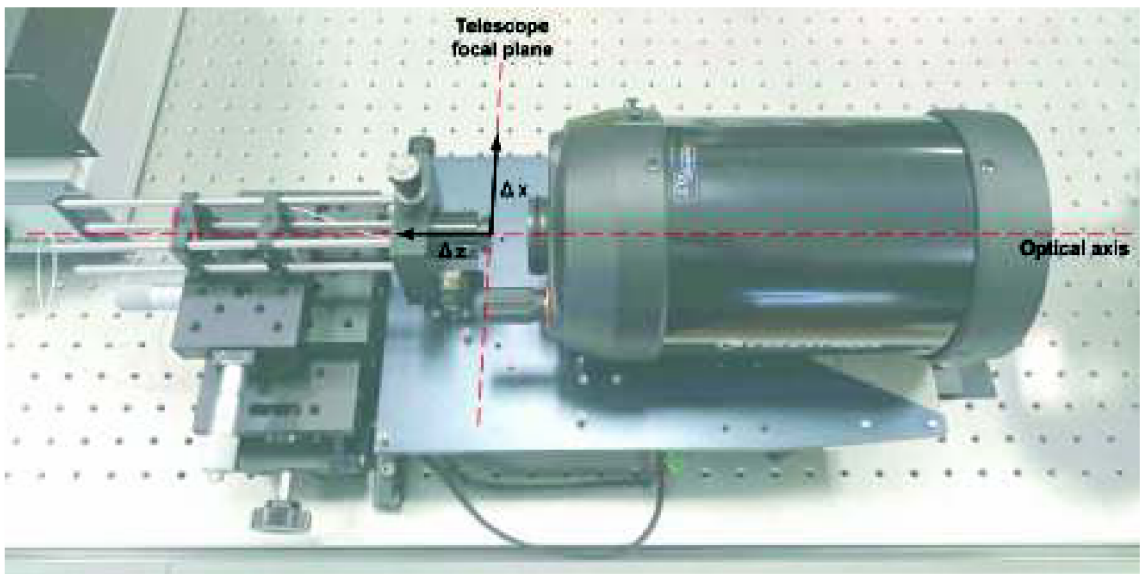


Fig. 6.19: Scheme for the measurement of coupling loss



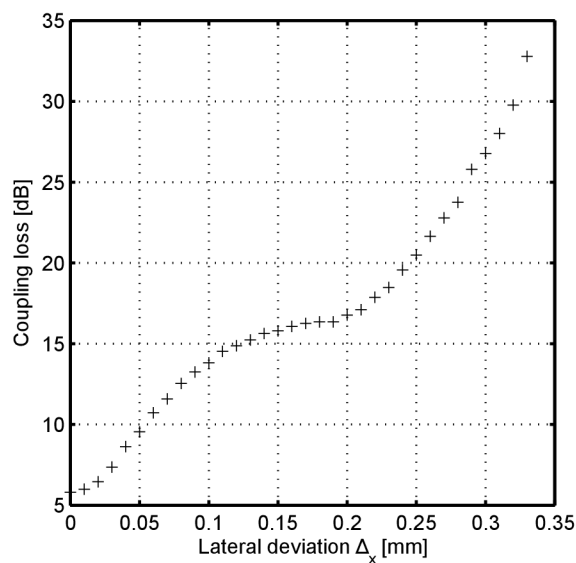


Fig. 6.20: The coupling loss of the FPR as a function of the lateral deviation.

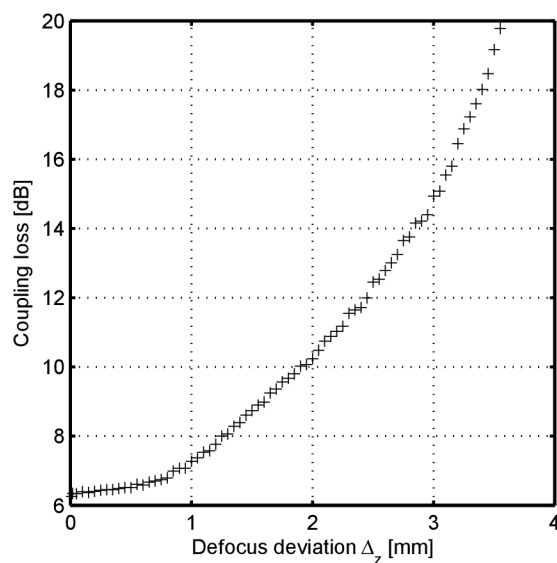


Fig. 6.21: The coupling loss of the FPR as a function of the defocus deviation.

## 6.8 Channel Characterization

A schematic concept of the fully photonic link is shown in Fig. 6.22. The input optical signal with wavelength 1550 nm is boosted in EDFA. The amplified signal (100 mW) is then led by single mode optical fiber to the transmitter, where large core fiber irradiates the transmitting lens. The optical Gaussian beam emanating from the transmitter ( $D_{\text{TXA}} = 25.4$  mm) has divergence  $\theta = 1$  mrad. After

propagation through the free space channel, the beam is received by the Schmidt-Cassegrain telescope (primary mirror diameter  $D_{1,RXA} = 125$  mm, secondary mirror diameter  $D_{2,RXA} = 50$  mm). The amount of the received power can be calculated by equation 6.19. The signal received by the Schmidt-Cassegrain telescope is then amplified by EDFA and filtered by a tunable fiber filter. The filtered optical signal is then distributed where it is needed. Example of possible energetic balance of the link was calculated in a special program which takes into account the statistical characteristics of the area. The results are shown in Tab. 6.3.

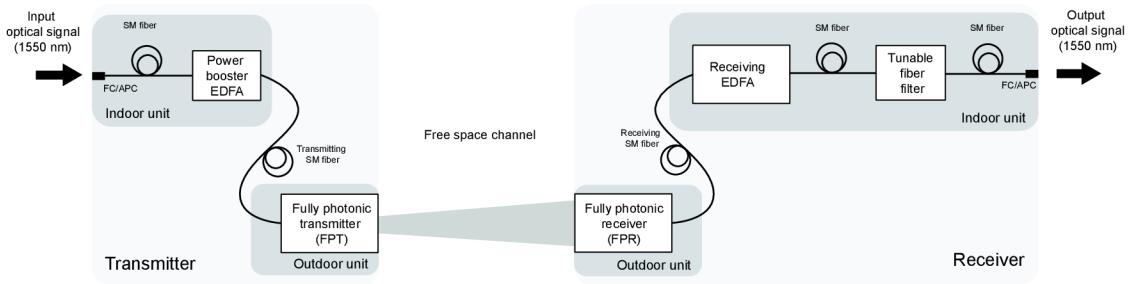


Fig. 6.22: Concept of the fully photonic link.

One of the effects caused by atmospheric turbulences, which have an essential impact on availability of the fully photonic link, is fluctuations of the angle of arrival. The incident angle is defined as the angle between the direction of propagation of an optical wave which is incident to the plane of the receiving aperture and optical axis of the receiver [23]. Fluctuations of angle of arrival have direct impact on coupling efficiency of a fully photonic link. As a consequence of angle of arrival fluctuation, the focused optical wave is shifted from the optical axis (image jitter) in the focal plane of the telescope. Due to this shift, the coupling loss increases.

The magnitude of angle of arrival fluctuation depends on the strength of the atmospheric turbulence. The strength of atmospheric turbulence is characterized by the refractive index structure parameter  $C_n^2$ . In the area of operation we expected values of the  $C_n^2$  parameter between  $10^{-13} \text{ m}^{-2/3}$  and  $10^{-14} \text{ m}^{-2/3}$ . It is assumed that the receiver will be placed at the far field; therefore we used relations for a spherical wave.

After substituting of the link parameters (Tab. 6.3) to the relation (1.23) we obtain variance of the angle of arrival approximately  $8 \mu\text{rad}$ . Fluctuations of the angle of arrival in the focus plane of the telescope create an offset of the focus sometimes called “image jitter” or “image dancing”. Owing to image jitter, the direction of propagation of light is changed at the input plane of the receiving fiber which causes coupling loss ( $\alpha_{CL}$ ).

<b>Transmitted optical power (mean)</b>	$P_{m, \text{TXA}}$	19.5	dBm
<b>Beam divergence</b>	$\theta$	1	mrad
<b>Link distance</b>	$L$	850	m
<b>Wavelength</b>	$\lambda$	1550	nm
<b>Transmitter system loss</b>	$\alpha_{\text{trans, syst}}$	5.5	dB
<b>Atmospheric loss</b>	$\alpha_{\text{atm}}$	1	dB
<b>Propagation loss</b>	$\alpha_{\text{prop}}$	37	dB
<b>Diameter of receiving antenna (the primary mirror)</b>	$D_{1, \text{RXA}}$	125	mm
<b>Diameter of receiving antenna (the secondary mirror)</b>	$D_{1, \text{RXA}}$	50	mm
<b>Equivalent diameter of the (receiving antenna)</b>	$D_{\text{Eq, RXA}}$	114	mm
<b>Total gain of the receiver</b>	$\gamma_{\text{total}}$	17	dB
<b>Received power</b>	$P_{\text{RXA}}$	-7	dBm
<b>Receiver system loss</b>	$\alpha_{\text{rec, syst}}$	15.5	dB
<b>Receiver sensitivity (mean)</b>	$P_{0, \text{RXA}}$	-38	dBm
<b>Margin of the link</b>	$M$	15.5	dB

Tab. 6.3: Link budget.

The “image jitter” can be calculated as the root mean square angle of arrival multiplied by the focal length of the receiving telescope [22]. However, we have to take into account the whole receiving optical system including the collimating aspheric lens and GRIN lens. For this, I used relation (6.2) for estimating of the image displacement at the input plane of the receiving fiber. The value of image jitter is approximately 5  $\mu\text{m}$ . From this value one can estimate the additional coupling loss caused by the angle of arrival from Fig. 6.21. The loss is about 2 dB. For this particular application of the fully photonic link, the loss caused by the angle of arrival fluctuations is fully acceptable (see link margin in Tab. 6.3).

## 6.9 Summary

This chapter was focused on modeling and designing a fully photonic link which is used primarily for transmitting a highly stable optical frequency – transmission of time. The fully photonic concept of the link brings a number of benefits which improve qualitative parameters of the link: creation of an optimal intensity profile of the transmitting beam, usage of photonic devices such as WDM and EDFA, etc. A fully photonic transceiver only uses passive optical components without any electronic and optoelectronic devices. Lasers, photodiodes, fiber amplifiers and supply blocks are used in the indoor unit which is not so strongly affected by atmospheric changes as the outdoor unit is. An extremely wide band can be achieved by excluding the blocks performing E/O conversion from the communication channel.

However, transmission of a highly stable optical frequency with a fully photonic link requires good knowledge of the conditions under which the link will be working. These include statistical parameters of the atmosphere like time dispersion and the effect of random attenuation and turbulence.

The received power by the fully photonic receiver is highly dependent on the fluctuation of the angle of the incident optical wave. The angle of arrival variance caused by atmospheric turbulences was estimated within this chapter. From theoretical prediction, it was assumed that the loss caused by the angle of arrival variance does not exceed the margin of the particular link.

## 7 CONCLUSION

The doctoral thesis was focused on analysing the distribution of optical intensity within a laser beam at the transmitting aperture which is affected by propagation through free space as well as through the atmosphere. The aim of the thesis was to determine the optimal intensity distribution of the laser beam which is minimally affected by turbulence during the propagation. In the first part of the thesis the overall insight into the problem of Gaussian and Flattened Gaussian beam propagation through atmospheric turbulence was given. The numerical models of particular effects which influence beam quality are discussed. The various types of beam shapes were mentioned.

The numerical simulation of the arbitrary optical wave propagation through atmospheric turbulence was utilized and the results from the simulation were used in order to verify the theoretical models. From the theoretical analysis, it is assumed that the top-hat or Flattened Gaussian beam should have a lower scintillation index in comparison with the Gaussian beam. The simulation also showed that the aperture averaging effect has essential impact on scintillation reduction. Therefore the signal to noise ratio at the receiver increases.

Based on these findings, the available methods of beam shaping were studied. A refraction beam shaper for an FSO communication transmitter was designed. The design was performed by a geometric design method which is based on numerical calculation of two plano-aspheric lenses. The final design was verified in the optical design software ZEMAX. The next possible option is using the plastic optical fiber as a beam shaper. For that case the optical intensity distribution of three different optical fibers was investigated. The output from the plastic optical fiber is created by thousand of modes whose envelope is similar to the Flattened Gaussian beam. Because the light emanating from the plastic optical fiber is partially coherent, the scintillation level could be reduced more.

The last chapter deals with modelling and designing a fully photonic link which will be used primarily for transmitting a highly stable optical frequency. The concept of a fully photonic transmitter was utilized. The optimal shape of the transmitted optical beam is ensured by a plastic optical fiber which irradiates the transmitting lens. The emanating optical beam has an optimal shape which is more resistant to the negative effects of atmospheric turbulence. The most challenging part of the fully photonic link is to design the fully photonic receiver. The aim of the receiver is to couple the light captured by the Schmidt Cassegrain telescope to the single mode optical fiber. The critical aspects which influence the coupling efficiency were discussed and modelled. The optical intensity distribution at the focal plane of the telescope and the effect of secondary mirror obscuration on resolving power was

investigated by Fraunhofer diffraction. It was found that the obscuration by the secondary mirror improves the resolving power of the telescope which means that the central diffraction disk has a lower radius in comparison with a clear aperture. However, less energy is included within the central diffraction disk. The fully photonic receiver coupling efficiency was estimated for a perfectly aligned system and for lateral, angular and defocus deviations. The modelled results were compared with experimental measurement on a testbed. Lastly the link budget and concept of the fully photonic link is given. The main contribution of this chapter is utilizing a fully photonic link with a beam shaper which is ready for experimental testing.

## BIBLIOGRAPHY

- [1] I. E. LEE, Z. GHASSEMLOOY, S. MEMBER, and W. P. NG, “Effects of Aperture Averaging and Beam Width on Gaussian Free Space Optical Links in the Presence of Atmospheric Turbulence and Pointing Error,” in *14th International Conference on Transparent Optical Networks (ICTON), 2012*, 2012, pp. 2–5.
- [2] P. KAUR, V. K. JAIN, and S. KAR, “Capacity of free space optical links with spatial diversity and aperture averaging,” *2014 27th Biennial Symposium on Communications (QBSC)*, vol. 6, no. 3, pp. 14–18, Jun. 2014. [Online]. Available: <http://ieeexplore.ieee.org/lpdocs/epic03/wrapper.htm?arnumber=6841175>
- [3] L. YANG, X. GAO, and M.-S. ALOUINI, “Performance Analysis of Free-Space Optical Communication Systems With Multiuser Diversity Over Atmospheric Turbulence Channels,” *IEEE Photonics Journal*, vol. 6, no. 2, pp. 1–17, Apr. 2014. [Online]. Available: <http://ieeexplore.ieee.org/lpdocs/epic03/wrapper.htm?arnumber=6766188>
- [4] M.-A. KHALIGHI, N. SCHWARTZ, N. AITAMER, and S. BOURENNANE, “Fading Reduction by Aperture Averaging and Spatial Diversity in Optical Wireless Systems,” *Journal of Optical Communications and Networking*, vol. 1, no. 6, p. 580, Oct. 2009. [Online]. Available: <http://www.opticsinfobase.org/abstract.cfm?URI=JOCN-1-6-580>
- [5] A. GARCIA-ZAMBRANA, C. CASTILLO-VAZQUEZ, and B. CASTILLO-VAZQUEZ, “Outage performance of MIMO FSO links over strong turbulence and misalignment fading channels.” *Optics express*, vol. 19, no. 14, pp. 13 480–13 496, 2011.
- [6] H. T. EYYBOGLU, Y. BAYKAL, E. SERMUTLU, O. KOROTKOVA, and Y. CAI, “Scintillation index of modified Bessel-Gaussian beams propagating in turbulent media.” *Journal of the Optical Society of America. A, Optics, image science, and vision*, vol. 26, no. 2, pp. 387–94, Feb. 2009. [Online]. Available: <http://www.ncbi.nlm.nih.gov/pubmed/19183693>
- [7] H. T. EYYBOGLU, Y. BAYKAL, E. SERMUTLU, and Y. CAI, “Scintillation advantages of lowest order Bessel-Gaussian beams,” *Applied Physics B: Lasers and Optics*, vol. 92, pp. 229–235, 2008.
- [8] V. KOLLAROVA, T. MEDRIK, and R. CELECHOVSKY, “Application of nondiffracting beams to wireless optical communications,” *Proc. SPIE*, 2007.

- [Online]. Available: [http://www.opto.cz/tandem/publikace\\_pdf/%5B17%5D.pdf](http://www.opto.cz/tandem/publikace_pdf/%5B17%5D.pdf)
- [9] Y. CAI, “Propagation of various flat-topped beams in a turbulent atmosphere,” *Journal of Optics A: Pure and Applied Optics*, vol. 8, no. 6, pp. 537–545, Jun. 2006. [Online]. Available: <http://stacks.iop.org/1464-4258/8/i=6/a=008?key=crossref.d13f4016e37b776969a02269adef92a2>
- [10] M. ALAVINEJAD, B. GHAFARY, and F. KASHANI, “Analysis of the propagation of flat-topped beam with various beam orders through turbulent atmosphere,” *Optics and Lasers in Engineering*, vol. 46, no. 1, pp. 1–5, Jan. 2008.
- [11] H. T. EYYBOGLU, C. ARPALI, and Y. K. BAYKAL, “Flat topped beams and their characteristics in turbulent media.” *Optics express*, vol. 14, no. 10, pp. 4196–207, May 2006.
- [12] L. C. ANDREWS, R. L. PHILLIPS, and C. Y. HOPEN, *Laser Beam Scintillation With Applications*, ser. Spie Press Monograph. SPIE Press, 2001.
- [13] S. ZVANOVEC, J. PEREZ, Z. GHASSEMLOOY, S. RAJBHANDARI, and J. LIBICH, “Route diversity analyses for free-space optical wireless links within turbulent scenarios.” *Optics express*, vol. 21, no. 6, pp. 7641–50, 2013. [Online]. Available: <http://www.ncbi.nlm.nih.gov/pubmed/23546147>
- [14] V. E. ZUEV, *Laser Beams in the Atmosphere*, 1st ed. Springer US, 1982.
- [15] C. N. REINHARDT, S. M. HAMMEL, K. MCBRYDE, and D. TSINTIKIDIS, “Improved vertical refractive-index structure parameter model for the maritime atmosphere based on local bulk meteorological measurements,” pp. 85 170L–85 170L–10, 2012. [Online]. Available: <http://dx.doi.org/10.1117/12.973361>
- [16] C. WILSON, A. M. van EIJK, and E. FEDOROVICH, “Retrieval of structure functions of air temperature and refractive index from large eddy simulations of the atmospheric boundary layer,” vol. 8874, p. 887408, 2013. [Online]. Available: <http://proceedings.spiedigitallibrary.org/proceeding.aspx?doi=10.1117/12.2023990>
- [17] A. K. MAJUMDAR, *Advanced Free Space Optics (FSO): A Systems Approach*. Springer, 2014.
- [18] A. MAJUMDAR and J. RICKLIN, *Free-Space Laser Communication: Principles and Advances*. Springer Science+Business Media, 2008.



- [19] Y. DIKMELIK, “Dember Effect Photodetectors and the Effects of Turbulence on Free-Space Optical Communication Systems,” Ph.D. dissertation, The Johns Hopkins University, 2004.
- [20] W. O. POPOOLA, “Subcarrier Intensity Modulated Free-Space Optical Communication Systems,” Ph.D. dissertation, Northumbria University, 2009.
- [21] J. C. DAINTY, *Laser Guide Star Adaptive Optics for Astronomy - Optical Effects of Atmospheric Turbulence*. Springer Netherlands, 2000.
- [22] L. C. ANDREWS, *Field Guide to Atmospheric Optics*. SPIE Press, 2004.
- [23] L. C. ANDREWS and R. L. PHILLIPS, *Laser Beam Propagation Through Random Media*, ser. Press Monographs. SPIE Press, 2005.
- [24] D. COWAN, “Effects of Atmospheric Turbulence on the Propagation of Flattened Gaussian Optical Beams,” Ph.D. dissertation, University of Central Florida Orlando, Florida, 2006.
- [25] J. H. CHURNSIDE and R. J. LATAITIS, “Angle-of-arrival fluctuations of a reflected beam in atmospheric turbulence,” *Journal of the Optical Society of America A*, vol. 4, no. 7, p. 1264, Jul. 1987. [Online]. Available: <http://www.opticsinfobase.org/abstract.cfm?URI=josaa-4-7-1264>
- [26] B. EPPLE, H. HENNIGER, S. KURZ, and H. HAAN, “Rural Optical-Propagation Measurements,” *Radioengineering*, vol. 20, no. 1, pp. 49–54, 2011.
- [27] A. PROKES and L. BRANCIK, “Degradation of free space optical communication performance caused by atmospheric turbulence,” *2012 2nd International Conference on Advances in Computational Tools for Engineering Applications (ACTEA)*, no. 2, pp. 338–341, 2012. [Online]. Available: <http://ieeexplore.ieee.org/lpdocs/epic03/wrapper.htm?arnumber=6462896>
- [28] H.-C. KIM and Y. H. LEE, “Hermite-Gaussian and Laguerre-Gaussian beams beyond the paraxial approximation,” *Optics Communications*, vol. 169, no. October, pp. 9–16, 1999. [Online]. Available: <http://www.sciencedirect.com/science/article/pii/S0030401899004113>
- [29] H. T. EYYBOGLU, Y. BAYKAL, and X. JI, “Scintillations of Laguerre Gaussian beams,” *Applied Physics B: Lasers and Optics*, vol. 98, pp. 857–863, 2010.
- [30] H. T. EYYBOGLU and Y. BAYKAL, “Analysis of reciprocity of cos-Gaussian and cosh- Gaussian laser beams in a turbulent atmosphere.” *Opt Express*, vol. 12, no. 20, pp. 4659–4674, 2004.

- [31] Y. BAYKAL, H. T. EYYBOGLU, and Y. CAI, “Effect of beam types on the scintillations: a review,” in *Proc. SPIE 7200*, 2009, pp. 720 002–720 002–15.
- [32] Y. CHEN, Y. CAI, H. T. EYYBOGLU, and Y. BAYKAL, “Scintillation properties of dark hollow beams in a weak turbulent atmosphere,” *Applied Physics B: Lasers and Optics*, vol. 90, pp. 87–92, 2008.
- [33] H. GERCEKCIOGLU, Y. BAYKAL, and C. NAKIBOGLU, “Annular beam scintillations in strong turbulence.” *Journal of the Optical Society of America A, Optics, image science, and vision*, vol. 27, no. 8, pp. 1834–9, Aug. 2010. [Online]. Available: <http://www.ncbi.nlm.nih.gov/pubmed/20686588>
- [34] J. SCHMIDT, *Numerical Simulation of Optical Wave Propagation With Examples in MATLAB*. SPIE Press, 2010.
- [35] T. POON, T.C. KIM, *Engineering Optics With Matlab*. World Scientific Publishing Company Incorporated, 2006.
- [36] NAROTTAM DAS, *Optical Communications Systems*. InTech, 2012.
- [37] N. RODDIER, “Atmospheric wavefront simulation using Zernike polynomials,” 2013.
- [38] J. A. HOFFNAGLE and C. M. JEFFERSON, “Design and performance of a refractive optical system that converts a Gaussian to a flattop beam.” *Applied optics*, vol. 39, no. 30, pp. 5488–99, Oct. 2000.
- [39] Y. BAYKAL and H. T. EYYBOGLU, “Scintillation index of flat-topped Gaussian beams.” *Applied optics*, vol. 45, no. 16, pp. 3793–7, Jun. 2006.
- [40] V. BAGINI, R. BORGHI, F. GORI, a. M. PACIELO, M. SANTARSIERO, D. AMBROSINI, and G. S. SPAGNOLO, “Propagation of axially symmetric flattened Gaussian beams,” *Journal of the Optical Society of America A*, vol. 13, no. 7, p. 1385, Jul. 1996. [Online]. Available: <http://www.opticsinfobase.org/abstract.cfm?URI=josaa-13-7-1385>
- [41] D. C. COWAN, J. RECOLONS, L. C. ANDREWS, and C. Y. YOUNG, “Propagation of flattened Gaussian beams in the atmosphere: a comparison of theory with a computer simulation model,” in *Proc. of SPIE, Atmospheric Propagation III*, C. Y. Young and G. C. Gilbreath, Eds., vol. 6215, no. 1, May 2006, pp. 62 150B–62 150B–10.
- [42] F. M. DICKEY and S. C. HOLSWADE, *Laser Beam Shaping: Theory and Techniques*, ser. Optical Science and Engineering. Taylor & Francis, 2002.

- [43] P. BARCIK, L. HUDCOVA, O. WILFERT, J. L. ARCE-DIEGO, F. FANJUL-VELEZ, I. SALAS-GARCIA, and N. ORTEGA-QUIJANO, “Comparison and evaluation of the laser beam-shaping techniques,” in *Proc. of SPIE, Laser Communication and Propagation through Atmosphere and Oceans II*, A. M. J. van Eijk, C. C. Davis, and S. M. Hammel, Eds., vol. 8874, Sep. 2013, p. 88740E. [Online]. Available: <http://proceedings.spiedigitallibrary.org/proceeding.aspx?doi=10.1117/12.2023213>
- [44] P.-H. Y. CHEN, C.-H. CHEN, and CHENG-HUAN, “Low speckle laser illuminated projection system with a vibrating diffractive beam shaper,” *Opt. Express*, vol. 20, pp. 16 552—16 566, 2012.
- [45] J. J. KASINSKI and R. L. BURNHAM, “Near-diffraction-limited laser beam shaping with diamond-turned aspheric optics.” *Optics letters*, vol. 22, no. 14, pp. 1062–4, 1997.
- [46] J. HOFFNAGLE, “Refractive Optical System that Converts a Laser Beam to a Collimated Flat-Top Beam,” 2001.
- [47] S. DE SILVESTRI, P. LAPORTA, V. MAGNI, O. SVELTO, and B. MAJOCCHI, “Unstable laser resonators with super-Gaussian mirrors.” *Optics letters*, vol. 13, no. 3, pp. 201–3, Mar. 1988.
- [48] Z. FENG, L. HUANG, and G. JIN, “Beam shaping system design using double freeform optical surfaces,” *Optics express*, vol. 21, no. 12, pp. 14 728–14 735, 2013.
- [49] D. L. SHEALY and J. A. HOFFNAGLE, “Laser beam shaping profiles and propagation.” *Proceedings SPIE 5876, Laser Beam Shaping VI*, 2005.
- [50] F. DUERR and H. THIENPONT, “Refractive laser beam shaping by means of a functional differential equation based design approach,” *Optics express*, vol. 22, no. 7, pp. 10 839–10 846, 2014.
- [51] P. BARCIK, E. LEITGEB, and L. HUDCOVA, “Optical wireless communication transmitter with a refraction beam shaper,” *2014 9th International Symposium on Communication Systems, Networks & Digital Sign (CSNDSP)*, pp. 1044–1048, Jul. 2014. [Online]. Available: <http://ieeexplore.ieee.org/lpdocs/epic03/wrapper.htm?arnumber=6923983>
- [52] D. L. SHEALY and S.-H. CHAO, “Geometric optics-based design of laser beam shapers,” *Optical Engineering*, vol. 42, no. 11, p. 3123, Nov. 2003. [Online].

Available: <http://opticalengineering.spiedigitallibrary.org/article.aspx?doi=10.1117/1.1617311>

- [53] Y. GAO, Z. AN, J. WANG, W. ZHAO, and F. SONG, “Automatic optimization design of Gaussian beam shaping system by using ZEMAX software,” *Optik - International Journal for Light and Electron Optics*, vol. 122, no. 24, pp. 2176–2180, Dec. 2011.
- [54] J. L. KREUZER, “Coherent light optical system yielding an output beam of desired intensity distribution at a desired equiphase surface,” 1969.
- [55] J. C. RICKLIN and F. M. DAVIDSON, “Atmospheric turbulence effects on a partially coherent Gaussian beam: implications for free-space laser communication.” *Journal of the Optical Society of America. A, Optics, image science, and vision*, vol. 19, no. 9, pp. 1794–802, Sep. 2002. [Online]. Available: <http://www.ncbi.nlm.nih.gov/pubmed/12216873>
- [56] Y. BAYKAL, H. T. EYYBOGLU, and Y. CAI, “Scintillations of partially coherent multiple Gaussian beams in turbulence.” *Applied optics*, vol. 48, no. 10, pp. 1943–54, Apr. 2009. [Online]. Available: <http://www.ncbi.nlm.nih.gov/pubmed/19340150>
- [57] M. PAVLU and J. POLIAK, “Modeling of the multichannel optical wireless link,” in *Conference on Microwave Techniques (COMITE), 2013*, 2013, pp. 79–82.
- [58] J. POLIAK, “Diffraction Effects in Transmitted Optical Beam,” Doctoral thesis, Brno University of Technology, 2014.
- [59] J. GERRARD, A. and BURCH, *Introduction to Matrix Methods in Optics*, dover book ed. Dover, 1975.
- [60] H. HEMMATI, *Near-Earth Laser Communications*. CRC Press, 2009.
- [61] C. GOMEZ-REINO, M. V. PEREZ, C. BAO, and M. T. Flores-Arias, “Design of GRIN optical components for coupling and interconnects,” *Laser and Photonics Reviews*, vol. 2, no. 3, pp. 203–215, 2008.
- [62] M. BORN and E. WOLF, *Principles of Optics: Electromagnetic Theory of Propagation, Interference and Diffraction of Light*. CUP Archive, 2000.
- [63] I. L. GOLDBERG and A. MCCULLOCH, “Annular Aperture Diffracted Energy Distribution for an Extended Source,” Goddard Space Flight Center, Greenbelt, Maryland, Tech. Rep., 1968.

- [64] E. EVERHART and J. KANTORSKI, “Diffraction Patterns Produced by Obstructions in Reflecting Telescopes of Modest Size,” *The Astronomical Journal*, vol. 1, 1959.
- [65] V. SACEK, “Notes on Amateur Telescope Optics,” 2006. [Online]. Available: <http://www.telescope-optics.net>
- [66] K. KATAOKA, “Estimation of coupling efficiency of optical fiber by far-field method,” *Optical Review*, vol. 17, no. 5, pp. 476–480, 2010.

# LIST OF SYMBOLS, PHYSICAL CONSTANTS AND ABBREVIATIONS

EDFA Erbium Doped Fiber Amplifier

$\mathcal{F}$  Fourier transform

FG Flattened Gaussian Beam

FSO Free Space Optical

NA Numerical aperture

RF Radio Frequency

A Aperture averaging factor

$a$  Parameter

$A_A$  Attenuation caused by absorption

$a_s^2$  Flattened beam radius

$A_S$  Attenuation caused by scattering

$C_n^2$  Refractive index structure parameter

$C_T$  Temperature structure parameter

$D_{1,RXA}$  Diameter of receiving antenna (the primary mirror)

$D_{2,RXA}$  Diameter of receiving antenna (the secondary mirror)

$D_{Eq,RXA}$  Equivalent diameter of the receiving antenna

$D_n(\mathbf{r})$  Structure function of the refractive index

$D_{RXA}, D$  Diameter of the receiving aperture

$d_{spot, ideal}$  Spot size at the focal plane of the receiving lens

$d_{spot, turb}$  Spot size at the focal plane of the receiving lens in case of atmospheric turbulence

$F_0$  Radius of curvature in the plane of the transmitter

$H_m, H_n$  Hermite polynomial

$i$	Imaginary unit
$I$	Optical intensity
$I_0$	On axis intensity
$J_n$	Bessel function
$k$	Wave number of beam wave ( $k=2\pi/\lambda$ )
$L$	Space scale of the flow process
$l_0$	Small scale of the atmospheric turbulence
$L_0$	Large scale of the atmospheric turbulence
$L_p^l$	Laguerre polynomial
$M$	Margin of the link
$M_{\text{step}}$	Number of steps of the optical wave propagation
$N$	Flatness order of the Flattened Gaussian beam
$n$	Index of refraction
$N_{\text{Fresnel}}$	Number of Fresnel zone
$o$	central obstruction diameter
$p$	Flatness order of the Flattened Gaussian beam
$P_{0,\text{RXA}}$	Receiver sensitivity (mean)
$P_{\text{m,TXA}}$	Transmitted optical power (mean)
$P_{\text{atm}}$	Atmospheric pressure
$P_{\text{RXA}}$	Received power
$q$	Flatness order of the Flattened Gaussian beam
$r$	Size of the turbulent eddie
$\mathbf{r}$	Transverse position of observation point
$R_0$	Radius at which the intensity fall to half of its value on the axis
$r_0$	Fried coherence diameter

$r_A$	Radius of the Airy disk
$r_{cd}$	Radius of the central diffraction disk
$r_c^2$	Root-mean square centroid displacement
$R_e$	Reynolds number
$R_{FL}$	Width of the flattened beam
$T$	Temperature
$u$	Velocity of the flow
$U$	Complex amplitude of the field in the plane of the transmitter
$v_m$	Kinematic viscosity
$w_0$	Waist of the Gaussian beam
$W_e$	Effective beam width in the plane of the receiver
$\alpha(\lambda)$	Extinction coefficient
$\alpha_{atm}$	Atmospheric loss
$\alpha_{prop}$	Propagation loss
$\alpha_{rec, syst}$	Receiver system loss
$\alpha_{trans, syst}$	Transmitter system loss
$\beta_a$	Variance of the angle of arrival
$\beta_x, \beta_x$	Parameter of the Cos Gaussian beam
$\Gamma(\mathbf{r}_1, \mathbf{r}_2, \tau)$	Mutual coherence function
$\gamma(\mathbf{r}_1, \mathbf{r}_2, L)$	Complex degree of coherence
$\gamma_{total}$	Total gain of the receiver
$\Delta z$	Single step of the optical wave propagation
$\epsilon$	Ratio between the radius of the central obstruction and aperture of the telescope
$\theta$	Beam divergence (half-angle)



$\Theta$	Refractive beam parameter
$\Theta_0$	Refraction parameter in the plane of the transmitter
$\kappa$	Spatial wave number
$\kappa_m$	Small scale wave number parameter
$\kappa_0$	Large scale wave number parameter
$\lambda$	Wavelength
$\Lambda_e$	Effective diffraction parameter in the plane of the receiver
$\Lambda_0$	Diffraction parameter in the plane of the transmitter
$\rho_G$	Spatial coherence radius of the Gaussian beam wave
$\rho_{pl}$	Spatial coherence radius of the plane wave
$\rho_{sp}$	Spatial coherence radius of the spherical wave
$\sigma_1^2$	Rytov variance
$\sigma_B^2$	Rytov variance for beam wave
$\sigma_I^2$	Scintillation index - normalized variance of optical intensity
$\omega_A$	Angular radius of the Airy disk
$\phi_n(\kappa)$	Spatial power spectrum of refractive index
$\omega_A$	Angular radius of Airy beam
$\omega_{CD}$	Angular radius of central diffraction disk
$\omega_0, \beta_x$	Parameter of the Cosh Gaussian beam

# LIST OF APPENDICES

A Curriculum Vitae	91
B List of Publications	94

# A CURRICULUM VITAE

## Peter Barcik

---

Technicka 3082/12  
616 00 Brno  
Czech Republic  
Phone: +420 541 14 6558  
E-mail: xbarci00@stud.feec.vutbr.cz

### RESEARCH INTERESTS

Free space optical communication with special emphasis on atmospheric effects, modeling of laser beam propagation in turbulent media.

### EDUCATION

since 2012 Brno University of Technology, Brno, Czech Republic

- Doctor of Philosophy (Ph.D.), Electronics and Communication
- Thesis: Analysis and optimalization of optical intensity distribution in a laser beam for optical wireless communication

2010 - 2012 Brno University of Technology, Brno, Czech Republic

- Master's degree (Ing.), Electronics and Communication
- Thesis: The distribution of relative variance of optical intensity in laser beam
- Deans award in 2012

2007 - 2010 Brno University of Technology, Brno, Czech Republic

- Bachelor's degree (Bc.), Electronics and Communication
- Thesis: Laboratory module of class D amplifier with PWM modulation

### ACADEMIC APPOINTMENTS

- since 9/2012 Department of Radio Electronics, Brno University of Technology
- since 10/2012 Sensor, Information and Communications Systems (SIX) research group
- 10/2012 - 5/2014 Research assistant at Central European Institute of Technology (CEITEC)

### RESEARCH STAY

- 1/2014 - 2/2014 Short Time Scientific Mission within COST IC1101 project  
Graz University of Technology, Austria  
Project: Modeling and Simulation of the Laser Beam Shaping Systems for FSO Terminal  
Supervised by: Prof. Erich Leitgeb

### COMPUTER SKILLS

- Matlab - Intermediate
- OrCad PSpice, AutoCad, Eagle - Pre-Intermediate
- MS office, LaTeX - Advanced
- Adobe Creative Suite - Advanced
- Cinema 4D - Beginner

**EXPERIENCE**

- 07/2007 - 08/2007 LEONI Autokabel Slovakia, s.r.o., Ilava, Slovak Republic
- 07/2008 - 08/2008 Delta Electronics Slovakia, s.r.o., Dubnica nad Vahom, Slovak Republic

**LANGUAGE  
SKILLS**

- Slovak - Native speaker
- English - Intermediate
- Spanish - Basic knowledge
- German - Basic knowledge

## B LIST OF PUBLICATIONS

## LIST OF PUBLICATIONS

---

### 2016

WILFERT, O.; BARCÍK, P.; KOLKA, Z. : Fully Photonic Wireless Link for Transmission of Synchronization Signals. *Radioengineering*, 2016, roč. 25, č. 1, s. 18-25. ISSN: 1210-2512.

POLIAK, J., BARCÍK, P., WILFERT, O.: Diffraction Effects and Optical Beam Shaping in FSO Terminals. In *Optical Wireless Communications - An Emerging Technology*. 1. Edition. Springer International Publishing, 2016. Chapter 7. ISBN: 978-3-319-30200-3.

### 2015

BARCÍK, P.; WILFERT, O.; LEITGEB, E.; HUDCOVA, L.: Optimal Distribution of the Optical Intensity within a Laser Beam for Optical Wireless Communications. *IET Optoelectronics*, 2015, DOI: 10.1049/iet-opt.2014.0153, Online ISSN 1751-8776.

BARCÍK, P.; WILFERT, O.; KOLKA, Z. Coupling Efficiency Estimation of the Fully Photonic Receiver. In *Proceedings of the 2015 13th International Conference on Telecommunications ConTEL 2015*. Graz: Graz University of Technology, 2015. s. 1-5. ISBN: 978-1-4799-8971- 3.

WILFERT, O.; KOLKA, Z.; BARCÍK, P.; DOBESCH, A.; PAVLŮ, M. The use of photonic technology in optical wireless links. In *14th Conference on Microwave Techniques, COMITE 2015*. 2015. s. 135-138. ISBN: 978-1-4799-8121- 2.

### 2014

POLIAK, J.; PEZZEI, P.; BARCÍK, P.; LEITGEB, E.; HUDCOVÁ, L.; WILFERT, O. On the derivation of exact analytical FSO link attenuation model. *Transactions on Emerging Telecommunications Technologies*, 2014, roč. 25, č. 6, s. 609-617. ISSN: 2161- 3915.

BARCÍK, P.; HUDCOVÁ, L.; LEITGEB, E. Optical Wireless Communication Transmitter with a Refraction Beam Shaper. In *Proceedings of the 9th International Symposium on Communication Systems, Networks & Digital Sign*. Manchester: 2014. s. 1044-1048. ISBN: 978-1-4799-2581- 0.

BARCÍK, P.; WILFERT, O.; LEITGEB, E. Design of Refraction Beam Shaper for FSO Transmitter. In *Proceedings of the 16th International Conference on Transparent Optical Networks ICTON 2014*. Warsaw, Poland: National Institute of Telecommunications, 2014. s. 1-4. ISBN: 978-1-4799-5600- 5.

BARCÍK, P.; HUDCOVÁ, L. Measurement of Spatial Coherence of Light Propagating in a Turbulent Atmosphere. *Radioengineering*, 2013, roč. 22, č. 1, s. 341-345. ISSN: 1210- 2512.

### 2013

HUDCOVÁ, L.; BARCÍK, P. Comparison of Gaussian Beams with Different Halfwidths using the Method of Available Power in Turbulent Atmosphere. In *Proceedings of 13th Conference on Microwave Techniques COMITE 2013*. 2013. s. 88-91. ISBN: 978-1-4673-5513- 1.

BARCÍK, P.; WILFERT, O. Simulation of Atmospheric Turbulence Effect on Horizontal Free Space Optical Link. In *Proceedings of the 25th Conference and Exhibition on Optical Communications 2013*. Praha: Action M Agency, 2013. s. 47-50. ISBN: 978-80-86742-37- 3.

BARCÍK, P.; HUDCOVÁ, L.; WILFERT, O.; ARCE-DIEGO, J.; FANJUL-VÉLEZ, F.; SALAS-GARCÍA, I.; ORTEGA-QUIJANO, N. Comparison and evaluation of the laser beam- shaping techniques. In SPIE Proceedings Vol. 8874 Laser Communication and Propagation through the Atmosphere and Oceans II. San Diego: SPIE, 2013. s. 1-7. ISBN: 9780819497246.

BARCÍK, P.; HUDCOVÁ, L. Measurement of Spatial Coherence of Light Propagating in a Turbulent Atmosphere. Radioengineering, 2013, roč. 22, č. 1, s. 341-345. ISSN: 1210- 2512.

BARCÍK, P.; HUDCOVÁ, L.; WILFERT, O. Influence of the Atmospheric Turbulence on the Laser Beam. In Proceedings of the 2013 18th European Conference on Network and Optical Communications & 2013 8th Conference on Optical Cabling and Infrastructure (NOC-OC&I). Graz: TU Graz, 2013. s. 83-86. ISBN: 978-1-4673-5822- 4.

WILFERT, O.; POLIAK, J.; BARCÍK, P.; ARCE-DIEGO, J.; FANJUL-VÉLEZ, F.; SALAS-GARCÍA, I.; ORTEGA-QUIJANO, N. Detection of non- standard atmospheric effects in FSO systems. In SPIE Optics & Photonics 2013 Conference on Laser Communication and Propagation through the Atmosphere and Oceans II. San Diego: SPIE Press, 2013. s. 1-8. ISBN: 978-0-8194-9724- 6.

## **2012**

BARCÍK, P.; WILFERT, O. The Distribution of Relative Optical Intensity Variance in a Laser Beam. In Proceedings of the 24th Conference and Exhibition on Optical Communications 2012. Praha: Agentura Action M, 2012. s. 43-46. ISBN: 978-80-86742-36- 6.

HUDCOVÁ, L.; BARCÍK, P. Experimental Measurement of Beam Wander in the Turbulent Atmospheric Transmission Media. In Proceedings of 22nd International Conference Radioelektronika 2012. 2012. s. 191-194. ISBN: